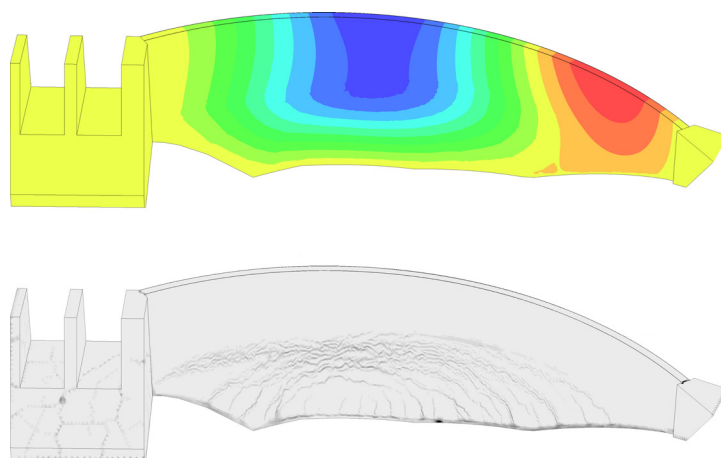# FINITE ELEMENT ANALYSIS OF CRACKING OF CONCRETE ARCH DAMS DUE TO SEASONAL TEMPERATURE VARIATION

FREDRIK HJALMARSSON and
FREDRIK PETTERSSON

Structural
Mechanics

Master's Dissertation

FINITE ELEMENT ANALYSIS OF CRACKING OF CONCRETE ARCH DAMS DUE TO SEASONAL TEMPERATURE VARIATION

FREDRIK HJALMARSSON and FREDRIK PETTERSSON

Preface

This master dissertation was carried out at the Division of Structural Mechanics, Faculty of Engineering LTH at Lund University, and concludes five years of civil engineering studies. This work was carried out in collaboration with ÅF Hydro Power South, International division, in Malmö during the spring of 2017.

We would like to express our sincerest gratitude to our supervisors, Senior Lecturer Susanne Heyden at the Division of Structural Mechanics, Faculty of Engineering LTH at Lund University and PhD Tomas Ekström at ÅF International Division for their guidance and support throughout this project. We would also like to thank Chaoran Fu and the rest of the colleagues at ÅF Hydro Power South for their valuable advice and for and making our time there much enjoyable.

Fredrik Hjalmarsson and Fredrik Pettersson

Lund, June 2017

Abstract

Dams located in the Nordic countries are subjected to large temperature variations between summer and winter. In the northern part of Sweden dams are subjected to temperature variations of up to 60-70 °C. This often results in cracking of the concrete and causes challenges in the design of new dams as well as maintenance of existing dams.

Seasonal temperature variation has been found to be the dominant cause of cracking in large, massive concrete structures. The difference in temperature of the water on the upstream side, and the ambient air on the downstream side, causes a temperature gradient in the dam which results in non-uniform expansion and contraction of the concrete.

This master dissertation is a part of an initiative from the ICOLD-committee "Computational Aspects of Dam Analysis and Design" with the aim to find a suitable FE-methodology to better analyse these kinds of phenomena.

An arch dam located in northern Sweden is analysed in order to see how temperature variations would influence the displacement and cracking of the dam. The work consisted of three parts which analyses the temperature distribution, the displacement and the crack propagation of the dam. The finite element application Abaqus 2016 was used for all of the analyses.

The analyses concludes that the seasonal temperature variations have a significant influence on the structural behaviour of arch dams in colder climates. As the water temperature do not go below 0 °C, cold winters can have a major effect on arch dams in regards to deformation and cracking.

Keywords: arch dam, hydro power, finite element method, abaqus, temperature variations, concrete, deformation, crack propagation

Sammanfattning

Flera dammkonstruktioner i Norden utsätts för stora temperaturvariationer mellan sommar och vinter. I norra Sverige kan dammar vara utsatta för temperaturvariationer på upp emot 60-70 °C. Detta resulterar ofta i sprickbildning i betongen vilket medför utmaningar vid både utformning av nya dammar och underhåll av befintliga.

Säsongsmässiga temperaturvariationer är den dominerande orsaken till sprickbildning i stora, massiva betongkonstruktioner. Skillnaden i temperatur mellan uppström- och nedströmssidan orsakar en temperaturgradient i dammkroppen vilket leder till en ojämn expansion eller krympning i betongen.

Detta examensarbete är en del av ett initiativ från ICOLD-kommittén "Computational Aspects of Dam Analysis and Design" med mål att hitta en lämplig FE-metodologi för att bättre kunna analysera dessa typer av fenomen.

En valvdamm i norra Sverige analyserades för att undersöka hur temperaturvariationer orsakar deformationer och påverkar spricktillväxt i dammkroppen. Arbetet består av tre delar som analyserar temperaturfördelningen, deformationen och spricktillväxten i dammen. Finita elementprogrammet Abaqus 2016 användes i alla analyser.

Analyserna fastställer att säsongsmässiga temperaturvariationer har en betydande påverkan på det mekaniska beteendet i valvdammar i kalla klimat. Kalla vintrar har en stor inverkan på valdammar avseende deformation och spricktillväxt då medeltemperaturen i dammen understiger 0 °C.

Nyckelord: valvdamm, vattenkraft, finita elementmetoden, abaqus, temperaturvariationer, betong, deformation, sprickbildning

Contents

Chapter 1

Introduction

1.1 Background

Hydropower facilities in Sweden produce around 65 TWh of electricity per year [17], which corresponds to approximately 45 % of the total electricity production in the country [16]. There are around 2000 dams in Sweden whereas about 200 of these are considered "big", with an effect of 10 MW or more. Around 80 % of the dams are located in the northern parts of the country [17]. Dams located in these cold areas are often subjected to harsh environmental conditions and large temperature variations. Many dams experience variations in temperature between summer and winter of up to 60‑70 °C [15]. As a result of this many of the concrete dams have been subjected to cracking [21].

The cracking is caused by the thermal expansion and contraction of concrete when heated or cooled. The difference in temperature of the water on the upstream side, and the ambient air on the downstream side, causes a temperature gradient in the dam which results in non-uniform expansion and contraction of the concrete. This will in turn create stresses in the dam and if the tensile stresses exceed the tensile strength of the concrete, cracks will propagate. Seasonal temperature variation has been found to be the dominant cause of cracking in large, massive concrete structures. Cracking of the concrete leads to penetration of water and exposes the body to freeze thaw action which creates bigger cracks and decreases the stability of the structure.

The design and maintenance of existing dams represent a challenge for the whole engineering community. Broad international collaboration has over the last decades been performed through organisations such as ICOLD (International Commission On Large Dams) for the improvement of hydro-power facilities. The research has covered both the characterisation and documentation of different types of cracks, as well as research with the objective to better explain the causes of cracks in these large concrete structures.

This report is a part of an initiative from the ICOLD-committee "Computational Aspects of Dam Analysis and Design" with the aim to find a suitable finite element (FE) methodology to better analyse these kinds of phenomena. The result will be presented on the "14th International Benchmark Workshop on Numerical Analysis of Dams" in Stockholm, September 2017.

Numerical 3D FE-analyses is a powerful tool for design and assessment of large, concrete dams and allows for more detailed analyses compared to traditional methods. The use of numerical analyses based on the FE-method in the field of structural engineering has increased significantly over the last decade and is today the dominant discretisation technique [28]. Regarding the maintenance of concrete dams, advanced non-linear FE-analyses can support monitoring systems on site regarding

the assessment of dam safety issues. FE-analyses can also be used to predict the effects of repair work on dams that are in bad condition.

There is a need of greater understanding of how to evaluate the non-linear finite element method for analysis of concrete dams and to show possibilities and restrictions associated with this method. In the design process of large concrete dams today, non-linear analyses is mainly used in the later stages in order to verify the structural behaviour of the final design [20].

1.2   Aim and objective

The aim of this report is divided into two parts, (i) find a suitable FE methodology to describe the crack propagation and response of large concrete dams subjected to temperature variations, (ii) analyse the risk for, and the extent of, cracking on a specific concrete arch dam in northern Sweden as a result of seasonal temperature variations.

The objective is divided into four parts. The first part is a transient thermal analysis where the temperature distribution in the dam is calculated. The second part is a linear mechanical analysis with gravity loads, hydrostatic water pressure and temperature loads due to seasonal temperature variations. In the linear mechanical analysis, the displacements in the dam are calculated and areas with high stresses that may be subjected to cracking are identified. The third part consists of mechanical analyses of the dam with a non-linear material model in which the displacements of the dam and the extent of cracking, *i.e* crack patterns, in the dam are calculated.

The result from the linear and non-linear analyses are compared in order to visualise the different analyses influence on the displacement. In the last part of the report assumptions in the previous parts are changed to see how these will influence the results with regards to crack propagation and displacement of the dam. The model is based on a real arch dam in northern Sweden but the results should be applicable as guidance for other concrete arch dams with similar characteristics as well.

1.3   Scope and limitations

The focus of this report is how seasonal temperature variations influence the crack propagation and displacement of concrete arch dams. The following three loads were taken into consideration in the analyses,

- Gravity loads
- Water pressure (only hydrostatic pressure)
- Temperature variations (only convective heat transfer)

The dam body was considered monolithic, *i.e.* without consideration of discontinuities from casting segments. Moreover, other types of loads and effects was neglected, such as,

- Loads from ice pressure, uplift pressure etc.
- Pore pressure distributions within the dam and foundation
- Thermal effects due to solar radiation
- Influence from construction sequence
- Influence from joints (such as lift and construction joints in the dam body)
- Influence from fractures in the rock foundation

1.4   Outline

The report contains 8 chapters, of which the content is the following;

Chapter 1 describes the background, aim and objectives of the report as well as limitations.

Chapter 2 provides a description of arch dam design and terminology. Loads present in the analyses are also described.

Chapter 3 gives a brief overview of the finite element method.

Chapter 4 describes the material behaviour of concrete and how this was modelled in Abaqus.

Chapter 5 describes the input data for the reference dam used in the numerical simulations.

Chapter 6 describes the modelling and methodology used in the numerical simulations.

Chapter 7 provides the results of the analyses.

Chapter 8 contains a discussion of the results and suggests ideas for further research.

In the appendix results which are not presented in the previous chapters are presented.

Chapter 2

Arch dams

2.1 Design principles and terminology

Arch dams are unique in the way they carry the main part of the hydrostatic load by arch action. Other types of dams, such as buttress and gravity dams, mainly rely on their self-weight to resist the imposed loads. The different way of carrying the load allows arch dams to have a more slender design [29].

The design of arch dams is highly dependent on the layout of their location. The crest height, thickness and radius of the arch are all aspects which are highly dependent on the conditions on site. Dams located in colder areas, such as the Nordic countries, may have insulated walls on the downstream side designed to reduce the thermal gradient in the dam body [20]. The reference arch dam used in the analyses is illustrated in Figure 2.1. Some conceptual terms regarding arch dams are illustrated in Figure 2.2.

(a) Spillway   (b) Dam body   (c) Support
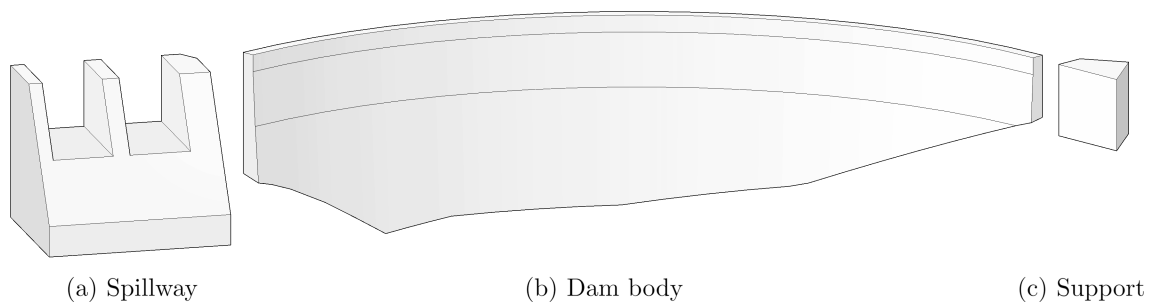
Figure 2.1: Geometry of the reference dam with the parts separated for clarification.
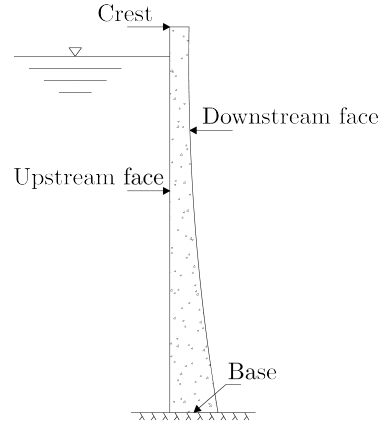
Figure 2.2: Conceptual terms used for arch dams.

The section shape can be designed with a *single* or *double* curvature. Single curvature arch dams are only curved in one plane, without any vertical curvature. Double curvature refers to the dam being curved in both plane and elevation, which has been the dominant design technique since 1950. Double curvature allows for a thinner and more efficient dam as the design utilises the self-weight to greater advantage and better accommodate the increase of hydrostatic forces [34]. The single and double curvature designs are illustrated in Figure 2.3b and Figure 2.3c respectively.

(a) Plane

(b) Section A-A, single curvature

(c) Section A-A, double curvature
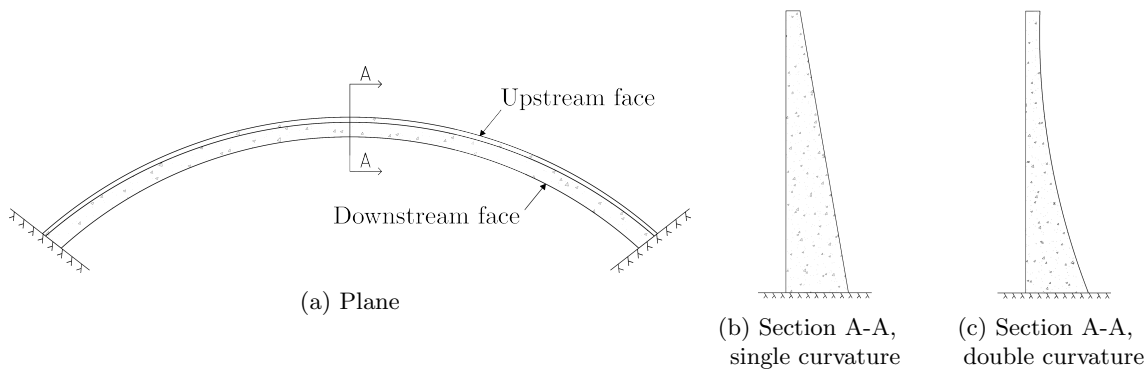
Figure 2.3: In plane, single and double curvature arch dam design.

Due to the small contact area of the arch dam with the foundation, the material properties of the rock are important factors to assure structural integrity. Arch dams require a foundation of sufficient compressive strength in order to resist the bearing pressure from the dam. This applies for the abutments as well as the forces are transmitted via arch action to the supports and into the canyon walls.

When designing the abutments it is important to make the connections as smooth as possible in order to achieve an even distribution of the forces between the dam and the rock. The angle between arch and abutment is of great importance. A general rule is that the angle should be less than 30° in order to reduce high concentrations of shear forces [34].

Spillways serve a variety of functions, for example detention of water or preventing overflows during a sudden rise of the water level in the reservoir. Spillways can be considered *attached* or *detached*. Attached spillways go through the dam body whereas a detached spillway can be designed as a side channel, tunnel, chute etc. located beside the dam. In the reference dam the spillway is attached

and located on the left side support at the crest and constitute the right abutment to the arch dam.

2.2   Loads

Dams are subjected to a variety of loads, both static and dynamic. Examples of loads that should be considered when evaluating the design of dams are,

- Gravity loads
- Water pressure (hydrostatic pressure and pore pressure)
- Temperature variation
- Ice loads
- Earth pressure
- Uplift pressure
- Traffic loads etc.

Temperature loads have significant influence on the design of arch dams compared to gravity dams due to the thinner cross section [34]. This section will not go into detail on all of the loads mentioned but rather give a brief description of the loads considered in the analyses of this report.

2.2.1   Gravity loads

Gravity loads, F_g, are considered as body forces in the numerical model and are calculated based on the volume and density of the modelled structure as

$$F_g = \rho g V \tag{2.1}$$

where,

ρ $\qquad$ is the density of the body.

g $\qquad$ is the acceleration of gravity, 9.81 m/s^2.

V $\qquad$ is the volume of the body.

2.2.2   Hydrostatic pressure

The hydrostatic pressure, p_w, is the dominant external force acting on the dam. The hydrostatic water pressure is considered as a surface force and is calculated by

$$p_w(h) = \rho_w g h \tag{2.2}$$

where,

ρ_w $\qquad$ is the density of water, assumed to be 1000 kg/m^3 at all temperatures.

h $\qquad$ is the depth below the water surface.

2.2.3   Temperature variation

Thermal stresses arise because of a restriction in motion when the material expands or contracts due to a temperature variation. The stresses, $\Delta\sigma$, that develop are calculated by

$$\Delta\sigma = \varepsilon_{th}E = \alpha(T - T_0)E \tag{2.3}$$

where,

E	is the elastic modulus.
ε_{th}	is the strain due to temperature variation.
α	is the thermal expansion coefficient.
T	is the current temperature.
T_0	is the initial temperature.

Chapter 3

The finite element method

By using partial differential equations various physical phenomena in a region, in one or multiple dimensions, can be described. These differential equations are often too complicated to solve using classic analytical methods. The finite element method is a numerical method for solving partial differential equations by using approximations and is widely used in engineering mechanics today.

3.1 Theory

Using the finite element method, a region is subdivided into disjoint components, so-called finite elements, and assigned material properties. In FE applications there are several different element classes available, suitable for different applications. Figure 3.1 illustrates a selection of commonly used element classes in structural analyses. For dams with variation in cross-section and/or dams that transfer loads in lateral direction, 3D solid (continuum) elements are mainly used [20].
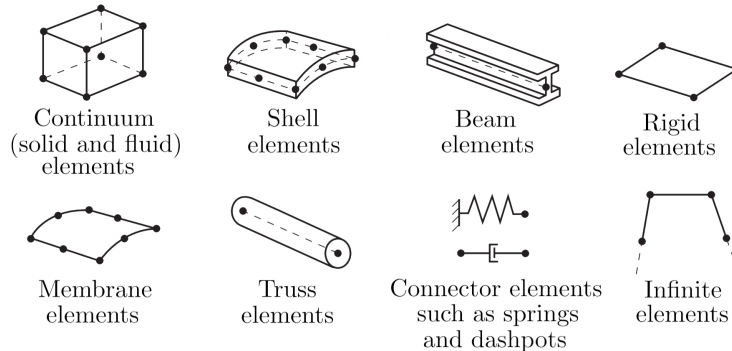
Figure 3.1: Common element classes used in structural analyses. Reproduction from Abaqus 6.14 Analysis User's Guide [8].

Nodal points are located at the corners or end points of the elements, illustrated as dots in Figure 3.1. Depending on the type of analysis the nodal points can have one or several different properties assigned, such as temperature and translation. The properties are specified by the degrees of freedom (DOF) for each node. In stress analyses the DOF of a node represent translation or rotation in the node. In this type of analysis the number of DOFs in a node define the number of ways the node is allowed to move. Some degrees of freedom in the system needs to be known in

order to obtain a unique solution. Shape functions are used to calculate the field variables between the nodes.

In first order elements, with nodes only at corners or end points, the field variables are calculated by linear shape functions between the nodes. In higher-order elements nodes are also placed between corners or endpoints which allow quadratic interpolation. Linear interpolation results in a linear estimation of the initial and deformed structural geometry. This may give a poor result in describing bending as the edges of the elements are unable to curve, which is known as *shear locking* [8]. Elements of higher order, with quadratic interpolation, solves this problem as the elements may be bent and thus give more reliable results. One has to take into consideration the increase of computational time with the use of higher order elements with their greater number of DOFs per element. However higher order elements allow a more coarse mesh, and thus fewer elements and can sometimes compensate for the increased CPU-time per element [20].

In a static analysis of a linear system the equilibrium equation for each DOF are solved by Equation (3.1).

$$\mathbf{K} \, \mathbf{a} = \mathbf{f} \tag{3.1}$$

where,

$\mathbf{K}$ is the stiffness matrix, describing the constitutive behaviour of the structure.

$\mathbf{a}$ is the nodal displacement vector containing the degrees of freedom.

$\mathbf{f}$ is the force vector containing both body and surface forces.

The finite elements define a finite element mesh. In general the use of a greater number of elements or elements of higher order will increase the accuracy of the result. However, the result is also dependent on how the mesh is defined. Using elements with a poor aspect ratio, *i.e.* elements with a ratio that differs from height/width ≈ 1, can result in a less accurate result [20]. Figure 3.2 illustrates elements with good and bad aspect ratios.

(a) Good   (b) Bad
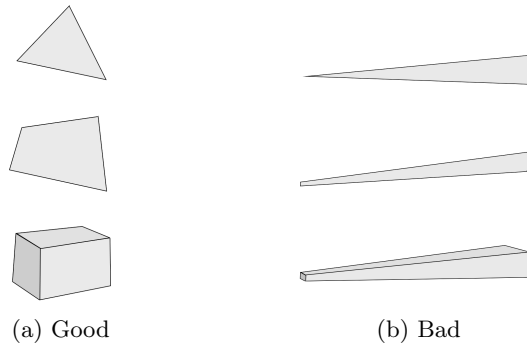
Figure 3.2: Examples of good and bad aspect ratios of an element.

When decreasing the element size, the approximate solution converges towards the exact, analytic solution. A finer mesh will however also increase CPU-time. As computational power and software continues to improve, bigger and more complex structures can be analysed. Finding a suitable mesh is an important step of numerical analyses, especially for analyses of materials with non-linear behaviour. A convergence study should always be performed to check if the mesh is fine enough. When the result is no longer significantly affected by further decreasing the element size, the calculated solution has converged to the exact solution. The requirement on a fine mesh is not as strict in linear-elastic analyses as in the case of non-linear analyses [20].

Non-linear finite element methods may suffer from convergence and stability problems. The use of non-linear FE-techniques requires a lot from the user, as the reliability of the results are dependent

on the accuracy of the model. The more complex the model is, the more difficult the interpretation of the results become [32].

Boundary conditions describe the behaviour at the boundaries of the simulation domain and are necessary for the system of equations to have a unique solution. Boundary conditions can be either *essential* or *natural*. Essential boundary conditions affect the DOFs and are imposed on the node displacement vector, **a**, whereas the natural boundary conditions are imposed on the force vector, **f**.

For further information about the finite element method the reader is referred to standard textbooks in the field, such as [26].

Chapter 4

Numerical modelling of concrete

Concrete is a composite material consisting of aggregate "glued" together with cement paste, water and often one or more types of admixture. The cement paste contributes to properties such as the compactness, stiffness and strength on a macro scale whereas the aggregate affects the casting process. The mechanical and physical properties of concrete are governed by the properties of the aggregate and cement paste and the transition zone between these components [2].

Concrete is generally considered to be a homogeneous and isotropic material. It is a brittle material with little to no plasticity before fracture in tension [2]. Therefore concrete structures are most often reinforced with steel rebars to transfer tensile forces.

The compressive strength of concrete is much higher compared to its tensile counterpart. Due to the different properties for compressive and tensile stresses it is important to get an understanding of the behaviour of concrete under different types of stresses. In this chapter linear and non-linear material properties of concrete are described briefly. For more detailed information on the subject the reader is referred to literature such as [30].

4.1 Linear elastic constitutive model

Linear-elastic behaviour is described using the elastic modulus and Poisson's ratio of the material. The elastic modulus, E, differs depending on the concrete quality and corresponds to the mean value 28 days after casting and varies between 27 and 44 GPa [33]. The elastic modulus is not constant over time as it decreases due to creep. Poisson's ratio, ν, is specified by Eurocode 2 [33] as

$\nu = 0.2$ for uncracked concrete

$\nu = 0$ for cracked concrete

In uni-axial loading, the stress increases linearly with the strain and the strain in calculated by dividing the change in length, ΔL with the initial length L. If brittle fracture is assumed, the material fractures when the stress reaches the ultimate limit stress [2].

Relying on linear-elastic analyses becomes increasingly unreliable as the stress increases and plasticity and cracking occurs in the material. Non-linear material behaviour must be taken into consideration for more extensive yielding [1].

4.2 Non-linear behaviour and constitutive models

The non-linear material properties of concrete due to cracking and crushing have a significant influence on the behaviour of a structure [20]. In this section the uni-axial and multi-axial non-linear behaviours of concrete in tension and compression are described.

4.2.1 Uni-axial stress

Tension

The behaviour of concrete under uni-axial tension is illustrated in Figure 4.1. The stress-strain curve is assumed to be linear elastic up until approximately 70 % of the peak tensile strength, f_t. Until this point, micro-cracks between the aggregate and cement paste are few and spread out across the whole volume of the specimen. At peak tensile stress, micro-cracks grow in both size and quantity, concentrating in front of the crack tip in the so-called *fracture process zone*. All further development of micro-cracks occurs in the fracture process zone until they unite and eventually result in the propagation of a crack. As the deformation increases the tensile stiffness decreases and the material starts softening. When the deformation reaches the point denoted ε_c, the concrete cracks and stress can no longer be transferred [2].
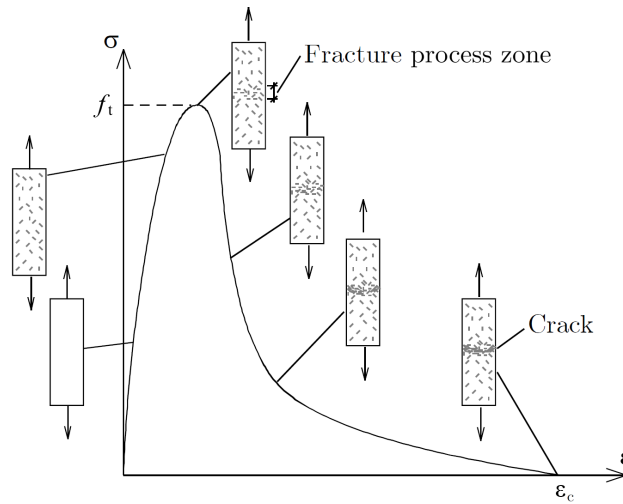

Figure 4.1: The response curve of concrete under uni-axial tension with illustrations describing the formation of micro-cracks and progression of a macro-crack [2].

Tension softening

Experimental observations has shown that concrete is not a perfectly brittle material as it retains some residual load-carrying capacity after reaching its tensile strength. This has led to the introduction of *tension softening* which aims to capture the gradually diminishing tensile stiffness of concrete upon further crack opening [9].

The behaviour of the fracture process zone can be described using a *stress-deformation curve*. The stress-deformation curve is obtained by subtracting the part of the stress-strain curve for uni-axial tensile loading which corresponds to the unloading curve of the concrete when unloaded at peak tensile stress as illustrated in Figure 4.2.

(a) Stress-strain curve with the un-
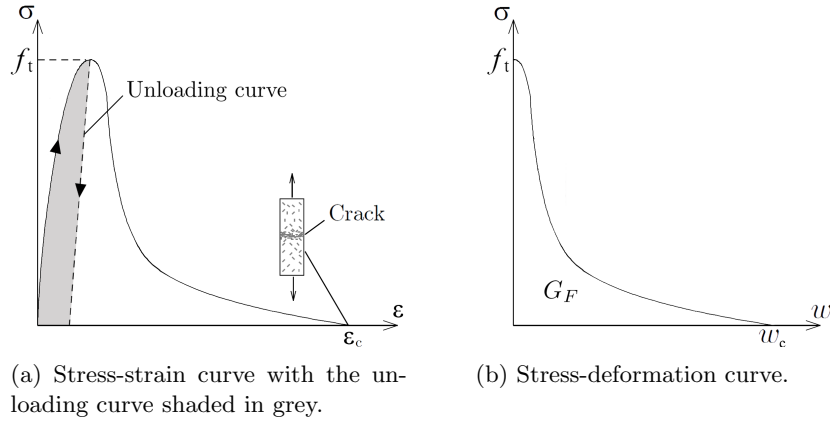loading curve shaded in grey.

(b) Stress-deformation curve.

Figure 4.2: Illustration of the transition from stress-strain curve to stress-deformation curve for
uni-axial tension by subtracting the unloading curve.

The area under the stress-deformation curve is defined as the fracture energy, G_F [N/m], consumed
per unit area as a crack develops. By introducing a crack opening law, also referred to as *tension
softening*, which is defined by the fracture energy, it is possible to define the formation of micro-
cracks into a macro-crack in FE-analyses [21].

The simplest way of describing the tension softening is by a linear approximation [30]. A second
more detailed bi-linear approximation was derived by Hillerborg [11]. A third, even more detailed
approximation of tension softening was made by Cornelissen et al. [5] as an exponential model
expressed as

$$\frac{\sigma}{f_t} = f(w) - \frac{w}{w_c} f(w_c) \tag{4.1}$$

in which

$$f(w) = \left[1 + \left(C_1 \frac{w}{w_c}\right)^3\right] \exp\left(-C_2 \frac{w}{w_c}\right) \tag{4.2}$$

where,

w	is the crack opening.
w_c	is the crack opening at which stress can no longer be transferred.
C_1	is a material constant. $C_1 = 3.0$ for normal density concrete.
C_2	is a material constant. $C_2 = 6.93$ for normal density concrete.

Linear, bi-linear and exponential approximations of tension softening are illustrated in Figure
4.3, with expressions of w_c for each approximation. The different ways of approximating tension
softening will result in different values of w_c.

(a) Linear   (b) Bi-linear   (c) Exponential
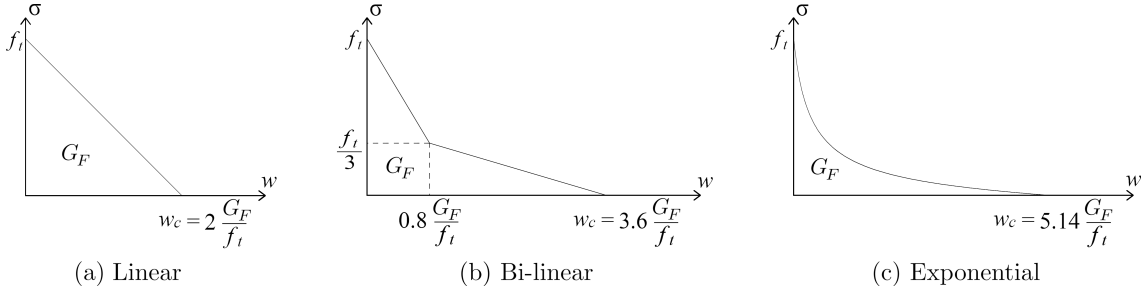
Figure 4.3: Approximation of tension softening with a linear, bi-linear and exponential function.

The fracture energy is best determined by experiments. In lack of experimental data, Model Code 2010 [23] provide a way to approximate the fracture energy by

$$G_F = 73 \cdot f_{cm}{}^{0.18} \tag{4.3}$$

where,

f_{cm} is the mean cylinder compressive strength of concrete [MPa].

Compression

Concrete behaves highly non-linear in uni-axial compression as shown by experimental tests. A typical behaviour for concrete under uni-axial compression is illustrated in Figure 4.4. Concrete is considered to act linear elastic up to approximately 30 % of the ultimate compressive stress in accordance with the initial (undamaged) elastic modulus, E_0, as illustrated between point (a) and (b). From point (b) to approximately 75 % of the ultimate compressive stress, at point (c), the stiffness of the concrete will start to decrease and the stress-strain curve becomes non-linear. After point (c) further loading will result in visible cracks of the concrete. After reaching peak compressive stress, f_c, and failure strain, ε_f, the concrete softens and the stress-strain curve descends [19].
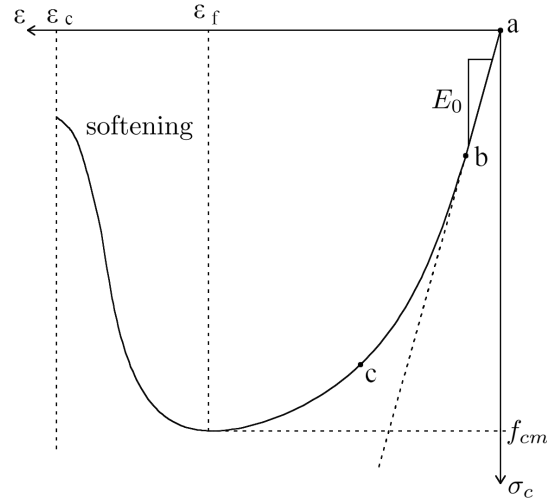

Figure 4.4: The response of concrete under uni-axial compression.

Equation (4.4), provided by Eurocode 2 [33] describes a compressive response curve of concrete subjected to uni-axial compression as shown in Figure 4.4. This can be used when actual measurements are not available.

$$\frac{\sigma_c}{f_{cm}} = \frac{k \cdot \eta - \eta^2}{1 + (k - 2)\eta} \tag{4.4}$$

where,

σ_c is the compressive stress.

f_{cm} is the mean compressive strength.

k is $1.05 \ E_{cm} \dfrac{|\varepsilon_{c1}|}{f_{cm}}$.

η is $\varepsilon_c / \varepsilon_{c1}$.

ε_{c1} is the strain at the maximum stress, $\varepsilon_{c1} = 0.8 \ f_{cm}^{0.31}$ with f_{cm} in MPa.

Compressive softening

There are several material models in literature that describe the softening phase which occurs after the compressive strength has been reached. One model introduced by de Borst [9] incorporated a compressive fracture energy in order to describe the compressive softening. This model is presented in Equation (4.5), see also Figure 4.5.

$$\sigma_c(\varepsilon_q) = \begin{cases} \dfrac{f_{cm}}{3}\left(1 + 4\dfrac{\varepsilon_c}{\varepsilon_{ec}} - 2\dfrac{\varepsilon_c^2}{\varepsilon_{ec}^2}\right) & \text{if } \varepsilon_c < \varepsilon_{ec} \\[3ex] f_{cm}\left(1 - \dfrac{(\varepsilon_c - \varepsilon_{ec})^2}{(\varepsilon_{uc} - \varepsilon_{ec})^2}\right) & \text{if } \varepsilon_{ec} \le \varepsilon_c < \varepsilon_{uc} \end{cases} \tag{4.5}$$

where,

ε_c is an internal damage parameter.

ε_{ec} is the equivalenet strain when the max. compressive stress is reached. $\varepsilon_{ec} = \dfrac{4}{3}\dfrac{f_{cm}}{E_c}$.

ε_{uc} is the fracture strain. $\varepsilon_{uc} = \dfrac{3G_c}{2wf_{cm}}$.

G_c is the compressive fracture energy.
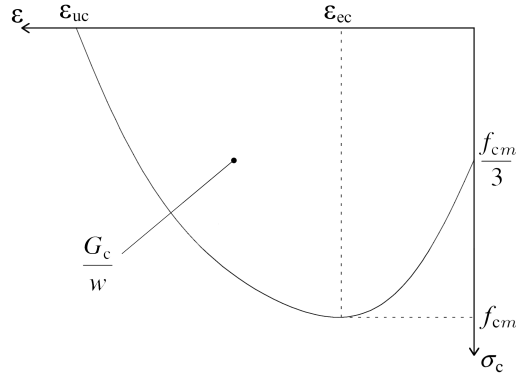
w is the element size.

Figure 4.5: Energy-based equivalent stress-strain diagram for compression.

4.2.2   Multi-axial stress

The behaviour of concrete is different under multi-axial stress compared to uni-axial stress. Concrete exposed to uni-axial compression or tension typically have a brittle behaviour whereas concrete exposed to large multi-axial compression or tension exhibit a more ductile response. Under these circumstances the main failure mechanism changes from cracking in tension and crushing in compression to be driven more by the consolidation and collapse of the microporous microstructure of the concrete [8].

Bi-axial failure development and cracking of concrete is illustrated in Figure 4.6. In the first, second and fourth quadrant the body is subjected to tensile stresses and tensile cracks develop perpendicular to the principal tensile stress [2]. Under bi-axial compression, as described in the third quadrant, the compressive strength increases by up to 25 % of the uni-axial compressive strength [19].
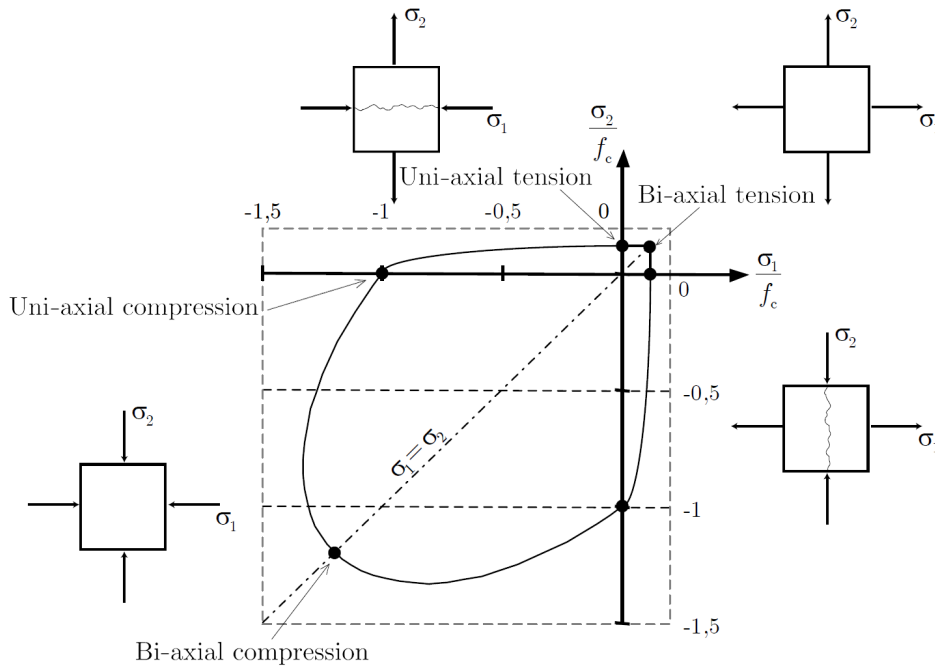

Figure 4.6: Yield criteria of concrete for plane stress conditions [19].

When subjected to tri-axial stress, concrete shows a significant increase in its compressive strength and ductile behaviour [21]. The concrete can act *quasi-brittle*, *plastic-softening* or *plastic-hardening* depending on the level of confining stress. The reason is that higher confining stress greatly reduces the possibility of bond cracking and the cement paste gets a failure mode of crushing instead of cleavage [4].

4.3 Constitutive models for concrete

4.3.1 Modes of fracture

In fracture mechanics three modes of fracture are defined, as illustrated in Figure 4.7. Mode I is a tensile opening mode with tensile stresses acting normal to the plane of the crack. Mode II is a shear or sliding mode with shear stresses acting parallel to the plane of the crack and perpendicular to the crack front. Mode III is a shearing-, or twisting mode with shear stresses parallel to the plane and parallel to the crack front. Mode I is the most common type of fracture in concrete and can in some cases occur in its pure form whereas Mode II and Mode III rarely occur in their pure forms. Instead a combination of the fracture modes is possible and common for concrete [19].
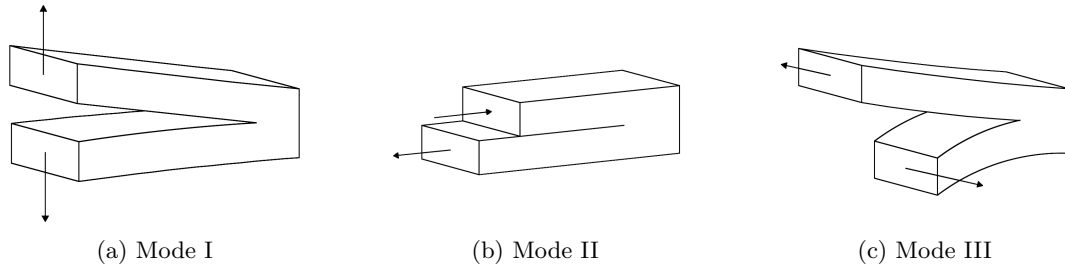

(a) Mode I   (b) Mode II   (c) Mode III

Figure 4.7: The three fracture modes according to fracture mechanics.

4.3.2 Plasticity theory

Plasticity theory is mainly used to describe the behaviour of ductile materials. However, in finite element analysis, it is also used to describe the non-linear behaviour of brittle materials [19]. According to plasticity theory the total strain, ε_{ij}, is equal to the sum of the elastic strain, ε_{ij}^{el}, and the plastic strain, ε_{ij}^{pl}.

$$\varepsilon_{ij} = \varepsilon_{ij}^{el} + \varepsilon_{ij}^{pl} \tag{4.6}$$

Yield and failure function

A yield criterion defines the threshold between elasticity and plasticity or brittle failure deformation. Various yield criteria have been proposed for both steel and concrete. A proper choice of yield criterion is vital in the design of structures. A commonly used criterion for steel is von Mises, illustrated in Figure 4.8a. For concrete, Drucker-Prager and Mohr-Coulomb are two commonly used criteria, illustrated in Figure 4.8b and Figure 4.8c respectively. Both Drucker-Prager and Mohr-Coulomb can be expressed as

$$F(\sigma) = c \tag{4.7}$$

where,

$F(\sigma)$ is a function of the stress components that is homogeneous in the first degree.

c is the cohesion.

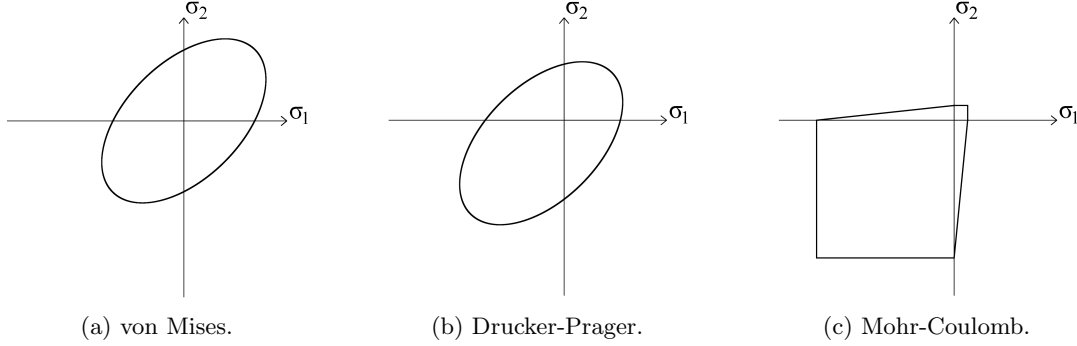(a) von Mises.   (b) Drucker-Prager.   (c) Mohr-Coulomb.

Figure 4.8: Yield criteria in the $\sigma_1\sigma_2$-plane.

However, according to Lubliner [18], both Drucker-Prager and Mohr-Coulomb criteria have notoriously poor correlation with experimental data for concrete. He suggests a modified version which combines the two criteria in which $F(\sigma)$ takes the form

$$F(\sigma) = \frac{1}{1-\alpha}\left[\sqrt{3J_2} + \alpha I_1 + \beta\langle\sigma_{max}\rangle - \gamma\langle-\sigma_{max}\rangle\right] \tag{4.8}$$

where,

J_2 is the second deviatoric stress invariant.

I_1 is the first stress invariant.

α, β and γ are dimensionless constants.

σ_{max} is the maximum stress

If $\sigma_{max} = 0$, *i.e.* bi-axial compression, Equation (4.8) is reduced to the Drucker-Prager criterion. Abaqus implements a modified version of Lubliners yield criterion which is described in more detail in Section 4.4.1.

Hardening

An elastic-perfectly plastic material subjected to uni-axial loading yields at a constant stress. A behaviour where the stress either increases or decreases as the material yields is referred to as *hardening* or *softening*. The same behaviour can be described for multi-axial loading. The stress can move along the yield surface but without changing the shape or position as long as the stress is less or equal to the yield stress. When the yield stress is reached and hardening or softening occurs the yield surface can change in size, position or both.

Any yield surface can at the start be described as

$$F(\sigma) - \sigma_Y = 0 \tag{4.9}$$

where σ_Y is the current yield stress, initially equal to the initial yield stress, σ_0. The development of the yield surface as the plastic deformation increases can be described with a *hardening law*. Two ways of defining a hardening law is that it explicitly depends on the plastic strain, referred

to as *strain hardening* or that the yield stress depends on the cumulative plastic strain which is referred to as *work hardening*. The choice of hardening law depends on the material.

Equation (4.9) can be rewritten so that it describes both types of hardening by replacing the yield stress σ_Y with a hardening function, h, according to

$$\sigma_Y = h(\kappa) \tag{4.10a}$$

$$F(\sigma) - h(\kappa) = 0 \tag{4.10b}$$

where $\kappa]$ is a hardening variable.

One possible development of the yield surface is that it expands uniformly in all directions, without any translation in the stress space. This is referred to as *isotropic hardening*, illustrated in Figure 4.9a. The development of the yield surface for isotropic hardening can be described with a yield function, f, and written as

$$f(\sigma, \kappa) = F(\sigma) - h(\kappa) \tag{4.11}$$

Another type of hardening law is *kinematic hardening*, illustrated in Figure 4.9b. The initial yield surface preserves its shape and orientation but translates its origin in the stress space as a rigid body, represented by the so-called *back stress*, σ_b. Kinematic hardening is required in order to model the so-called *Bauschinger effect* [12]. The Bauschinger effect describes the change of a materials tensile yield strength related to change in compressive yield strength. For example will an increase in tensile yield strength be at the expense of its compressive yield strength [27].

Most materials can be described by a combination of isotropic and kinematic hardening, called *mixed hardening* where the yield surface can both change in shape and translate in the stress space at the same time. This can be described with

$$f(\sigma, \sigma_b, \kappa) = F(\sigma - \sigma_b) - h(\kappa) \tag{4.12}$$

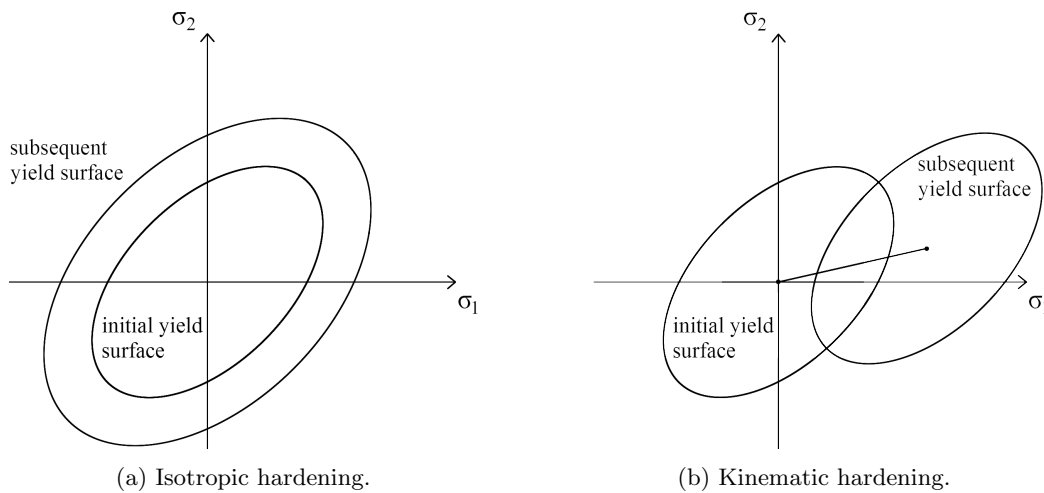(a) Isotropic hardening.   (b) Kinematic hardening.

Figure 4.9: Isotropic and kinematic hardening for the von Mises criterion.

Flow Rule

The relation between the stress-strain relation and the yield surface is defined with a *flow rule*. It defines the direction of plastic flow and supplements the yield criterion by describing the development of the plastic flow [12].

A flow rule is defined as

$$d\varepsilon_{ij}^{pl} = d\lambda \frac{\partial g}{\partial \sigma_{ij}} \tag{4.13}$$

where,

$\dfrac{\partial g}{\partial \sigma_{ij}}$ is the gradient of the plastic potential surface and defines the direction of the plastic strain increment $d\varepsilon_{ij}^{pl}$.

$d\lambda$ is a loading parameter and defines the length or magnitude of the vector.

If the plastic potential surface, g, takes the same shape as the current yield surface it is called an *associated flow rule* as the plastic flow is associated with the yield surface. When the plastic potential surface and yield surface do not coincide the flow rule is *non-associated* [4].

4.3.3 Damage theory

The growth of micro-cracks and voids in concrete damage models is represented by a set of variables which alter the elastic and plastic behaviour of the material. The stress-strain relation for damage models is defined by [19]

$$\boldsymbol{\sigma} = \boldsymbol{D^s} \colon \boldsymbol{\varepsilon} \tag{4.14}$$

where,

$\boldsymbol{\sigma}$ is the stress tensor.

$\boldsymbol{D^s}$ is the stiffness tensor of the damaged material.

$\boldsymbol{\varepsilon}$ is the strain tensor.

Isotropic damage model

The isotropic damage model describes the degradation of a material as a result of micro-cracking. The damage parameter, d, acts as a stiffness reduction factor and is equal to 0 for the undamaged state and 1 for the completely damaged state. For an isotropic damage model the stress-strain relation shown in Equation (4.14) takes the form of [3]

$$\sigma = (1 - d)D^0 \colon \varepsilon \tag{4.15}$$

Where D^0 is the stiffness tensor of the undamaged material.

Damage-coupled plasticity theory

According to the damage theory described in Section 4.3.3, the damage strain is fully recovered after unloading unlike the equivalent plastic strain. Due to sliding and development of micro-cracks some permanent strain remains in the concrete after unloading which should be included in the plasticity theory [19]. Coupling between damage and plasticity has been found to be necessary in order to capture the observed behaviour of concrete in experimental tests [25].

A coupled damage plasticity model could use the effective stress concept in Equation (4.16) developed by [13].

$$\sigma = (1-d)D^0 : (\varepsilon - \varepsilon^{pl}) \tag{4.16}$$

where ε^{pl} is the plastic equivalent strain.

The plastic yield function is formulated in terms of effective stress according to the effective stress concept. The effective stress, $\hat{\sigma}$, is calculated according to [19]

$$\hat{\sigma} = \frac{\sigma}{1-d} \tag{4.17}$$

4.3.4   Crack propagation

The non-linear material properties of concrete can be described by several different theories in numerical analyses. The modelling of crack propagation is generally done by one of two approaches, first introduced by Rashid [31] and Ngo [24]. Cracks can either be considered as *discrete* with a separation of the two crack surfaces or with a continuum approach where the cracks are considered *distributed* (smeared) over the elements, as illustrated in Figure 4.10. When analysing the non-linear material properties of concrete in large structures the distributed (smeared) crack approach is the most common technique used today [20].
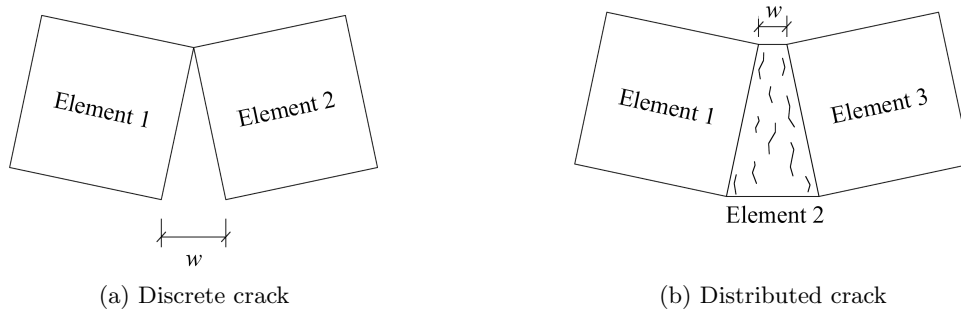

(a) Discrete crack   (b) Distributed crack

Figure 4.10: Discrete and distributed crack.

4.4   Constitutive models in Abaqus

All of the analyses were performed using the finite element program Abaqus 2016. There are three constitutive models available in Abaqus for modelling the non-linear behaviour of concrete. *Concrete smeared cracking* and *concrete brittle cracking* are both based on the smeared crack approach. Concrete smeared cracking can only be used in static analyses whereas concrete brittle cracking can only be used in dynamic analyses. The third constitutive model, *concrete damaged plasticity*, is based on a combination of damage and plasticity theory and can be used for both static and dynamic analyses [8].

4.4.1   The concrete damaged plasticity model

The concrete damaged plasticity model (CDP) in Abaqus is designed for analyses with cyclic loading of reinforced concrete, alternating compression and tension and allows for stiffness recovery which makes it a suitable model for the analyses. The CDP model was therefore used to describe the non-linear behaviour of concrete.

The CDP model assumes that the main fracture mechanisms in concrete are rupture for tension and crushing for compression. The model is designed for analyses with cyclic loading of reinforced concrete, alternating compression and tension and allows for stiffness recovery. The stress-strain relationships in the CDP model under uni-axial tension and compression are defined as

$$\sigma_t = (1 - d_t)E_0(\varepsilon_t - \varepsilon_t^{pl}) \tag{4.18a}$$

$$\sigma_c = (1 - d_c)E_0(\varepsilon_c - \varepsilon_c^{pl}) \tag{4.18b}$$

where,

σ_t, σ_c is the stress in tension and compression.

d_t, d_c is the degradation factor in tension and compression.

E_0 is the initial (undamaged) elastic modulus.

$\varepsilon_t^{pl}, \varepsilon_c^{pl}$ is the equivalent plastic strain for tension and compression.

The CDP model assumes a reduction of the elastic modulus according to Equation (4.19). The expression is true for both the compressive and tensile side of the load cycle [8].

$$E = (1 - d)E_0 \tag{4.19}$$

The response and unloading curves for uni-axial compression and tension in the CDP model is characterised by damage plasticity as shown in Figure 4.11.

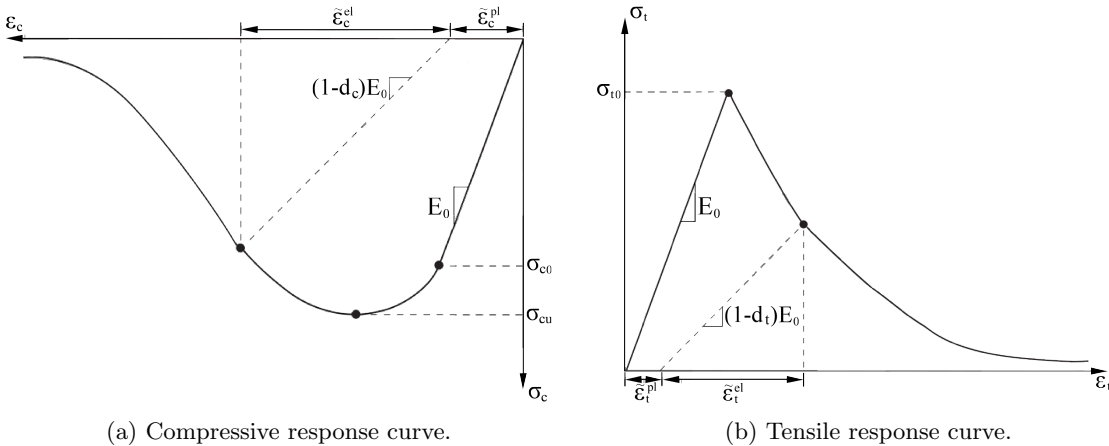(a) Compressive response curve.   (b) Tensile response curve.

Figure 4.11: Response curves for uni-axial loading in concrete according to the CDP model. Reproduction from Abaqus 6.14 Analysis User's Guide [8].

The stress-strain response under uni-axial compression is linear elastic until the intial yield, σ_{c0}, is reached. After this point the response curve enters the plastic regime which is characterised by stress hardening until the ultimate stress, σ_{cu}, is reached followed by strain softening. The

stress-strain response under uni-axial tension is linear elastic until the failure stress, σ_{t0}, is reached and the propagation of microcracks is initiated in the concrete [7].

In most quasi-brittle materials, including concrete, observations has shown that the compressive stiffness recovers as the load changes from tension to compression and cracks close. Tensile stiffness however, does not recover once micro-cracks have developed as the load changes from compression to tension. This behaviour corresponds to the default values of the CDP model in Abaqus and is defined by the stiffness recovery factors $w_t=0$ and $w_c=1$ [8]. The CDP model is illustrated in Figure 4.12 for a uni-axial load cycle from tension to compression to tension.
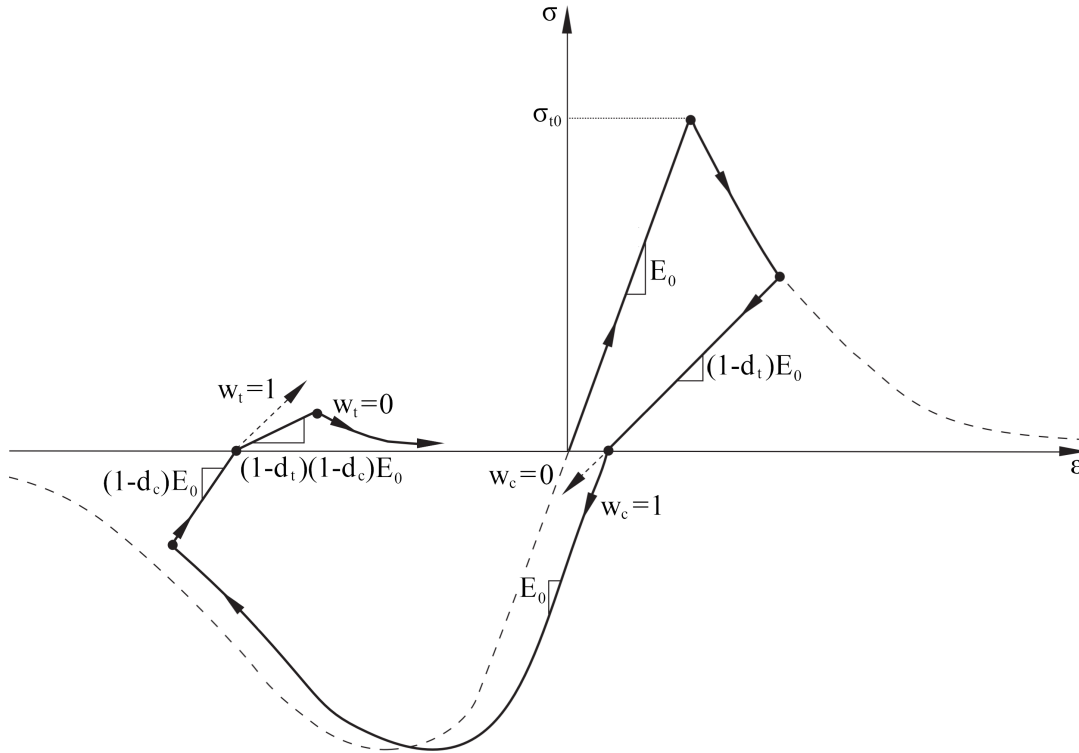
Figure 4.12: Uni-axial load cycle (tension-compression-tension) with default values for the stiffness recovery factors $w_t=0$ and $w_c=1$. Reproduction from Abaqus 6.14 Analysis User's Guide [8].

Yield criteria

Abaqus uses a bi-axial yield criterion for concrete in plane stress conditions in the CDP model based on the yield function by Lubliner as described in Section 4.3.2, but with modifications proposed by Lee and Fenves [14] to account for different evolution of strength under tension and compression. The yield surface is illustrated in Figure 4.13,
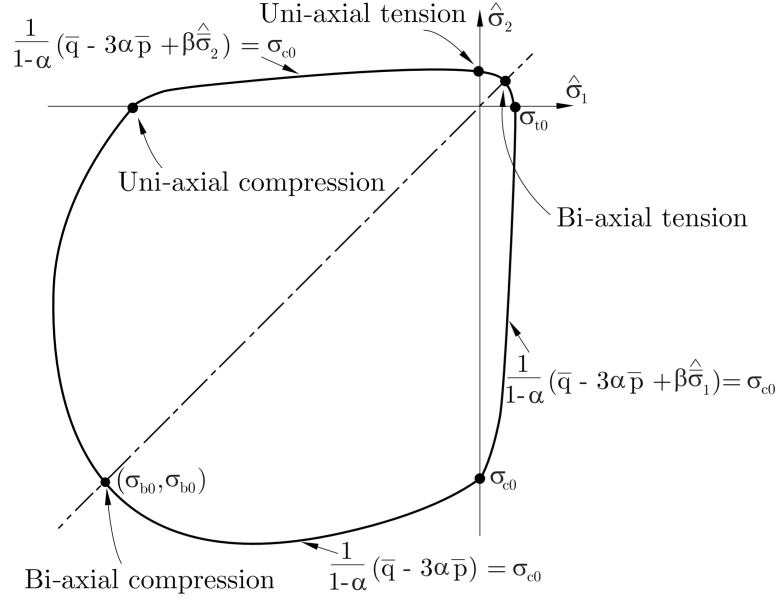
Figure 4.13: Bi-axial yield surface in the CDP model. Reproduction from Abaqus 6.14 Analysis User's Guide [8].

where,

α is a dimensionless material constant. $\alpha = \dfrac{f_{b0} - f_{c0}}{2f_{b0} - f_{c0}}$ where $0 \leq \alpha \leq 0.5$.

σ_{c0} is the initial uni-axial compressive yield stress.

σ_{b0} is the initial equibiaxial compressive yield stress.

σ_{t0} is the uni-axial tensile stress at failure.

$\bar{p}$ is the hydrostatic pressure, which is a function of the first stress invariant I_1.
$\bar{p} = -I_1/3 = -(\sigma_{11} + \sigma_{22} + \sigma_{33})/3$.

$\bar{q}$ is the von Mises equivalent effective stress. $\bar{q} = \sqrt{\frac{3}{2}S:S} = \sqrt{3J_2}$ where J_2 is the second deviatoric stress invariant $J_2 = \sigma_{11}^2\sigma_{22}^2 - \sigma_{11}\sigma_{22}$ for bi-axial loading and S is the effective deviatoric stress tensor $S = \bar{\sigma} + pI$.

β is a dimensionless coefficient. $\beta = \dfrac{\hat{\bar{\sigma}}_c(\hat{\varepsilon}_c^p)}{\hat{\bar{\sigma}}_t(\hat{\varepsilon}_t^p)}(\alpha - 1) - (\alpha + 1)$.

$\hat{\bar{\sigma}}_c(\hat{\varepsilon}_c^p)$ is the effective compressive cohesion stress.

$\hat{\bar{\sigma}}_t(\hat{\varepsilon}_t^p)$ is the effective tensile cohesion stress.

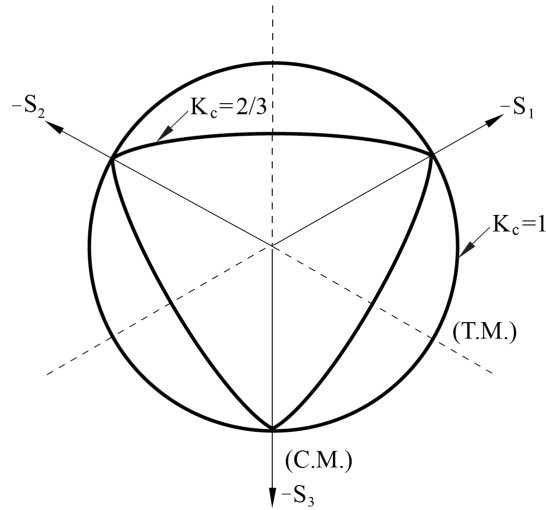Typical yield surfaces in the deviatoric plane are presented in Figure 4.14

Figure 4.14: Yield surfaces in the deviatoric plane, corresponding to different values of K_c. Reproduction from Abaqus 6.14 Analysis User's Guide [8].

where,

K_c is defined in the Abaqus Analysis User's Guide [8] as the ratio of the second stress invariant on the tensile meridian, to that on the compressive meridian, at initial yield for any given value of the pressure invariant p such that the maximum principal stress is negative, $\hat{\sigma}_{max} < 0$; it must satisfy the condition $0.5 < K_c \leq 1.0$.

Flow rule

The CDP model uses a non-associative flow rule and the Drucker-Prager hyperbolic function to describe the flow potential G [8]

$$G = \sqrt{(\epsilon\, f_{t0} \tan\psi)^2 + \bar{q}^2} - \bar{p} \tan\psi \tag{4.20}$$

where,

ϵ is the eccentricity, which defines the rate at which the plastic potential function approaches the asymptote. The flow potential approaches a straight line as the eccentricity approaches zero.

ψ is the dilation angle, measured in the p-q plane at high confining pressure.

Figure 4.15 illustrates the flow potential which approaches a straight line as the eccentricity approaches zero. If the dilation angle, ψ is equal to the inner friction angle of the material, the flow rule becomes associative [8]. In literature the value of the dilatation angle for reinforced concrete is given as 30° and the eccentricity default value for the CDP model is set to 0.1 [18].
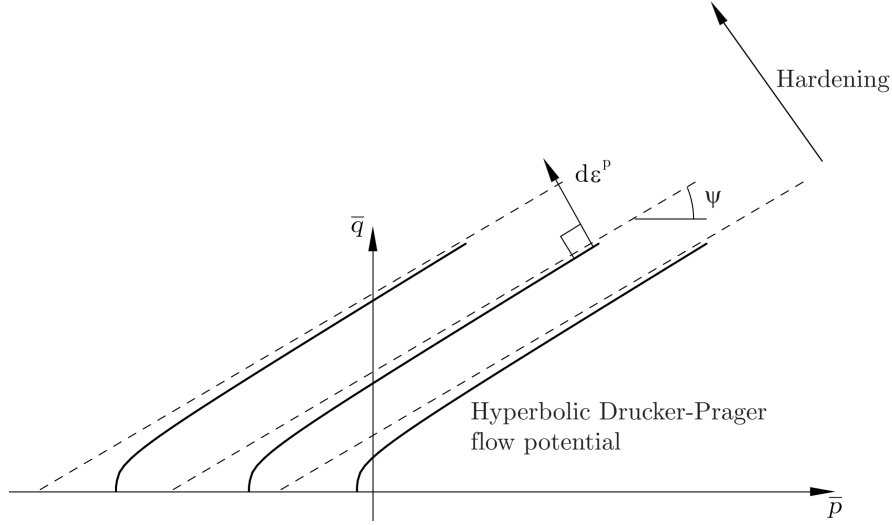
Figure 4.15: The Drucker-Prager hyperbolic plastic potential function in the $\bar{p}$-$\bar{q}$ plane. Reproduction from Abaqus 6.14 Analysis User's Guide [8].

4.5   Quasi-static analysis

Finite element problems can be solved with either implicit or explicit integration in Abaqus which both has their own advantages. Implicit integration is mainly used for linear elastic analyses with relatively small deformation which easily obtain convergence. Explicit integration is more capable in analyses of large structures with large deformations and more complicated contacts. Explicit integration is less computationally expensive for these kinds of problems as it uses a reduced-order integration [8]. Solving non-linear finite element problems introduces a number of difficulties that has to be resolved in order to establish convergence and a reliable solution. Performing these types of analyses as quasi-static can in many cases be beneficial. Quasi-static analyses refers to a technique were the analysis is performed with a dynamic solver and the loads are applied gradually in order to reduce the kinetic energy and thereby reducing significant inertia effects [20].

4.5.1   Explicit time integration

The explicit dynamic analysis procedure implements an explicit integration rule with the use of diagonal element mass matrices. The equations of motion for the body are integrated using the explicit central difference integration rule,

$$\dot{\mathbf{u}}^{(i+\frac{1}{2})} = \dot{\mathbf{u}}^{(i-\frac{1}{2})} + \frac{\Delta t^{i+1} + \Delta t^{(i)}}{2}\ddot{\mathbf{u}}^{(i)}, \tag{4.21a}$$

$$\mathbf{u}^{(i+1)} = \mathbf{u}^{(i)} + \Delta t^{(i+1)}\dot{\mathbf{u}}^{(i+\frac{1}{2})} \tag{4.21b}$$

where,

$\dot{\mathbf{u}}$	is the velocity.
$\ddot{\mathbf{u}}$	is the acceleration.
i	is the increment number.
Δt	is the incremental time.

The central difference integration is explicit since the kinematic state can be advanced by using known values of $\dot{\mathbf{u}}^{(i-\frac{1}{2})}$ and $\ddot{\mathbf{u}}^{(i)}$ from previous increments. The key to computational efficiency of the explicit procedure is the diagonal mass matrices since its inversion is tri-axial in the computation of the acceleration,

$$\ddot{\mathbf{u}}^{(i)} = \mathbf{M}^{-1} \cdot (\mathbf{F}^{(i)} - \mathbf{I}^{(i)}) \tag{4.22}$$

where,

$\mathbf{M}$ is the diagonal mass matrix.

$\mathbf{F}$ is the applied load vector.

$\mathbf{I}$ is the internal force vector.

The explicit method integrates through time by many small time increments. Estimating a stable time increment is of great importance since a too large increment will result in that the integration fails and if the increment is to small, the computational time will become costly.

A stable time increment can be calculated by [8]

$$\Delta t \approx \frac{L_{min}}{c_d} \tag{4.23}$$

where,

L_{min} is the smallest element dimension in the mesh.

c_d is the dilatational wave speed.

The dilatational wave speed can for an isotropic, elastic materials be expressed in terms of Young's modulus, E, the density, ρ, and Poisson's ratio, ν as [7]

$$c_d = \sqrt{\frac{E(1-\nu)}{\rho\,(1+\nu)(1-2\nu)}} \tag{4.24}$$

The explicit integration method generally requires very small time increments in order to produce an accurate result. Since the time increments are so small, it may take many thousands of increments in order to complete an analysis. There are two approaches in Abaqus designed to decrease the number of increments needed to complete an analysis. The two methods are *increasing load rates* and *mass scaling*.

4.5.2 Loading rate

The loading rate in quasi-static analyses is required to be as smooth as possible since large changes would induce high influence from dynamic effects. By increasing the loading rate the time scale can be artificially reduced. Abaqus has a built-in smooth step amplitude curve which automatically creates a smooth loading amplitude by connecting each data pair with curves whose first and second derivatives are smooth and equal to zero for each data point. An example of a smooth step amplitude curve is illustrated in Figure 4.16.
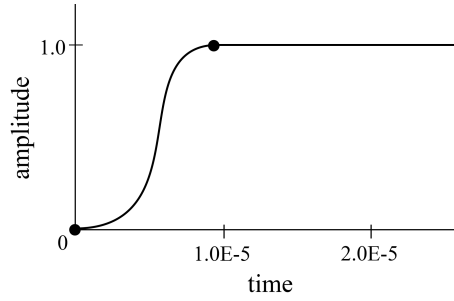
Figure 4.16: Example of a smooth step amplitude curve. Reproduction from Abaqus 6.14, Getting started with Abaqus [6].

4.5.3 Mass scaling

Mass scaling is an effective tool for reducing CPU-time in quasi-static, explicit analyses. By artificially increasing the mass of the model the time increments can be increased. Mass scaling can be applied globally to the entire model or on a specific part as either *fixed mass scaling* or *variable mass scaling*. In regions which require smaller time increments and more attempts to converge, the density or mesh size is increased [8]. The maximum allowed mass scaling in which the inertia forces are still insignificant should be applied in order to achieve the shortest CPU-time and still get a reliable result.

4.5.4 Energy balance

A general way of evaluating if a simulation produces an appropriate quasi-static response is by studying the various model energies. Abaqus/Explicit uses a energy balance equation according to

$$E_I + E_V + E_{FD} + E_{KE} + E_{IHE} - E_W - E_{PW} - E_{CW} - E_{MW} - E_{HF} = E_{total} \qquad (4.25)$$

where,

E_I	is the internal energy.
E_V	is the viscous energy dissipated.
E_{FD}	is the frictional energy.
E_{KE}	is the kinetic energy.
E_{IHE}	is the internal heat energy.
E_W	is the work done by the externally applied loads.
E_{PW}	is the work done by contact penalties.
E_{CW}	is the work done by constraint penalties.
E_{MW}	is the work done by propelling added mass.
E_{HF}	is the external heat energy through external fluxes.

The sum of the energy components should be equal to a constant. However, in the numerical model E_{total} is only approximately constant, generally with an error less than 1 %. In order to determine if a simulation is quasi-static the work applied by external forces is compared with the internal energy of the system. If these are close to equal we have a quasi-static simulation.

The viscously dissipated energy is generally small unless a viscolelastic material, discrete dashpot or damping is used. Inertial forces are neglectable since the velocity is small in a quasi-static state. Coroally with the two statements above the kinematic energy is small. To achieve a quasi-static analysis, the kinematic energy of a deforming material should on a global scale be no more than 5 - 10 % of its internal energy throughout most of the process [8].

Chapter 5

Reference dam input data

In this chapter, input data used to carry out the analysis are presented. This includes geometry, material properties, temperature data and heat transfer properties which were defined and provided by the formulators [22].

5.1 Geometry

The reference dam has a crest length of 170 m and a maximum height of 45.5 m. The thickness of the dam body varies with height, between 5.4 m at the base to 2.5 m at the crest. The dam body follows a continuous arch with the radius of 110 m. It consists of three parts, spillway, dam body and left support. The total length of the dam, with these included, is 270 m.

The spillway has a total height of 30 m and a total width of 35 m which is divided into two spillway sections about 12 m each. The rock foundation is roughly 90 × 210 m with a height varying between 18 m - 60 m. The geometry of the reference dam and rock foundation were provided by the formulators [22] and is illustrated in Figure 5.1.
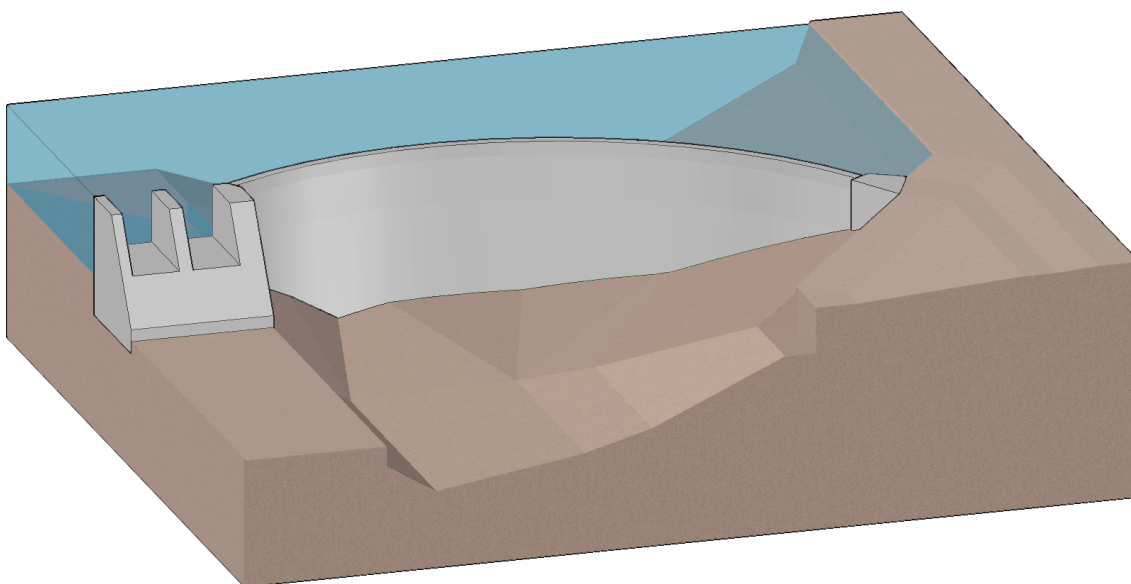
Figure 5.1: Idealized geometry of the reference dam and underlying rock.

The dam body is reinforced in both the upstream and downstream surface. The vertical reinforcement on the upstream surface consists of one rebar layer with a diameter of 25 mm and a spacing of 300 mm. The vertical reinforcement on the downstream surface consists of two rebar layers of 25 mm with a spacing of 300 mm and a spacing of 100 mm between the layers. The horizontal reinforcement consists of one layer of bars on both the upstream and downstream surface with 25 mm in diameter and a spacing of 300 mm. The concrete cover is 100 mm on both the upstream and the downstream side. A schematic illustration of the reinforcement is presented in Figure 5.2.
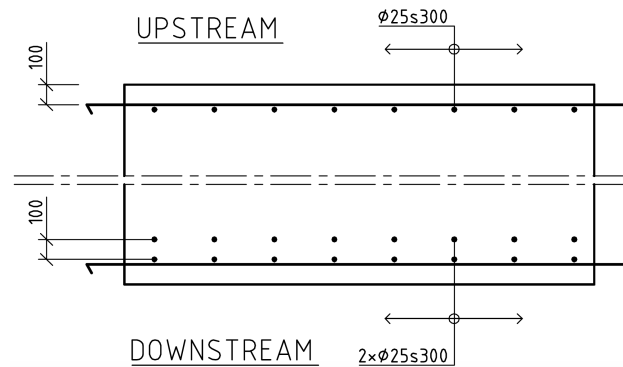
Figure 5.2: Schematic illustration of the reinforcement in the dam body [22].

No information of the reinforcement in the spillway or support was provided by the formulators.

5.2 Material properties

The concrete corresponds to concrete grade C30/C37 and the reinforcement is assumed to correspond to the old Swedish standard KS 40. The rock is assumed to act linear-elastic without consideration of fracture, shear or crush zones. The material properties in Table 5.1 corresponds to the mean values of the concrete, reinforcement and rock.

Table 5.1: Material properties of the concrete, reinforcement and rock [22].

Property	Unit	Concrete C30/37	Reinforcement KS 40	Rock -
Density	kg/m^3	2300	7800	2700
Elastic modulus	GPa	33	200	40
Poisson's ratio	-	0.2	0.3	0.15
Compressive strength	MPa	38	-	-
Tensile strength	MPa	2.9	-	-
Yield stress	MPa	-	360	-
Ultimate strength	MPa	-	600	-
Ultimate strain	-	-	0.15	-
Thermal expansion	K^{-1}	10^{-5}	10^{-5}	10^{-5}
Thermal conductivity	W/(mK)	2	39	3
Stress/strain free temperature	°C	4	4	4
Specific heat capacity	J/(kgK)	900	450	850
Fracture energy *	Nm/m^2	140	-	-

* The fracture energy was calculated using Equation (4.3).

5.3   Temperature data

The ambient air and water temperatures in the reservoir are based on temperature statistics on site over the last 40 years. Extreme temperature values with short duration has little to no effect on the structural behaviour, therefore the temperature values have been averaged to give the maximum and minimum average temperatures over a 7 day period for each month. The temperature values are presented in Table 5.2 and in Figure 5.3 where the temperatures are interpolated linearly between the months. Measurements on the temperature of the water in the reservoir has shown that the temperature is more or less constant with depth, which was also assumed in the analyses.

Table 5.2: Monthly temperatures on site for the ambient air and water.

Month	Maximum temperatures (Figure 5.3a)		Minimum temperatures (Figure 5.3b)	
	Air (°C)	Water (°C)	Air (°C)	Water (°C)
Jan	-0.2	0.0	-25.8	0.0
Feb	0.6	0.4	-23.6	0.0
Mar	2.4	1.7	-15.7	0.0
Apr	6.5	4.6	-6.5	0.0
May	14.8	10.4	1.1	0.8
Jun	18.5	13.0	6.6	4.6
Jul	19.7	13.8	10.0	7.0
Aug	18.0	12.6	7.3	5.1
Sep	12.6	8.8	1.9	1.3
Oct	8.0	5.6	-6.4	0.0
Nov	3.1	2.2	-15.9	0.0
Dec	0.6	0.4	-23.8	0.0
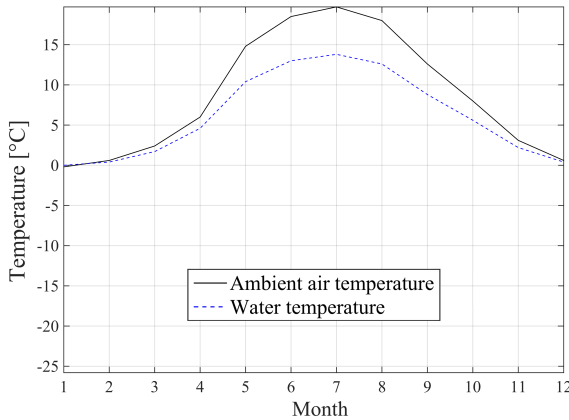
(a) Maximum temperatures for each month.
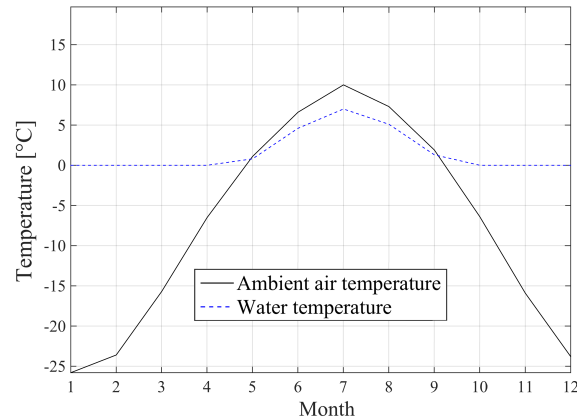
(b) Minimum temperatures for each month.

Figure 5.3: Maximum and minimum ambient air and water temperatures for each month.

5.4   Heat transfer properties

Table 5.3 provides the convective heat coefficients used in the analyses. The downstream surface, have a heat insulating material installed giving it a lower convective heat coefficient compared to the other concrete surfaces exposed to air.

Table 5.3: Convective heat transfer properties.

Interface	Convective heat coefficient [W/(m^{2}K)]
Insulated wall - air	4
Concrete - air	13
Concrete - water	500
Rock - air	13
Rock - water	500

Chapter 6

Method of analysis

The work was divided into three types of analyses, thermal analysis, linear mechanical analysis and non-linear mechanical analyses. This chapter describes the method of analysis for each type. Interactions and boundary conditions, application of loads, description of the mesh and non-linear material modelling are presented.

6.1   Thermal analyses

The purpose of the thermal analyses was to determine the temperature distribution in the dam due to the seasonal temperature variations. The main sources of external temperatures acting on dams are the ambient air temperature on the downstream surface, and the water temperature on the upstream surface. The results from the thermal analyses were used as input data in the linear and non-linear mechanical analyses to calculate the stresses, displacements and crack propagation caused by the temperature variation.

The thermal analyses were performed as transient analyses since it may take a significant time for a massive concrete structure to reach a steady state condition. The analyses were done in Abaqus/Standard as uncoupled heat transfer analyses.

6.1.1   Interaction and boundary condition

The different properties in convective heat transfer were modelled in Abaqus with surface film conditions with the convective heat coefficients presented in Table 5.3. The temperatures were applied on surfaces according to Figure 6.1, where the red area represents surfaces exposed to ambient air temperatures, the yellow area represents the heat insulated downstream surface and the blue area represents surfaces exposed to water temperatures.

The influence of the reinforcement was not considered in the heat transfer analysis and was therefore not included in the model [8]. The temperatures were instead applied on to the reinforcement in the mechanical analyses with the rest of the model. The outer boundaries were modelled as completely insulated, preventing any heat transfer out of the model. A reference temperature, T_{ref}, was set to the stress-strain free temperature of $4°C$ for the whole model and constitutes the initial temperature value used in the thermal analyses.

(a) Surface areas subjected to air.   (b) Surface areas subjected to water.
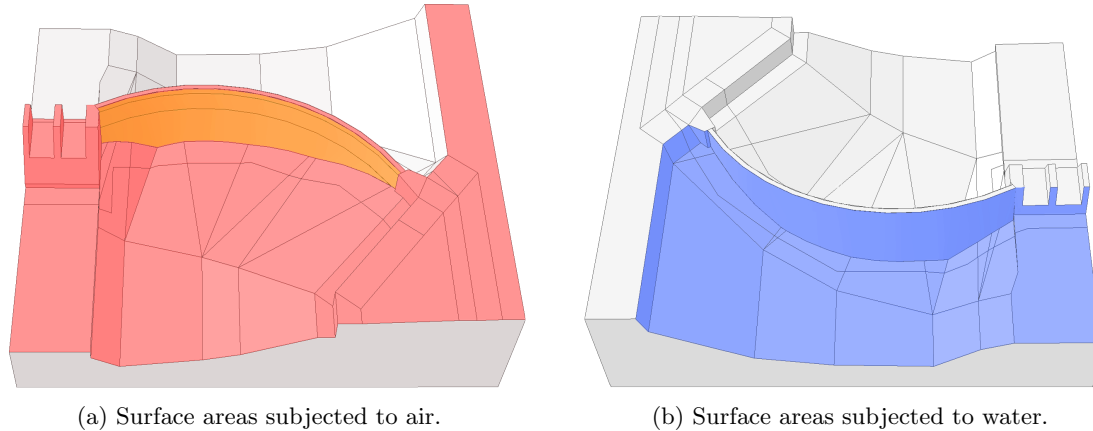
Figure 6.1: Surface areas subjected to air and water temperatures.

The temperature variations were applied in Abaqus with amplitude curves. Non-linear FE-analyses are history dependent and different combination of thermal data will provide different results. The combinations used for the non-linear analyses are discussed in Section 6.3.

6.1.2   Mesh

The result from the thermal analyses were to be used as input for the linear and non-linear mechanical analyses. It was therefore advantageous to use the same mesh for the thermal and the subsequent mechanical analyses to get a more accurate temperature distribution in the mechanical analyses. The same element discretisation is therefore used as in the linear and non-linear analyses. The element discretisation used in the linear and non-linear analyses are discussed in Section 6.2.5 and Section 6.3.7 respectively. The element types used in the thermal analysis are in Abaqus denoted DC3D8 and DC3D10.

6.2   Linear mechanical analysis

The purpose of the linear mechanical analysis was to calculate the displacement of the dam and to identify areas that may be subjected to cracking. The displacement is to be compared to the calculated displacement from the non-linear mechanical analyses in order to study the difference in result between the two approaches.

6.2.1   Linear material modelling

Abaqus requires three material properties in order to define a linear elastic material, *Young's modulus*, *Poisson's ratio* and the *density* for each material. Taking into consideration thermal effects requires an additional three parameters, the *specific heat capacity*, *thermal conductivity* and the *thermal expansion* are also needed. The values for each of these parameters are presented in Table 5.1.

6.2.2   Interactions and boundary conditions

Simplifications were made for the foundation geometry of the FE-model compared to the actual dam. The actual dam is excavated into the rock where the support is acting as a hinge, *i.e.* allowing rotation but preventing translations. In the FE-model the foundation was modelled as a flat surface, illustrated in Figure 6.2 where the squiggly arrow in the figures indicates the water flow direction.

(a) Geometry of the real dam.   (b) Simplified geometry in the FE-model.
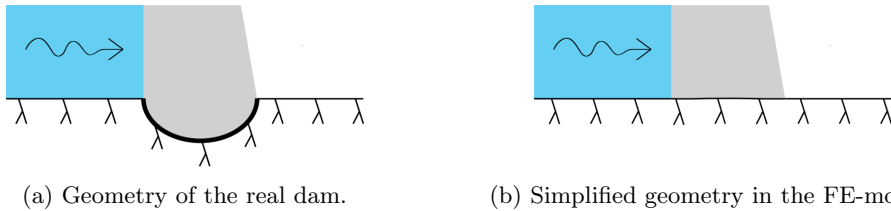
Figure 6.2: Interaction between the dam and rock for the real dam and in the FE-model [22].

The interaction between the dam body and rock was modelled with a tie constraint along the downstream side, as illustrated in Figure 6.3, allowing rotation but no translation in order to resemble the behaviour of the real dam-foundation.
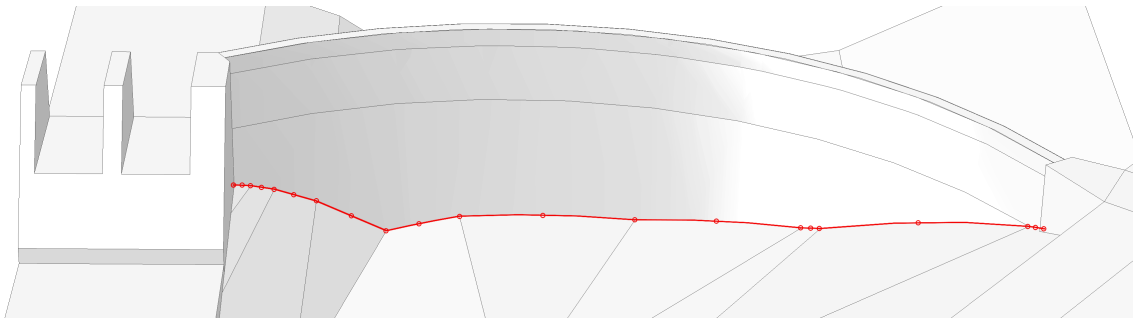
Figure 6.3: Tie constraint between the dam and rock modelled along the bottom side of the downstream surface highlighted in red.

The rock, spillway and the support were merged together as one part. The spillway and support were tied together with the dam body using tie constraints on the areas illustrated in Figure 6.4. The outer boundary condition was modelled along the bottom and outer sides of the rock as an encastre, restricting translation and rotation in all directions. This includes the outer boundary of the spillway as well.

(a) Tie constraint between the spillway and dam body.

(b) Tie constraint between the support and dam body.
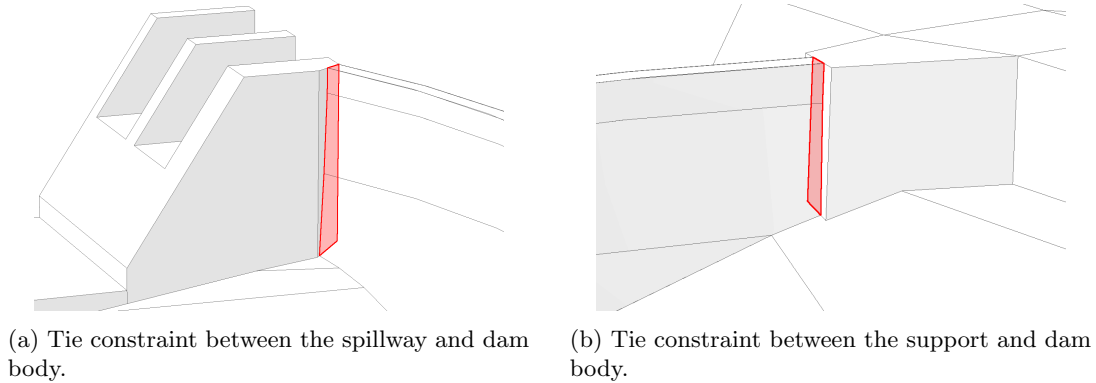
Figure 6.4: Tie constraints between the dam body, spillway and left support highlighted in red.

6.2.3   Applying loads

The loads in the linear mechanical analysis were applied in three consecutive steps. The gravity load was applied first, followed by the hydrostatic water pressure and finally the temperature loads.

The gravity load was applied to the dam body, spillway and support with a gravity function in Abaqus. No gravity load was applied to the rock mass since no consideration was taken to the behaviour of the foundation and any settling due to self-weight was assumed to have already taken place. The hydrostatic pressure was applied on the areas according to Figure 6.5 with an analytical field function describing the increase of hydrostatic pressure with depth according to Equation (2.2). The water surface level in the reservoir was assumed to reach the crest of the dam at all time. The node temperature was imported from the thermal analysis into the model in order to calculated the stress caused by thermal expansion.
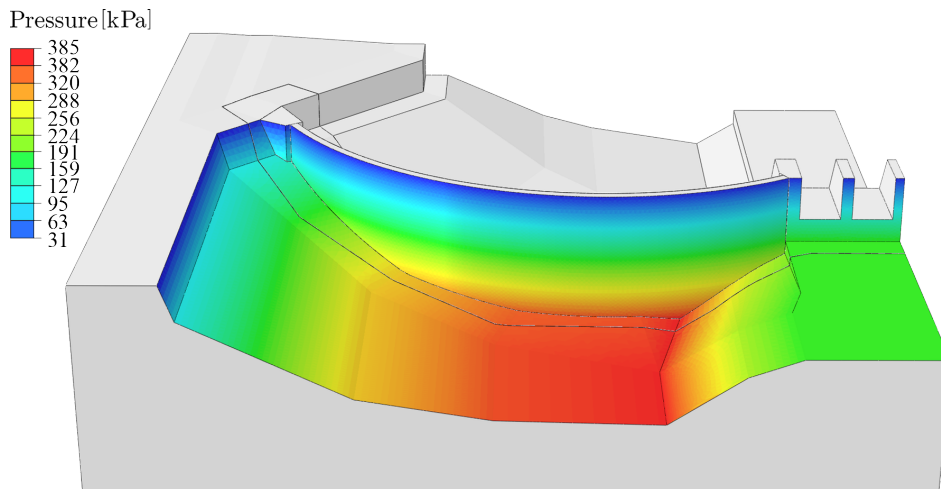
Figure 6.5: Applied hydrostatic water pressure.

6.2.4   Convergence study

A convergence study was performed in order to obtain a suitable element mesh size. The convergence study involved gravity and hydrostatic pressure loads and the element length was halved

until the solution was assumed to have converged, *i.e* the solution changed less than 5 % between two mesh refinements.

The displacement and maximum principal stress along the three lines, illustrated in Figure 6.6 were compared between the different element sizes. The study resulted in an element size of 2 m for the dam, spillway and support. For further details on the results obtained in the convergence study see Appendix.
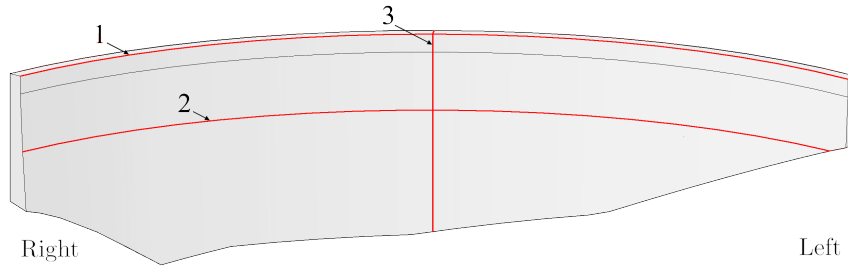
Figure 6.6: Three lines highlighted in red, on the downstream surface used to extract the calculated radial displacements of the dam. (1) At the crest. (2) A line 14 meter below the crest. (3) A vertical line in the centre section on the downstream surface.

6.2.5   Mesh

The dam body was modelled with 8 node linear hexahedral solid elements, C3D8R. The rock, spillway and support were meshed with 10 node quadratic tetrahedral solid elements, C3D10, due to their more complex geometry.

The reinforcement was modelled as embedded quadrilateral membrane elements, M3D4R, which were superimposed on the mesh of the concrete elements allowing the concrete behaviour to be considered independently. Membrane elements are often used to represent thin surfaces in space. They have an in-plane strength but no out-of-plane bending or transverse shear stiffness. Membrane elements can be used to represent thin stiffening components, making it a good alternative for modelling reinforcing layers in a continuum [7]. No reinforcement was modelled in the spillway or support. As the focus of this work was to evaluate the deformation and crack propagation in the dam body this simplification was assumed to have a negligible impact on the results.

Abaqus has a function for shell and membrane elements called *rebar*, recommended to use if the reinforcing layer is made up of chords which was used in the model. The rebar function allows for specification of multiple layers of reinforcement in membrane, shell and surface elements and the possibility to specify properties such as cross-section area of each rebar and rebar spacing. The rebar layer is treated as a smeared layer in Abaqus. The element length of the rebar layer was set to 2 m in order for the elements in the vicinity of the embedded rebar layer to easier find elements that contain embedded nodes and create constrains for these to the host elements [7]. The element types are illustrated in Figure 6.7.

(a) 8 node linear hexahedral element.

(b) 10 node quadratic tetrahedral element.
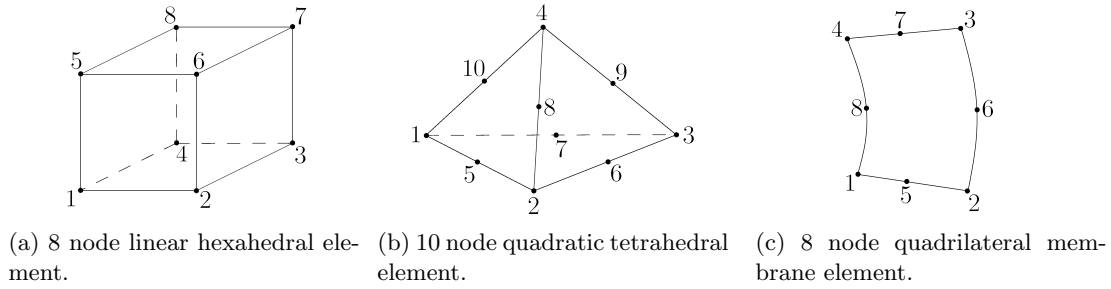
(c) 8 node quadrilateral membrane element.

Figure 6.7: Element types used in the dam, rock and reinforcement.

The element length of the rock was gradually increased from a length of 2 m under the dam to 20 m at the outer boundaries of the model. This approach reduces the total number of elements in the model without compromising the mesh refinement in areas which requires a higher mesh density, *i.e*, in the dam body, spillway and support. The final meshes of the linear mechanical analysis are presented in Figure 6.8 and Figure 6.9. Detailed information on the type, size and quantity of the different parts are presented in Table 6.1.
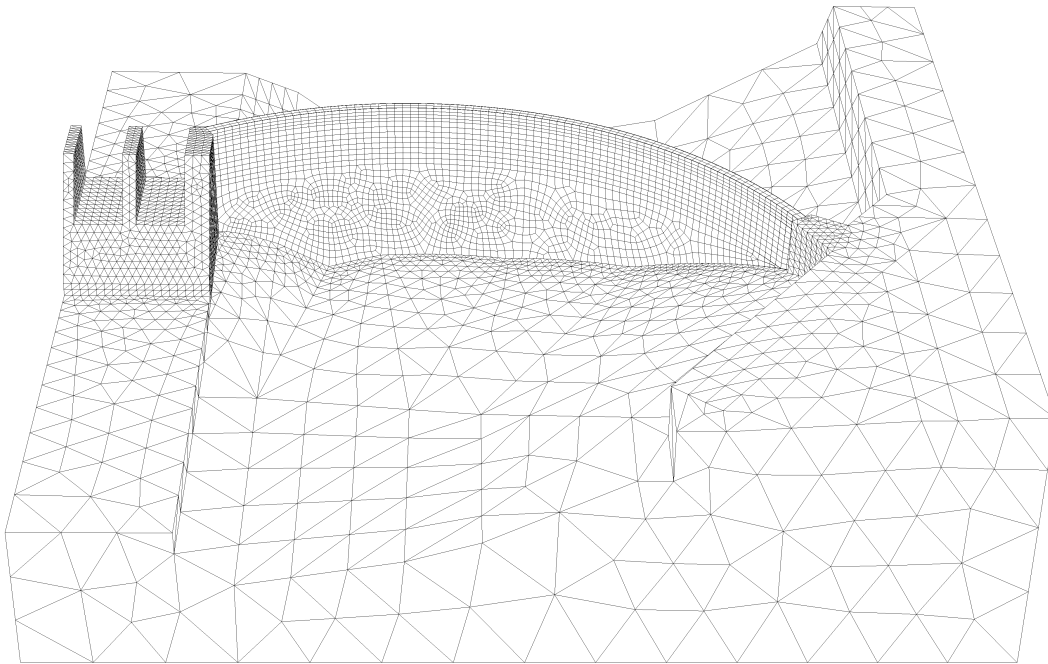
Figure 6.8: Mesh used in the linear mechanical analysis.
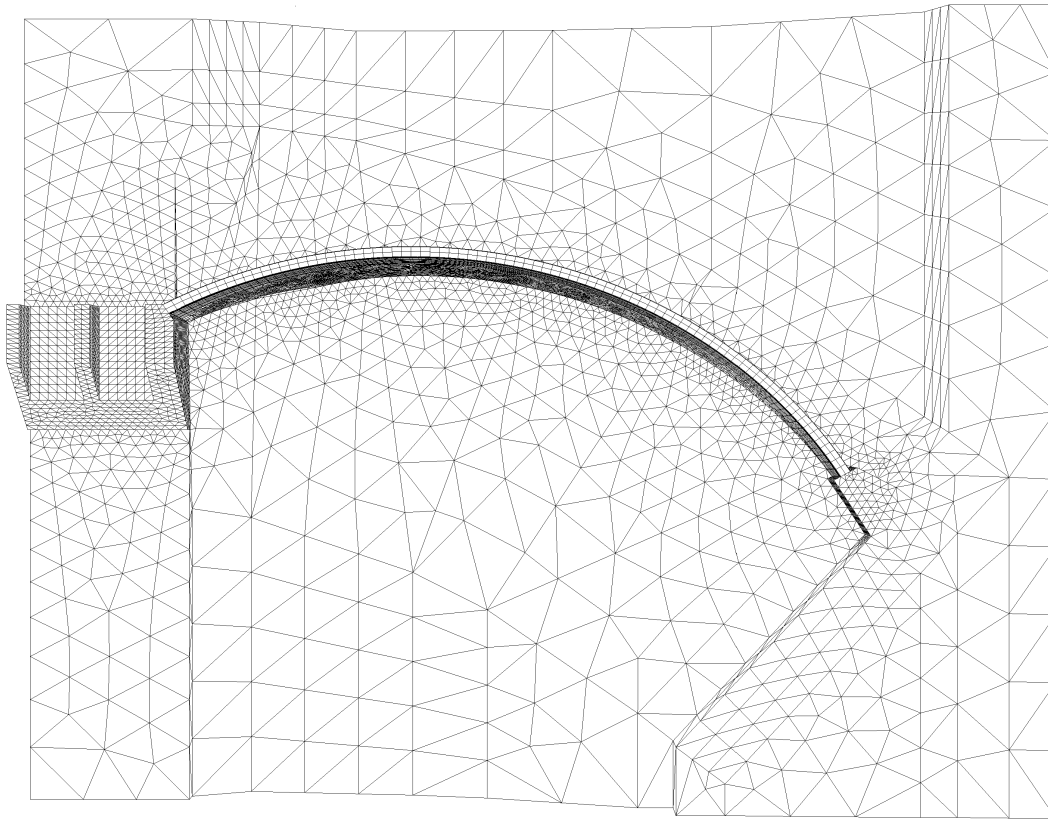
Figure 6.9: Mesh used in the linear mechanical analysis as seen from above.

Table 6.1: Element lengths and types in the linear analysis.

Parts	Element type[*]	Element length [m]	Elements
Dam body	C3D8R	2	4047
Reinforcement	M3D4R	2	3095
Rock, spillway & support	C3D10	2 - 20	42002
Total			49171

[*]As referred to in Abaqus.

6.3 Non-linear mechanical analyses

In the non-linear analyses, considerations were taken to non-linear material behaviour such as cracking of the concrete and yielding in the reinforcement. The purpose of the non-linear analyses were to calculate the extent of cracking, *i.e.* the crack pattern in the dam body, and displacement which was compared with the calculated displacements in the linear analysis.

6.3.1   Concrete damaged plasticity model

The CDP model require five constitutive parameters to be defined. These parameters are the flow potential eccentricity, ϵ, the angle of dilation, ψ, the ratio of initial bi-axial compressive yield stress to initial uni-axial compressive yield stress, f_{b0}/f_{c0}, the ratio of the second stress invariant on the tensile meridian to compressive meridian at initial yield, K_c, and the viscosity. The values chosen in the analyses are presented in Table 6.2 and corresponds to the recommended values by Abaqus [8] since experimental data could not be acquired.

Table 6.2: Values of the constitutive parameters used in the CDP model.

Constitutive parameters in CDP model				
ϵ	ψ	f_{b0}/f_{c0}	K_c	Viscosity
0.1	$35°^{*}$	1.16	0.67	0

*Abaqus recommend a value for the angle of dilation between 30° - 40°.

The damage parameters for compression, d_c, and tension, d_t, were both set to 0 for most of the analyses. A case where the tensile damage parameter, d_t, was implemented is presented in Section 6.3.8.

6.3.2   Non-linear modelling of concrete

In addition to the defined parameters presented in Section 6.2.1, non-linear material compression and tension curves were defined for the concrete. The non-linear behaviour for compression was modelled according to Eurocode 2 [33], with a hardening rule, illustrated in Figure 6.10a. The tensile behaviour used a model based on bi-linear tension softening, illustrated in Figure 6.10b. The theory behind the chosen models are described in Section 4.2.1. The corresponding input values are presented in Table 6.3.

(a) Compressive response curve.   (b) Tensile stress-displacement curve.
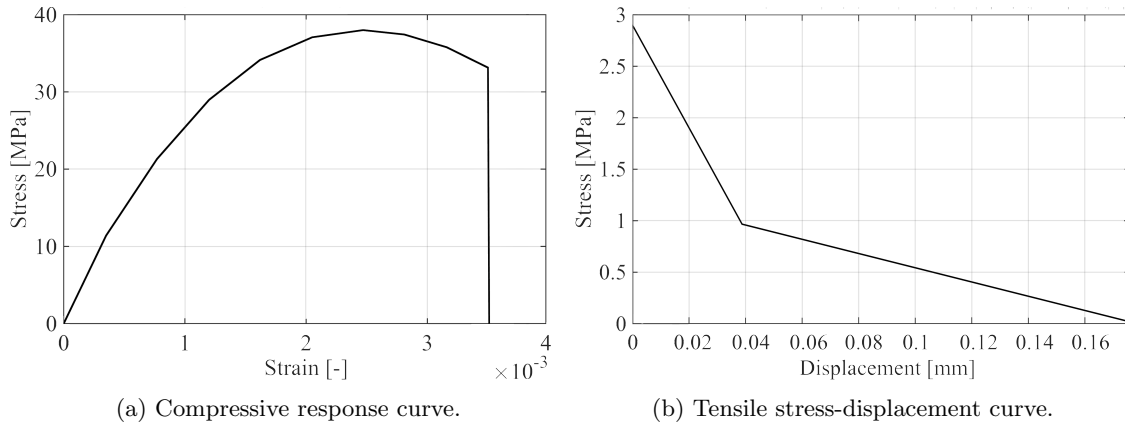
Figure 6.10: Response curves for uni-axial loading used in the CDP model.

Table 6.3: Values used for modelling the compression and tension response curves.

(a) Compressive values.

Stress [MPa]	Strain (‰) [-]
0.0	0.0
11.40	0.35
21.32	0.77
28.98	1.20
34.14	1.62
37.07	2.05
38.00	2.47
37.43	2.81
35.78	3.16
33.14	3.50
0.0	3.51

(b) Tensile values.

Stress [MPa]	Displacement [mm]
2.9	0.0
0.9667	0.039
0.145	0.174

The last value on the tensile stress-displacement curve was set to 5 % of the ultimate tensile strength, and not zero, in order to get a stable solution.

6.3.3   Non-linear modelling of reinforcement

The non-linear stress-strain curve of the reinforcement was modelled as a bi-linear stress-strain curve. The values were interpolated linearly between 0 and the yield strength, f_y, and between f_y and the ultimate stress, f_u. After f_u, a possible rupture is described by setting the stress to zero when the ultimate strain, ε_u, is exceeded by a small number. The values for f_y and f_u and ε_u, are given in Table 5.1. The stress-strain curve is illustrated in Figure 6.11.
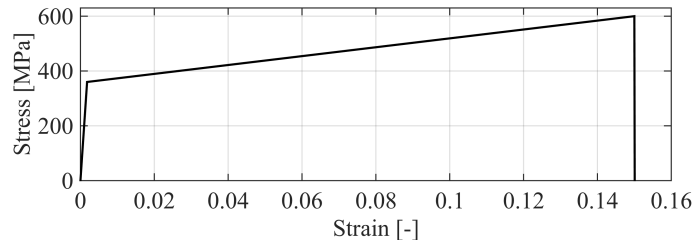
Figure 6.11: Approximated stress-strain curve for reinforcement KS 40.

6.3.4   Interactions and boundary conditions

Interactions and boundary conditions were not changed from the linear mechanical analysis presented in Section 6.2.2.

6.3.5   Combination of thermal data

Due to non-linear analysis being history dependent, different combinations of thermal data were used in order to study how it would influence the results. Two different combinations of thermal data were used with the values provided in Table 5.2.

The first combination starts with a cold year followed by a warm year, henceforth referred to as the *CW temperature combination*. The cold year starts in September as it is fairly close to the reference temperature, T_{ref}. A transition period of one month was added in order to go from T_{ref} to the temperature of September. After the end of the cold year a transition period of four months was added before the start of the warm year. The warm year started in November since the temperature was fairly close to August of the cold year. The transition periods were used to avoid large spikes in the change of temperature. The combination is illustrated in Figure 6.12.

The second combination was a warm year followed by a cold year, henceforth referred to as the *WC temperature combination*. The same approach was implemented as for the combination of a cold year followed by a warm year. The warm year starts in April and a transition period of four months was modelled between the warm year and the cold year, which starts in June. The combination is illustrated in Figure 6.13.
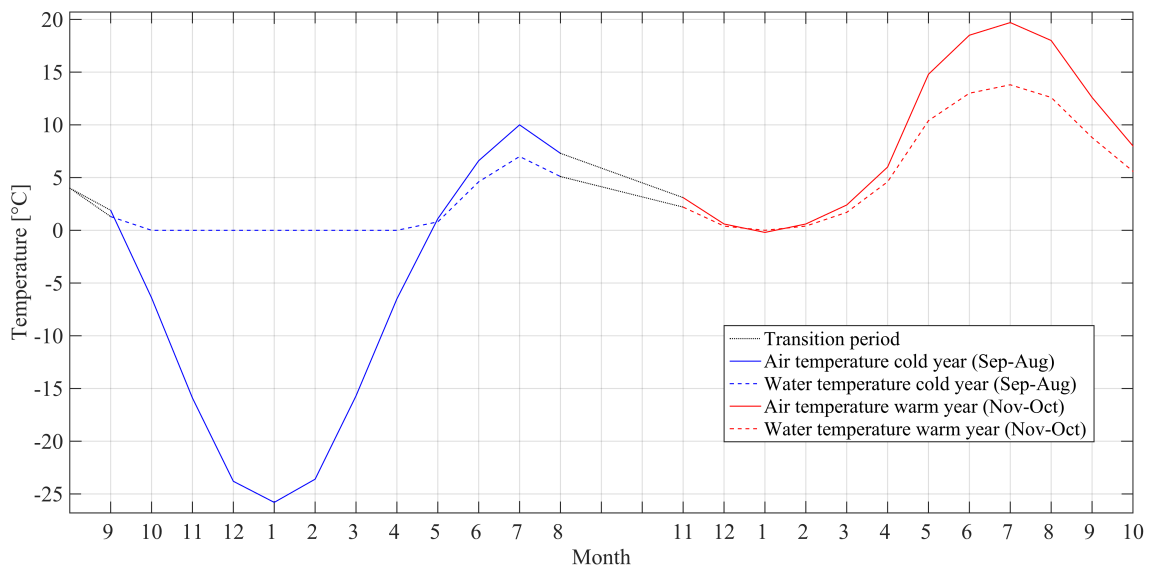
Figure 6.12: Ambient air and water temperatures for a cold year followed by a warm year.
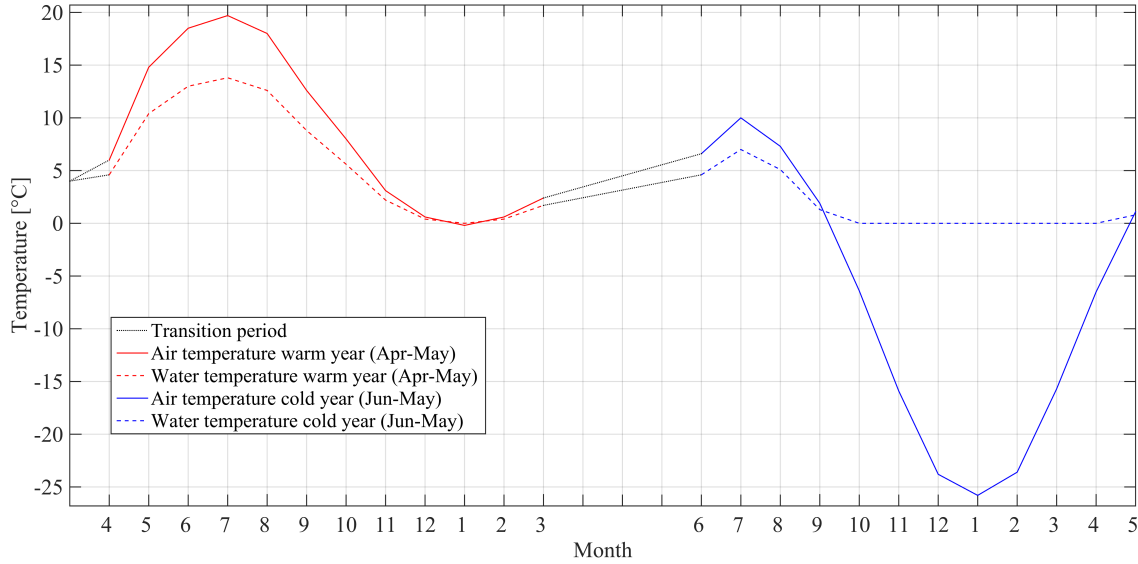
Figure 6.13: Ambient air and water temperatures for a warm year followed by a cold year.

6.3.6   Applying loads

The loads were applied with the Abaqus smooth step amplitude curve, described in Section 4.5.2. Both the gravity and hydrostatic pressure were applied over a time period of one second each in their respective step and set to hold over the total duration of the analyses.

6.3.7   Mesh

Non-linear analyses of cracking in concrete requires smaller elements than a corresponding linear analysis. This is partially in order to prevent snap-back behaviour when cracking occurs and all of the stored energy within the element must be absorbed by its surrounding elements. The maximum elements length used in the non-linear analyses was determined according to [20]

$$L_{max} < \frac{E \cdot G_F}{f_t^2} \tag{6.1}$$

where,

E is the elastic modulus.

G_F is the fracture energy.

f_t is the tensile strength.

With a concrete grade of C30/37, an elastic modulus of 33 GPa, a tensile strength of 2.9 MPa and fracture energy equal to 140 Nm/m^2, the required element length should be less than 0.5 m in areas of interest, *i.e.* spillway, dam body and support.

The mesh used in the non-linear mechanical analyses is presented in Figure 6.14 and in Figure 6.15. Detailed information on the type, size and quantity of the different parts are presented in Table 6.4. The reinforcement was embedded in the dam body with the same technique as for the linear mechanical analysis described in Section 6.2.5.
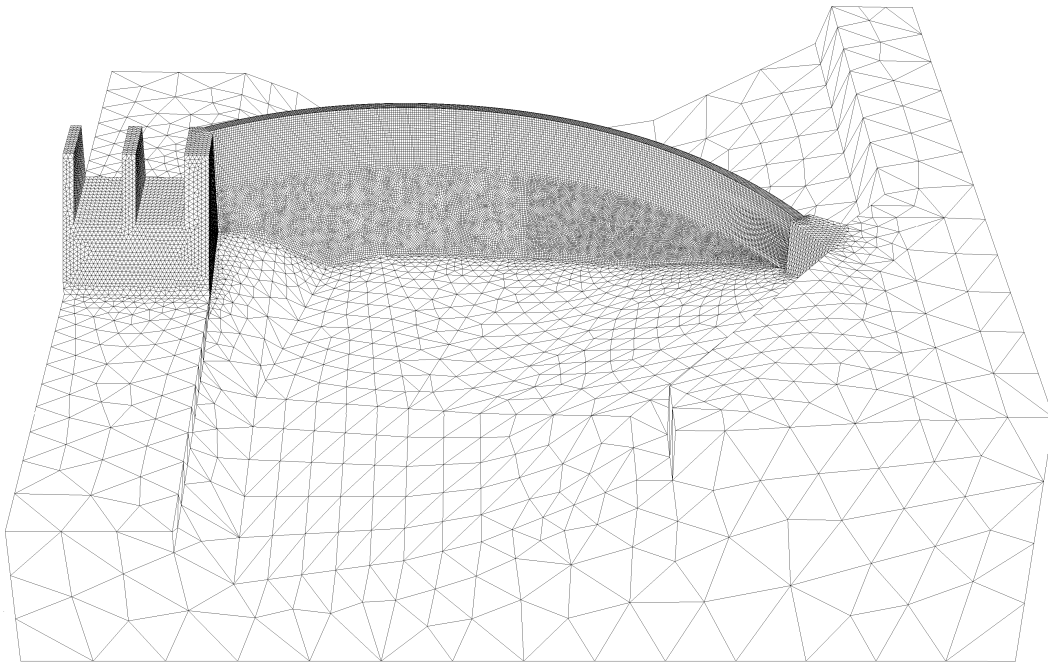
Figure 6.14: Mesh used in the non-linear mechanical analysis.
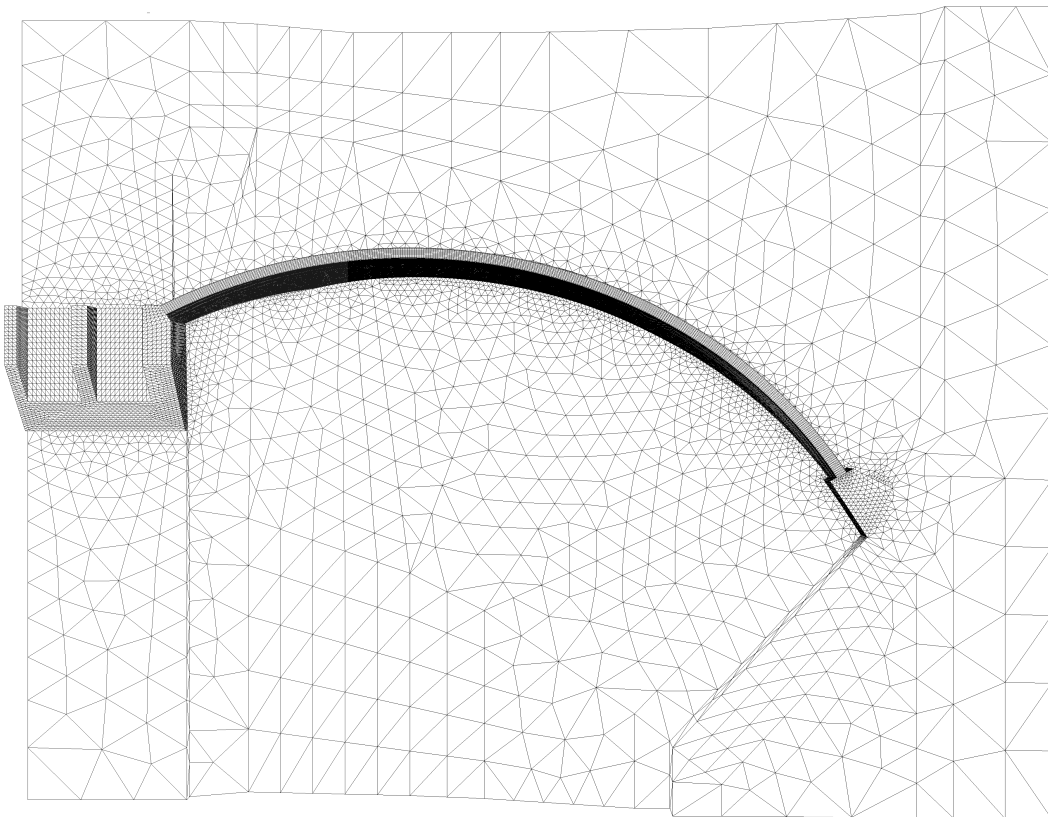
Figure 6.15: Mesh used in the non-linear mechanical analysis as seen from above.

Table 6.4: Element lengths and types in the non-linear analyses.

Parts	Element type[*]	Element length [m]	Elements
Dam body	C3D8R	0.5	222507
Reinforcement	M3D4R	0.5	49082
Rock, spillway & support	C3D10	0.5 - 16	113976
Total			385565

[*]As referred to in Abaqus.

6.3.8 Implementing the tensile damage parameter, d_t, in the CDP model

An analysis with the damage tensile parameter, d_t, implemented in the CDP model was performed in order to see how this would influence the displacement and crack propagation in the dam. The values of d_t were chosen according to a study by Eriksson and Gasch [10] which indicated that a damage parameter value of 0.95 fits quite well with experimental data. The damage parameter was modelled in Abaqus according to Table 6.5. The WC temperature combination was used in the analysis.

Table 6.5: Defined values for the tensile damage parameter, d_t.

Damage parameter [-]	Displacement [mm]
0.0	0.0
0.95	1.744×10^{-4}

Chapter 7

Results

In this chapter, the results from the numerical analyses are presented. Temperature distributions and temperature gradients are calculated in order to study the effects seasonal temperature variation have on the structure. Radial and vertical displacements plots are presented in order to study the differences in result for different temperature combinations and different material modelling. Calculated cracks propagation from the non-linear analyses are compared with the linear result in order to study possible concordence concerning areas in risk of cracking and crack patterns.

7.1   Thermal analysis

The temperature variation over time was measured in four nodes located in the centre section, 82.6 m from the spillway, for a cold year followed by a warm year. The nodes are illustrated in Figure 7.1. Node (a), (b) and (c) are located 10 meter above the foundation on a straight line in an area where the temperature fluctuations would not be influenced by the rock foundation or the non-insulated top surface. Node (d) is located on top of the dam, which was not insulated, in order to study the effect of the insulation on the temperature distribution in the dam. The purpose of the plot was to visualise how the temperature fluctuates in different sections of the dam during the analyses.
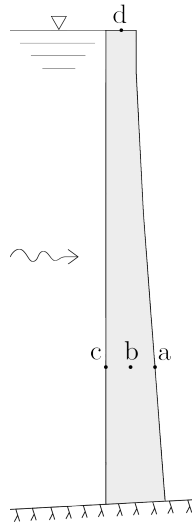
Figure 7.1: Nodes used to measure the temperature variation in the dam body over time.
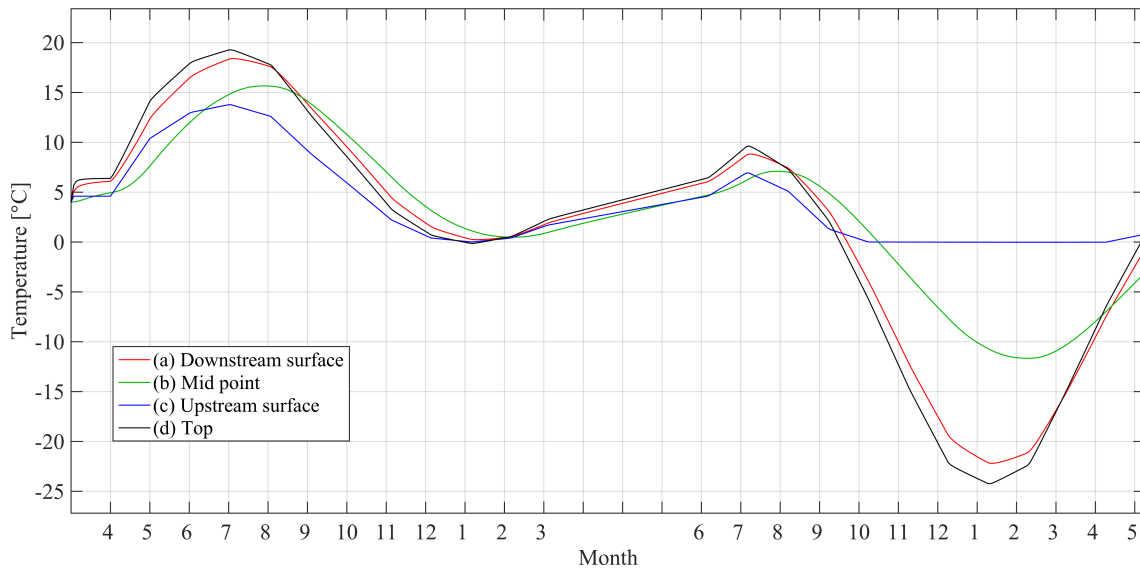
Figure 7.2: Temperature variation at the four nodes for a warm year followed by a cold year.

Figure 7.2 illustrates how the insulated wall reduces the temperature peaks and delays the heating and cooling of the downstream surface by approximately 3 °C at most. The temperature difference between the downstream and upstream surfaces was approximately 5 °C in July the warm year and and 22 °C in January the cold year. The absolute value of the gradient in the dam is plotted over time in Figure 7.3 in order to illustrate how the temperature gradient varies over time. This can give an indication of when large displacements and possibly crack propagation will occur in the dam.
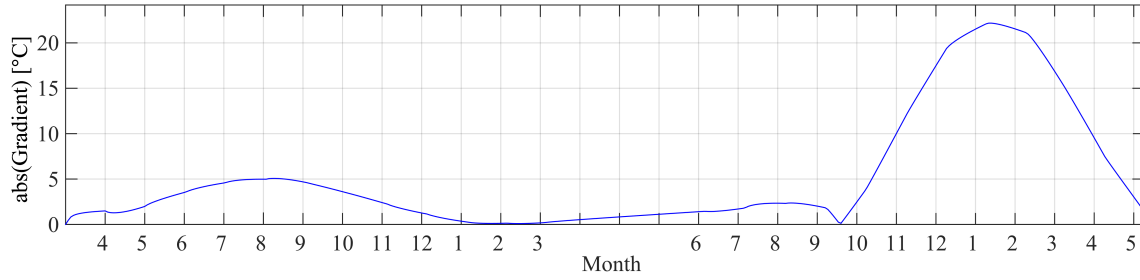
Figure 7.3: The absolute value of the temperature gradient between the upstream and downstream surfaces of the dam for the warm year followed by a cold year.

The temperature distribution in the centre section of the dam body, marked A-A in Figure 7.4, for the warmest and coldest months are presented in Figure 7.5.
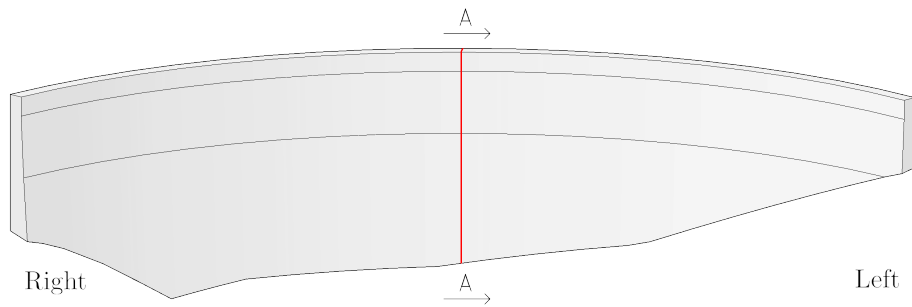
Figure 7.4: Centre section, A-A, of the dam body marked with a red line. The centre section is located 82.6 m from the spillway.
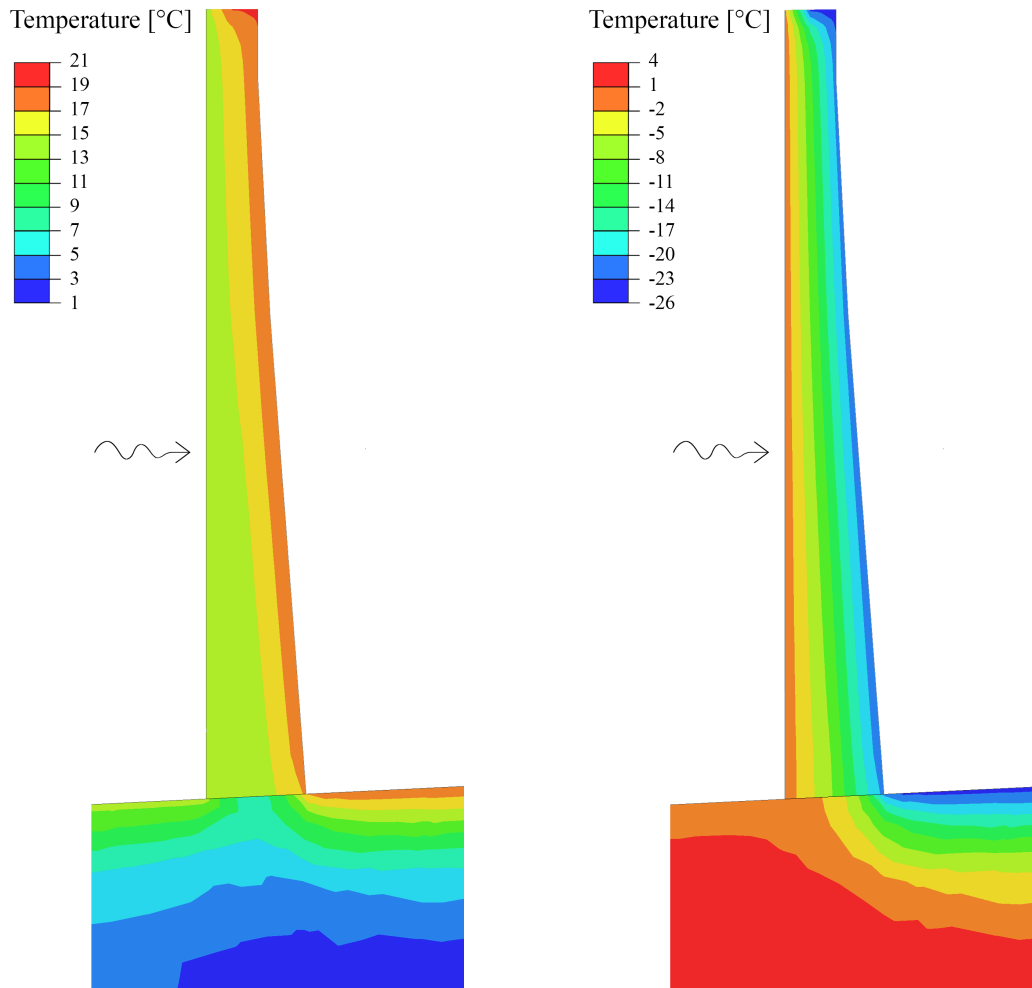
(a) Temperature distribution in July a warm year.   (b) Temperature distribution in January a cold year.

Figure 7.5: Section A-A: Temperature distribution in the centre section of the dam at the warmest and coldest month.

7.2 Linear mechanical analysis

7.2.1 Deformation

The calculated displacements were measured with a cylindrical coordinate system according to Figure 7.6. The x-axis begins at the intersect between the spillway (right) and the dam body and follows the arch to the support (left).
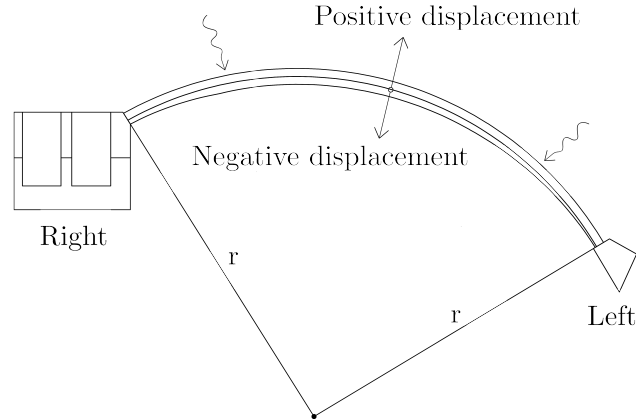
Figure 7.6: Cylindrical coordinate system.

The calculated radial displacement was measured along three lines, illustrated in Figure 7.7, for a warm and for a cold year.
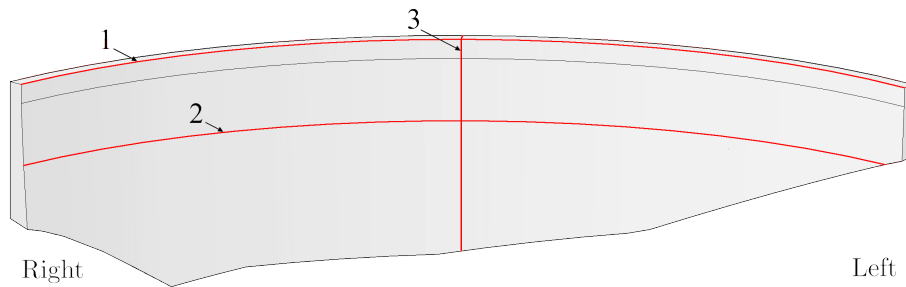
Figure 7.7: Three lines, highlighted in red, on the downstream surface used to extract the calculated radial displacements of the dam. (1) At the crest. (2) A line 14 meter below the crest. (3) A vertical line in the centre section on the downstream surface.

The calculated radial displacement of the crest is presented in Figure 7.8 and the calculated radial displacement 14 meter below the crest is presented in Figure 7.9. The largest calculated radial displacement of the crest in the upstream, positive, direction occurred in July of a warm year. The largest calculated radial displacement of the crest in the downstream, negative, direction occurred in January of a cold year. The deformation caused by gravity and hydrostatic forces, referred to in Figure 7.8 - 7.10 as *Initial conditions*, are plotted as a dotted line. The squiggly arrow in the figures indicates the water flow direction.
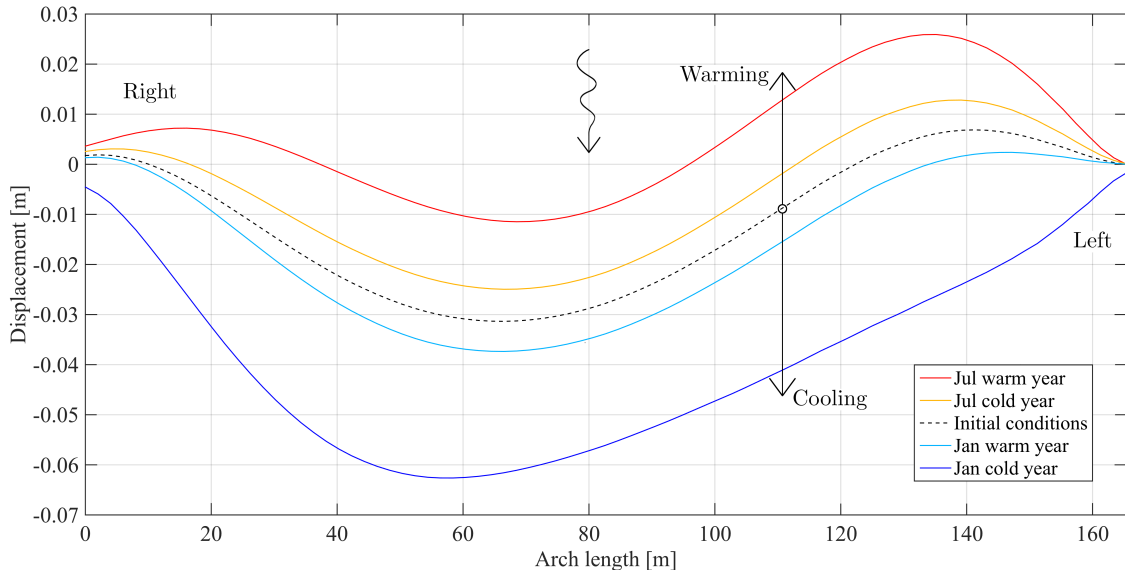
Figure 7.8: Maximum calculated radial displacement of the crest line.
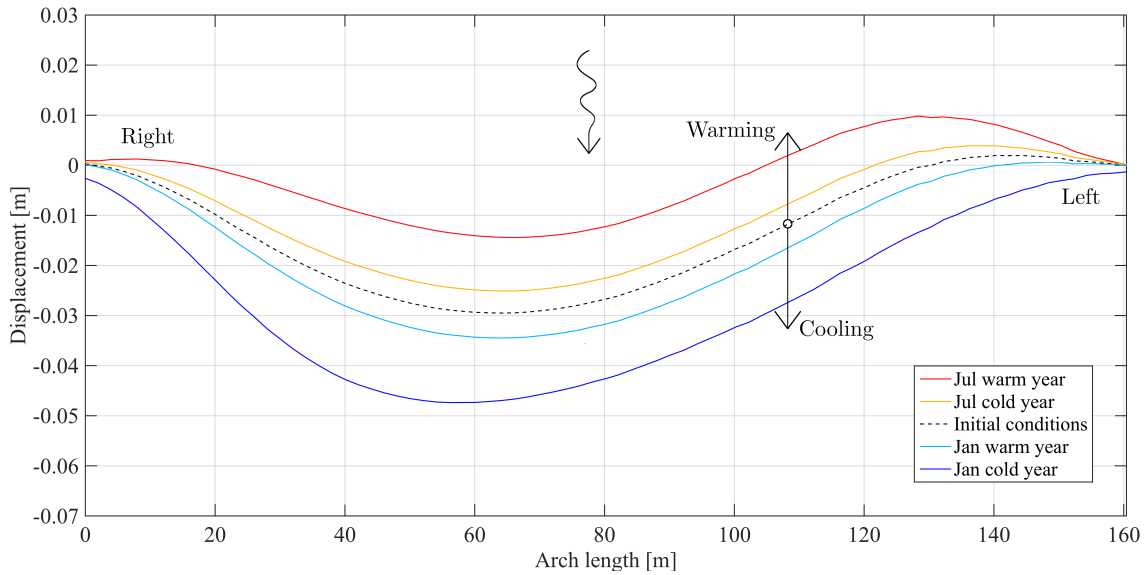
Figure 7.9: Maximum calculated radial displacement of a line 14 m below the crest.

The radial displacement of the centre section was measured as a function of height and is presented in Figure 7.10. The largest calculated displacement in the upstream direction, referred to as *Minimum* in Figure 7.10, occurred in July of a warm year. The largest displacement in the downstream direction, referred to as *Maximum* in Figure 7.10, occurred in January of a cold year.
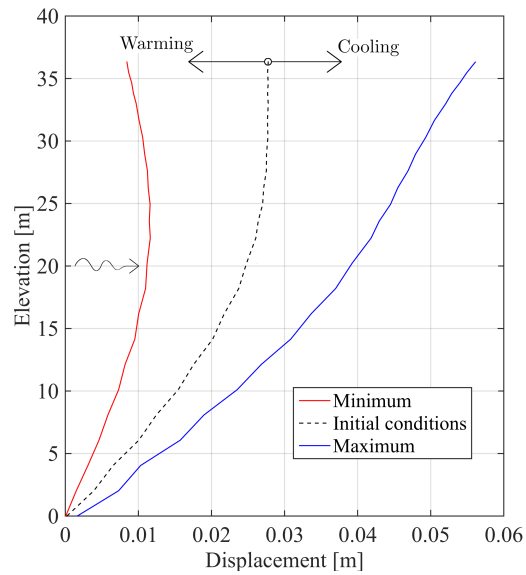
Figure 7.10: Maximum calculated radial displacement of the centre section of the dam as a function of height.

Radial displacement contour plots are presented in Figure 7.11 and Figure 7.12 at the time of the largest positive and negative radial displacement respectively.
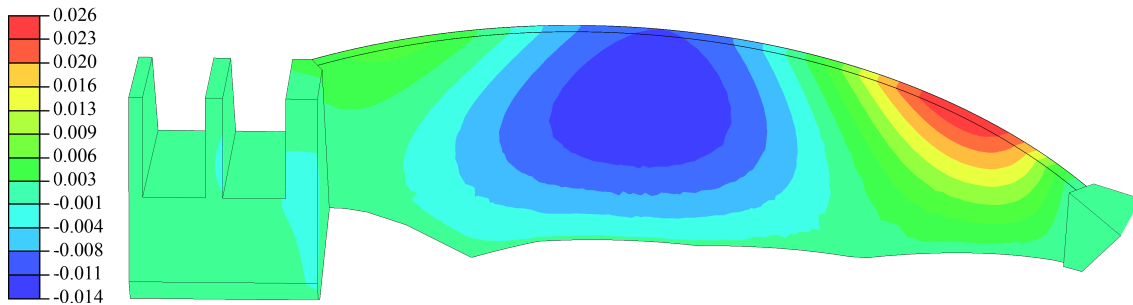
Figure 7.11: Contour displacement plot at the time of the largest positive radial displacement, [m], of the dam in July of a warm year.
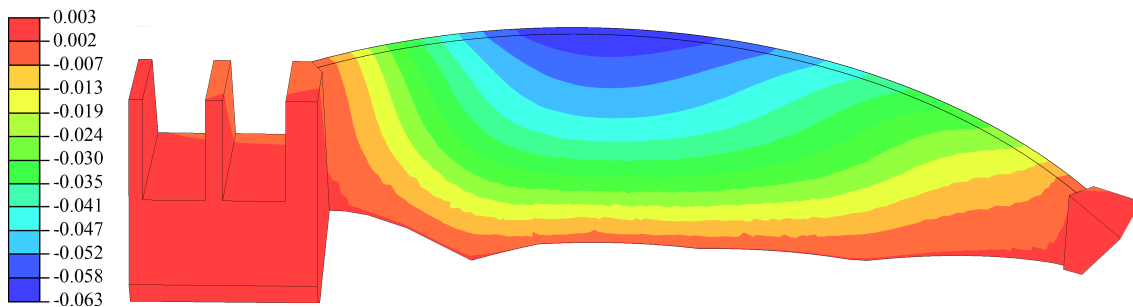
Figure 7.12: Contour displacement plot at the time of the largest negative radial displacement, [m], of the dam in January of a cold year.

7.2.2 Stresses

The maximum principal stress occurs on the downstream side of the dam near the base during January of the cold year. In Figure 7.13 - 7.14, red areas illustrate where the tensile strength of the concrete of 2.9 MPa, see Table 5.1, was exceeded and the dam is possibly subjected to cracking. Only areas on the downstream side reached tensile stresses greater than the tensile strength of concrete, *i.e* no areas on the upstream side was marked red at any point in time.
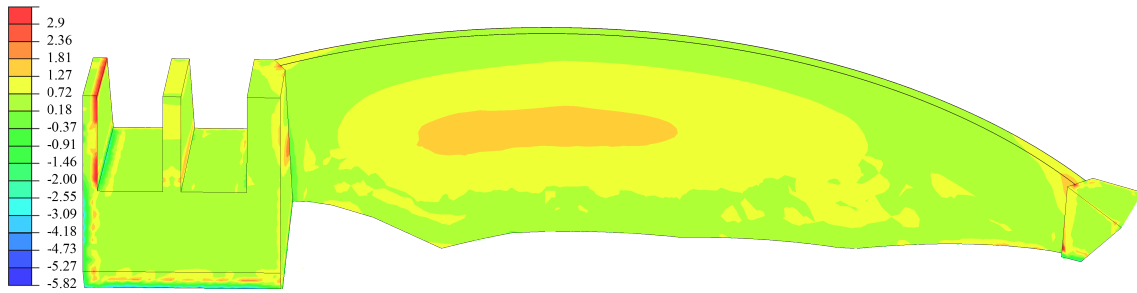
Figure 7.13: Maximum principal stress, [MPa], in July of a warm year. Areas in orange may exceed the tensile strength of concrete and are perhaps subjected to minor cracking.
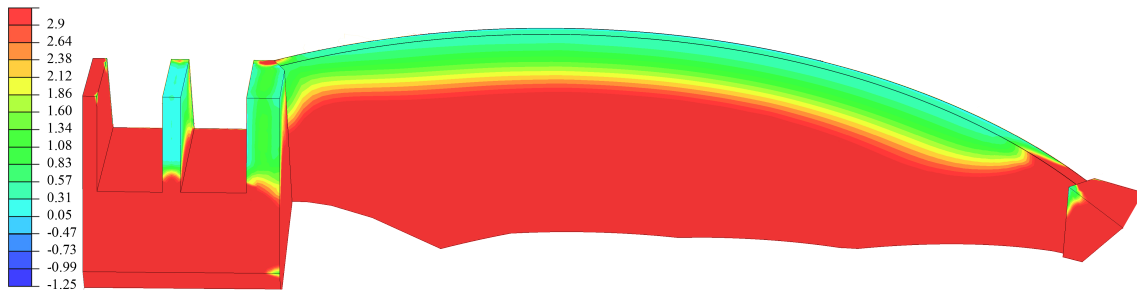
Figure 7.14: Maximum principal stress, [MPa], in January of a cold year. Areas in red most probably exceed the tensile strength of concrete and are possibly subjected to extensive cracking

The number of elements in the dam body which exceed the tensile strength of the concrete in the maximum principal stress direction is plotted over time with the temperature history in the middle of the dam, node (b) in Figure 7.1, for a cold year in Figure 7.15. The aim of the figure is to study the influence the average temperature has on the crack propagation and provide an indication of when cracks start to propagate in the dam body.
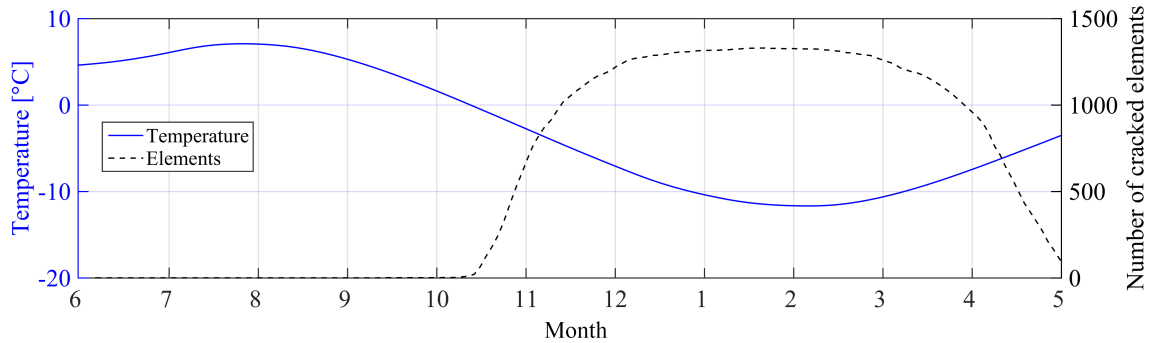
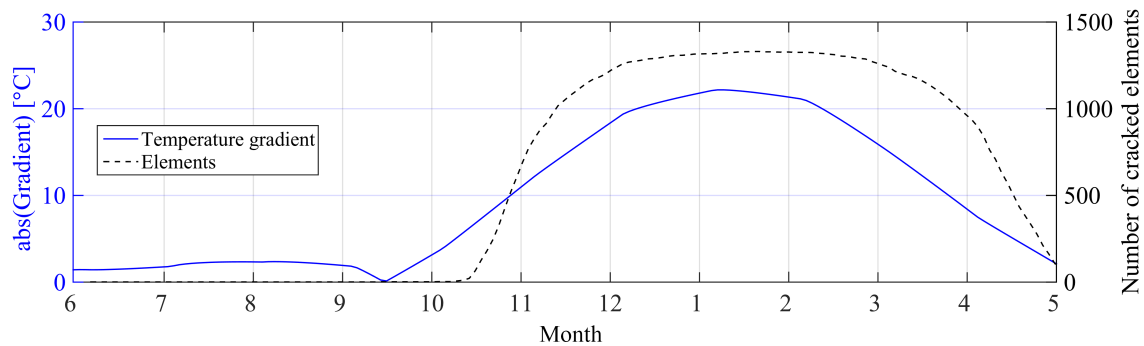Figure 7.15: The temperature in the middle of the dam body, node (b) in Figure 7.1, as well as the number of elements which exceeded the tensile strength of the concrete plotted over time for a cold year.

The number of elements in the dam body which exceed the tensile strength of the concrete in the maximum principal stress direction is plotted over time with the temperature gradient in Figure 7.16 for a cold year. The aim of the figure is to study the influence of the temperature gradient has on the cracks propagation and provide an indication of when cracks start to propagate in the dam body.

Figure 7.16: The absolute values of the temperature gradient in the dam body as well as the number of elements which exceeded the tensile strength of the concrete plotted over time for a cold year.

7.2.3 Stress direction

A vector direction plot of the maximum and minimum principal stress in the dam body are presented in Figure 7.17 - 7.18 for July a warm year and in Figure 7.19 - 7.20 for January a cold year. The direction of the arrows represent the global direction of the minimum or maximum principal stress and the relative length and colour indicate the magnitude of the value in the nodes. The figures provide an idea of what the crack pattern might look like. The crack surfaces develops along the minimum principal stress direction and perpendicular to the maximum principal stress direction [2].
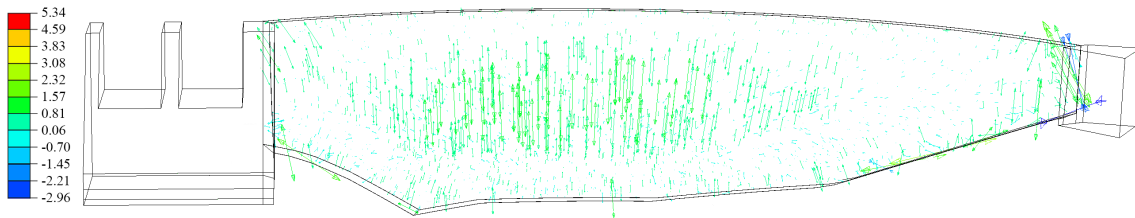
Figure 7.17: Maximum principal stress direction in the dam body in July of a warm year, [MPa].
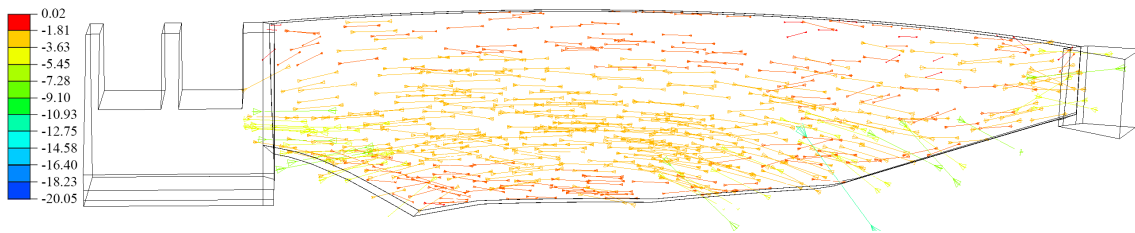

Figure 7.18: Minimum principal stress direction in the dam body in July of a warm year, [MPa].
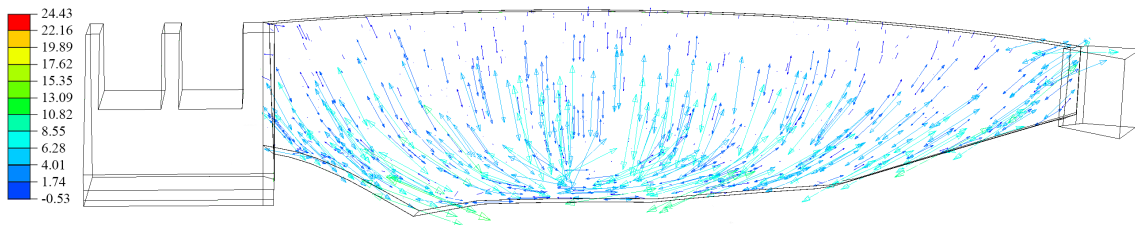

Figure 7.19: Maximum principal stress direction in the dam body in January of a cold year, [MPa].
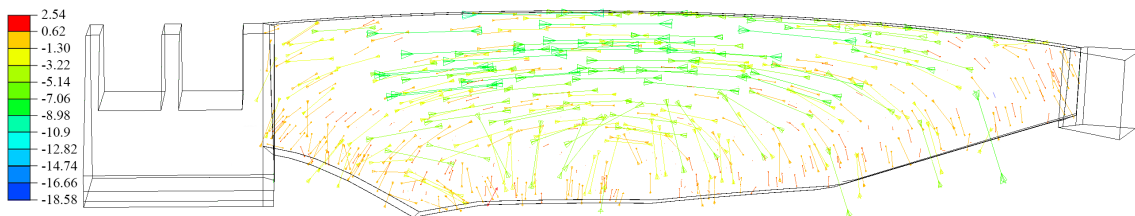

Figure 7.20: Minimum principal stress direction in the dam body in January of a cold year, [MPa].

7.3   Non-linear mechanical analyses

7.3.1   Quasi-static control

The strain energy and kinematic energy for the whole model, during the total time of the non-linear analysis, were extracted from Abaqus. The values were compared in order to ensure that a quasi-static analysis was performed according to Section 4.5.4.

Warm year followed by cold year temperature combination

Figure 7.21 presents the resulting strain and kinematic energy on a global scale throughout the whole analysis for the WC temperature combination. The maximum ratio between the strain and kinematic energy is approximately 2.5 % indicating small kinematic effects and a quasi-static behaviour. At some points between 0 and 2 seconds the ratio between the kinematic energy and the strain energy exceeds the recommended value, however, since this occurred during the gravity and hydrostatic step and the strain energy develops at a slower rate, this is neglected.
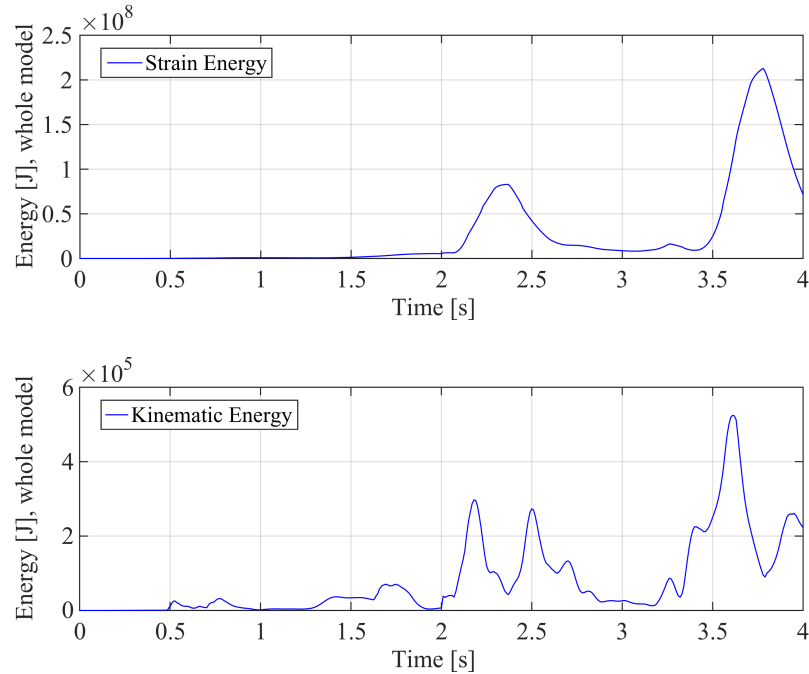

Figure 7.21: Strain energy and kinematic energy for the whole model for a warm year followed by a cold.

Cold year followed by warm year temperature combination

Figure 7.22 presents the resulting strain and kinematic energy on a global scale throughout the whole analysis for the CW temperature combination. The maximum ratio between the strain and kinematic energy is approximately 1.4 % indicating small kinematic effects and a quasi-static behaviour. The same reasoning is applied here as for the WC temperature combination relating the ratio between the kinematic energy and stain energy exceeds the recommended value during the first 2 seconds of the analysis.
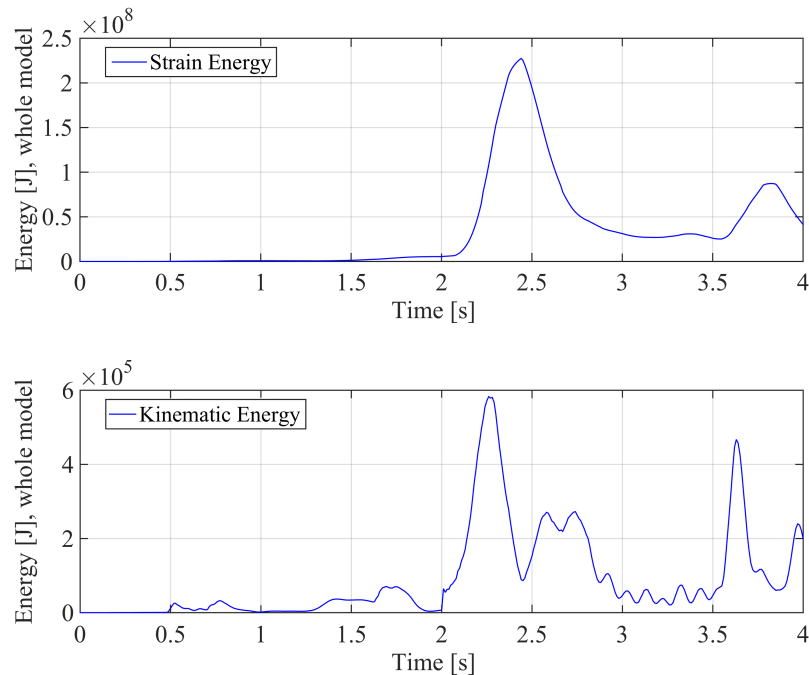
Figure 7.22: Strain energy and kinematic energy for the whole model for a cold year followed by a warm year.

7.3.2 Deformation

The radial displacement of the dam was measured along the same line as in the linear mechanical analysis presented in Figure 7.7, with the same cylindrical coordinate system illustrated in Figure 7.6.

Warm year followed by a cold year temperature combination

The largest calculated displacement of the crest in the upstream, positive, direction occurred in July of the warm year. The largest calculated displacement of the crest in the downstream, negative, direction occurred in January of the cold year. The calculated radial displacement of the crest is illustrated in Figure 7.23 and the calculated displacement 14 meter below the crest is illustrated in Figure 7.24. The deformation caused by gravity and hydrostatic forces, refereed to in the displacement figures as *Initial conditions*, are plotted as a dotted line. The squiggly arrow in the figures indicates the water flow direction.
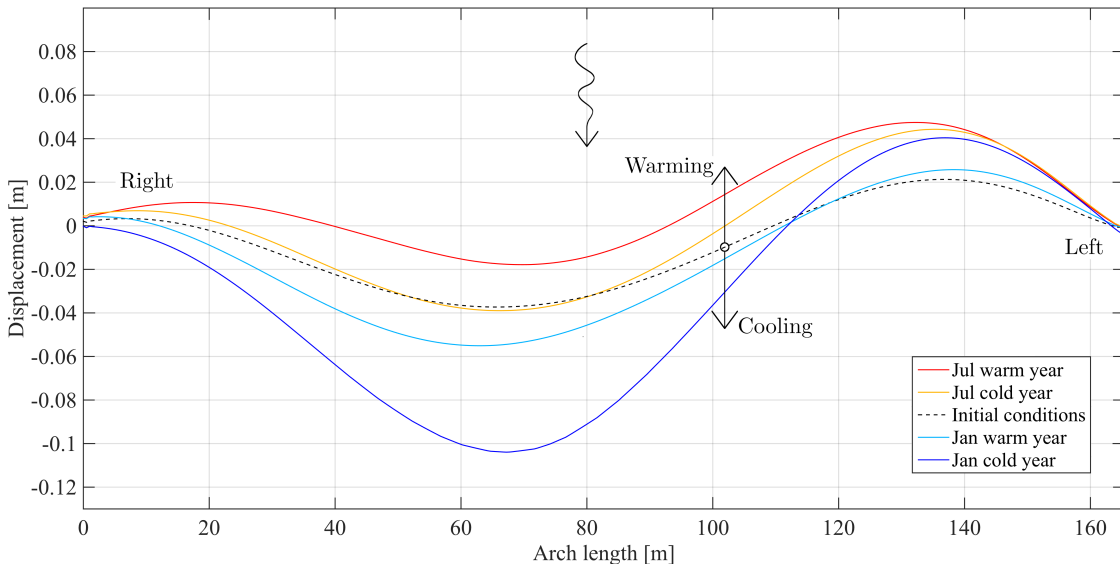
Figure 7.23: Maximum calculated radial displacement of the crest line for a warm year followed by a cold year.
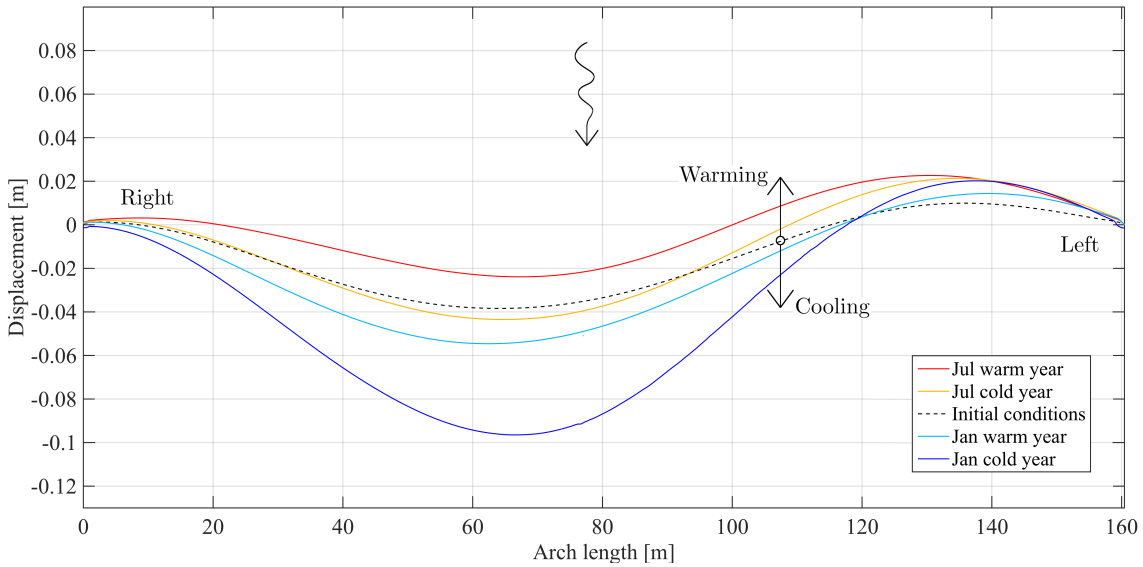

Figure 7.24: Maximum calculated radial displacement of a line 14 m below the crest line on the downstream surface for a warm year followed by a cold year.

The radial displacement of the centre section was measured as a function of height and is presented in Figure 7.25. The largest calculated displacement in the upstream direction, referred to as *Minimum* in Figure 7.25, occurred in July of a warm year. The largest displacement in the downstream direction, referred to as *Maximum* in Figure 7.25, occurred in January of a cold year.
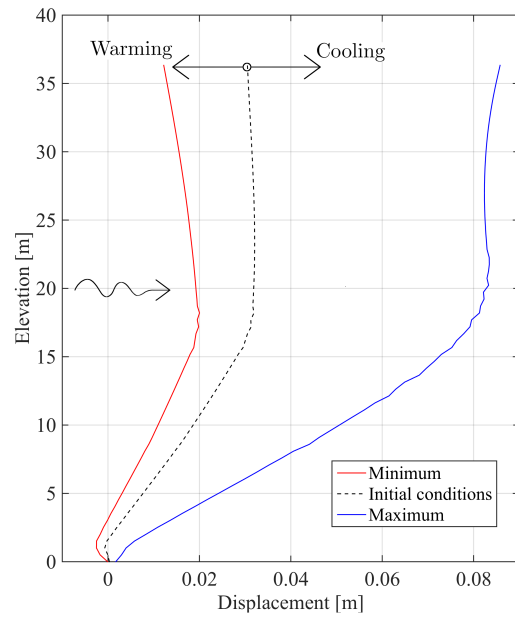
Figure 7.25: Maximum radial calculated displacement at the time of the centre section of the dam as a function of height.

Displacement contour plots, for the WC temperature combination, are presented in Figure 7.26 and in Figure 7.27 at the time of the largest positive and largest negative radial displacement respectively.
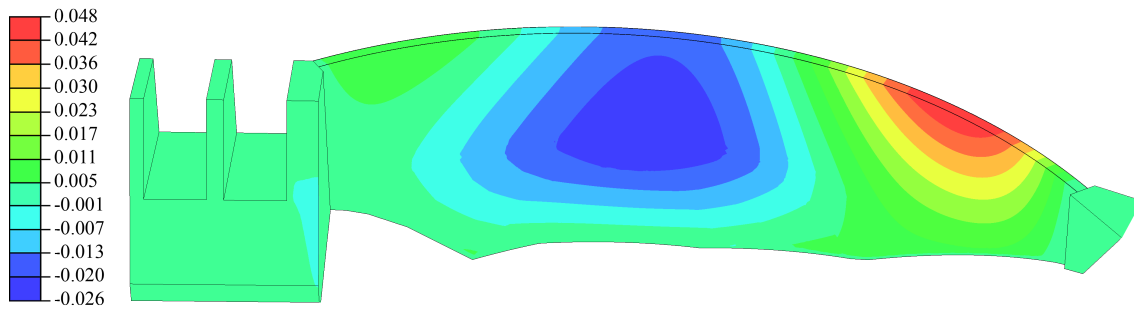

Figure 7.26: Contour displacement plot at the time of the largest positive radial displacement, [m], of the dam during July the first year.
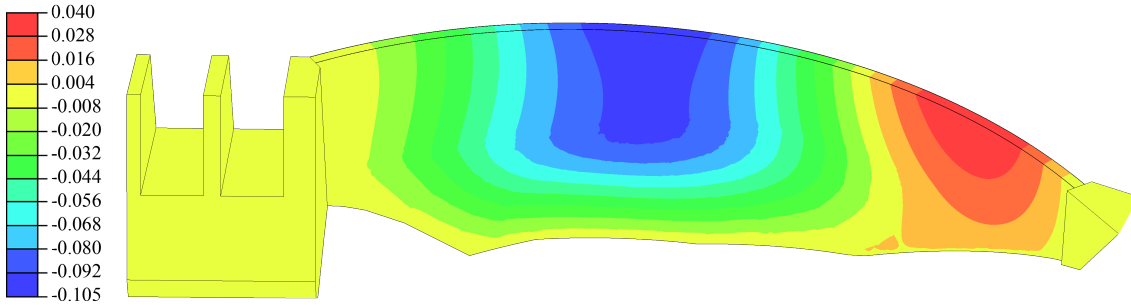
Figure 7.27: Contour displacement plot at the time of the largest negative radial displacement, [m], of the dam during January the second year.

Cold year followed by a warm year temperature combination

The largest calculated displacement of the crest in the upstream, positive, direction occurred in July of the warm year. The largest calculated displacement of the crest in the downstream, negative, direction occurred in January of the cold year. The calculated radial displacement of the crest is illustrated in Figure 7.28 and the calculated displacement 14 meter below the crest is illustrated in Figure 7.29. The deformation caused by gravity and hydrostatic forces, refereed to in the displacement figures as *Initial conditions*, are plotted as a dotted line. The squiggly arrow in the figures indicates the water flow direction.
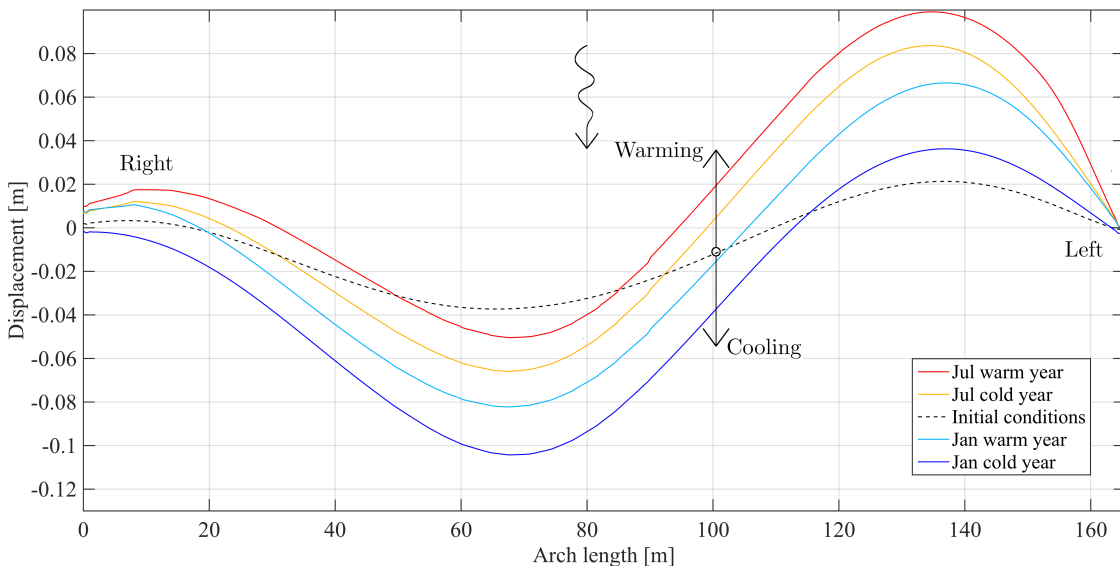

Figure 7.28: Maximum calculated radial displacement of the crest line for a cold year followed by a warm year.
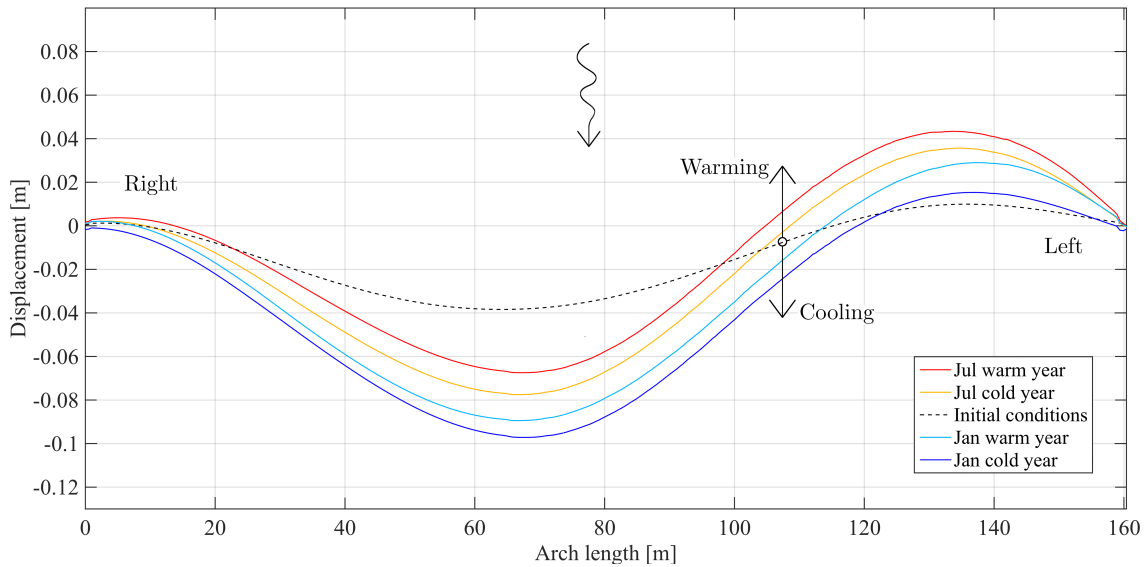
Figure 7.29: Maximum calculated radial displacement of a line 14 m below the crest line on the downstream surface for a cold year followed by a warm year.

The radial displacement of the centre section was measured as a function of height and is presented in Figure 7.30. The largest calculated displacement in the upstream direction, referred to as *Minimum* in Figure 7.30, occurred in July of a warm year. The largest displacement in the downstream direction, referred to as *Maximum* in Figure 7.30, occurred in January of a cold year.
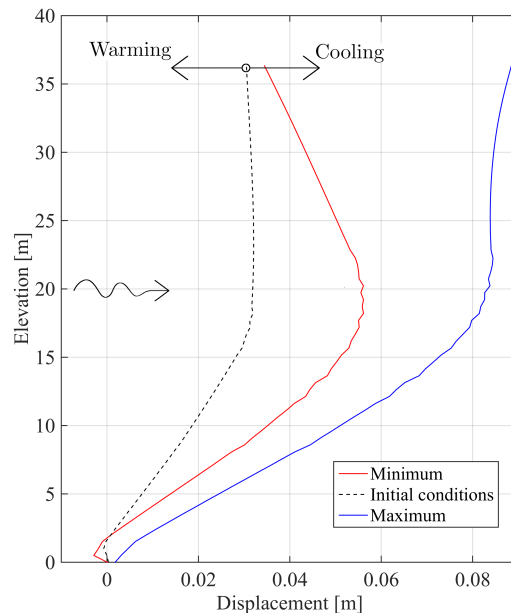

Figure 7.30: Maximum calculated radial displacement of the centre section of the dam as a function of height.

Displacement contour plots, for the CW temperature combination, are presented in Figure 7.31 - 7.32 for the largest positive and largest negative radial displacement respectively.
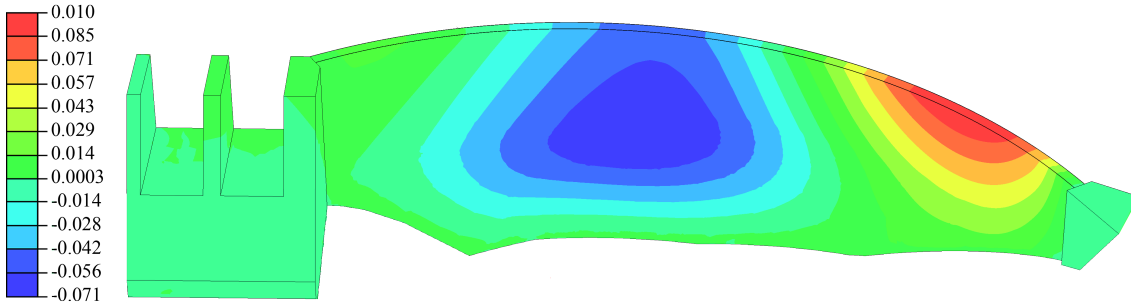
Figure 7.31: Contour displacement plot of the largest positive radial displacement, [m], of the dam during July the second year.
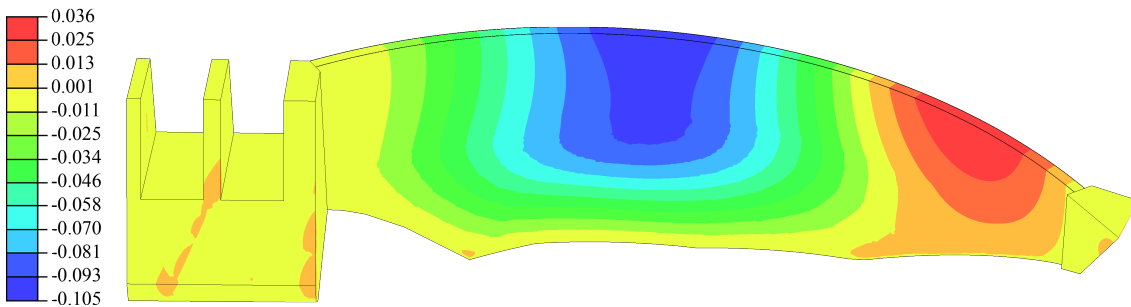

Figure 7.32: Contour displacement plot of the largest negative radial displacement, [m], of the dam during January the first year.

7.3.3   Crack propagation

Crack initiation was assumed to occur when the maximum principal tensile stress exceeded the tensile strength of the concrete. The crack surface develops in the normal direction of the maximum tensile principal stress. As the stress changes from tensile to compressive the cracks are able to close completely, however, the elements are still defined as cracked throughout the analysis. Only elements where the plastic strain in the maximum principal stress direction exceeded 0.001 were plotted. The value 0.001 was chosen in order to only include elements which exceeds the plastic strain by a margin and can with a higher certianty be assumed to have cracked. The elements assumed to have cracked are presented in the figures and tables presented below.

Warm year followed by a cold year

The total number of elements in the dam body that reached a plastic strain of over 0.001 is plotted in Figure 7.33 together with the temperature in the middle of the dam and in 7.34 together with the absolute value of the temperature gradient.
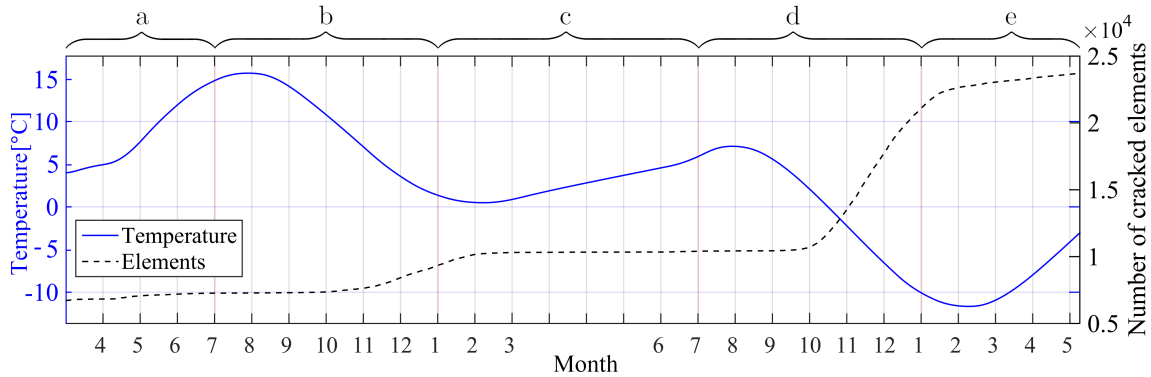
Figure 7.33: The temperature in the middle of the dam body, node (b) in Figure 7.1, as well as the number of elements in the dam body which was assumed to have cracked over time.
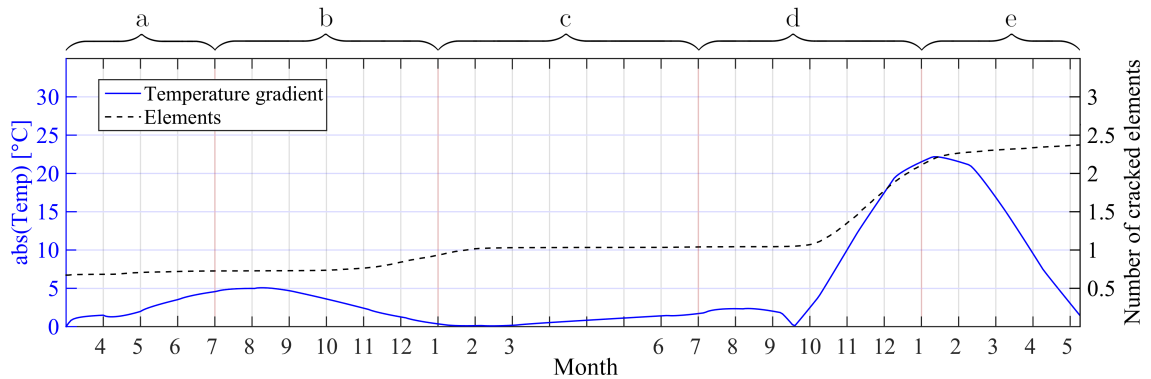

Figure 7.34: The absolute value of the temperature difference between the upstream and downstream surfaces of the dam as well as the number of elements in the dam body which was assumed to have cracked over time.

The number of cracked elements are presented in Table 7.1 for the initial condition, January and July of both years, as well as at the end of the analysis.

Table 7.1: Number of elements that have reached a plastic strain greater than 0.001 in the dam body at the frames presented in Figure 7.35 - 7.39 as well as for the complete analysis.

	Time	Number of elements	% of total elements
	Gravity and hydrostatic pressure	6725	3.0
a	July the first year	7243	3.2
b	January the first year	9852	4.4
c	July the second year	10421	4.7
d	January the second year	22868	10.3
e	Complete analysis	23724	10.7

The plastic strain in the maximum principal stress direction is presented in Figure 7.35 - 7.40 which gives an indication of the crack propagation and patterns in the dam.

Figure 7.35: Crack propagation due to gravity and hydrostatic pressure alone on the downstream surface.

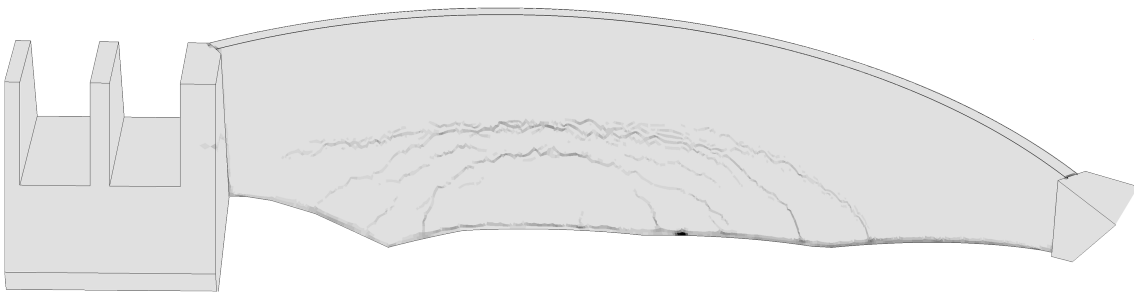Figure 7.36: Crack propagation in July the first year on the downstream surface.

Figure 7.37: Crack propagation in January the first year on the downstream surface.

Figure 7.38: Crack propagations in July the second year on the downstream surface.

Figure 7.39: Crack propagation in January the second year on the downstream surface.

Figure 7.40: Crack propagation in January the second year on the upstream surface.

Cold year followed by a warm year

The total number of elements in the dam body that reached a plastic strain of over 0.001 is plotted in Figure 7.41 together with the temperature in the middle of the dam and in 7.42 together with the absolute value of the temperature gradient.
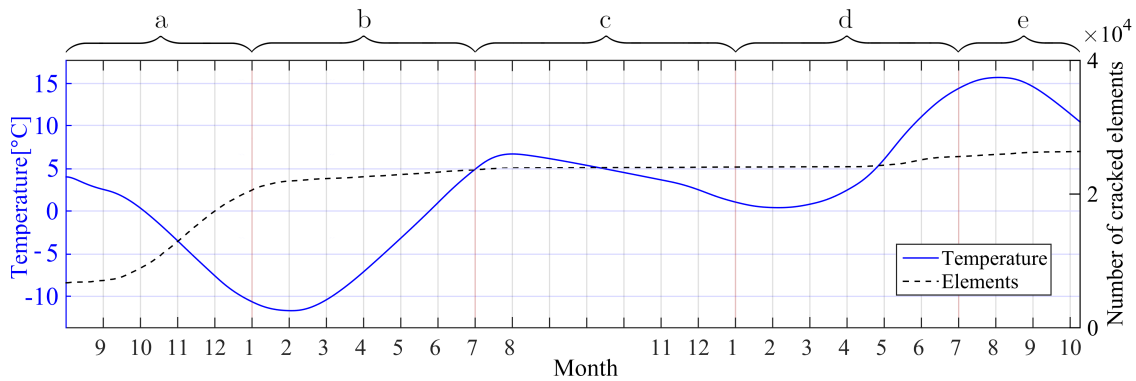
Figure 7.41: The temperature in the middle of the dam body, node (b) in Figure 7.1, as well as the number of elements in the dam body which was assumed to have cracked over time.
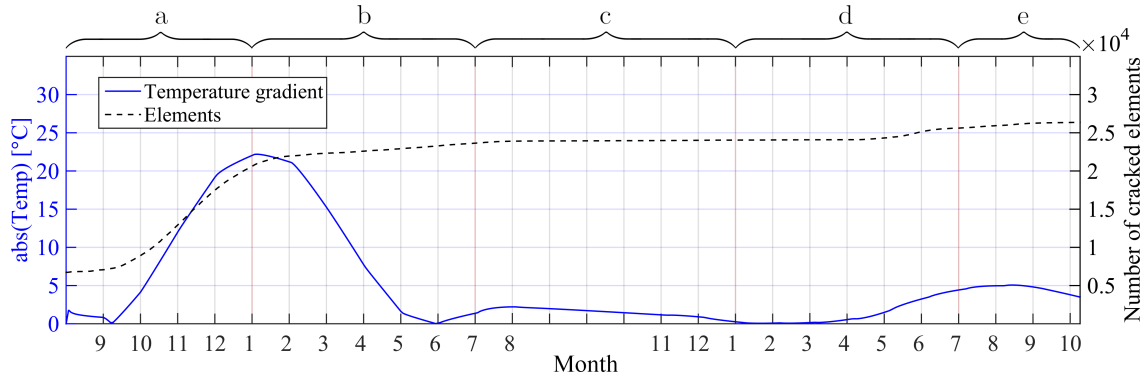
Figure 7.42: The absolute value of the temperature difference between the upstream and downstream surfaces of the dam as well as the number of elements in the dam body which was assumed to have cracked over time.

The number of cracked elements are presented in Table 7.2 for the initial condition, January and July of both years, as well as at the end of the analysis.

Table 7.2: Number of elements that have reached a plastic strain greater than 0.001 in the dam body at the frames presented in Figure 7.43 - 7.47 as well as for the complete analysis.

	Time	Number of elements	% of total elements
	Gravity and hydrostatic pressure	6725	3.0
a	January the first year	21885	9.8
b	July the first year	23876	10.7
c	January the second year	24062	10.8
d	July the second year	25475	11.4
e	Complete analysis	26372	11.9

The plastic strain in the maximum principal stress direction is presented in Figure 7.43 - 7.48 which aims to give an indication of the crack propagation and patterns in the dam.
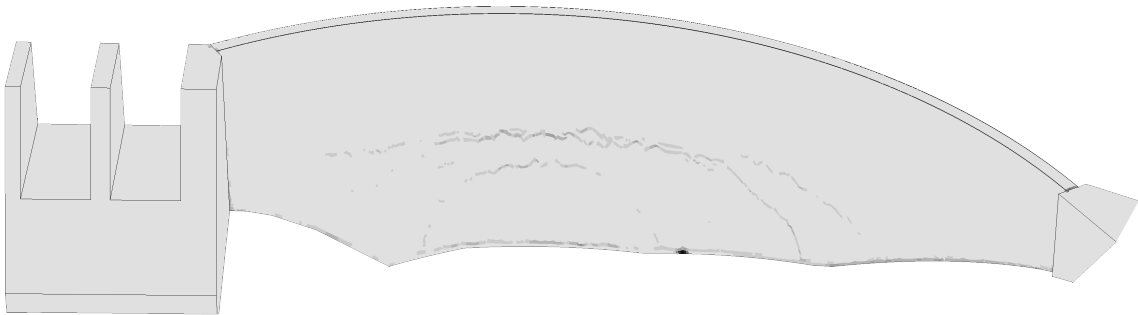
Figure 7.43: Crack propagation due to gravity and hydrostatic pressure alone on the downstream surface.

Figure 7.44: Crack propagation in January the first year on the downstream surface.

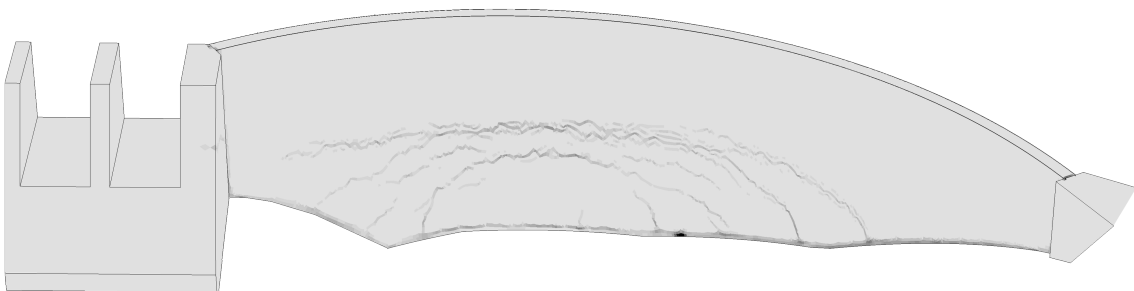Figure 7.45: Crack propagation in July the first year on the downstream surface.

Figure 7.46: Crack propagations in January the second year on the downstream surface.

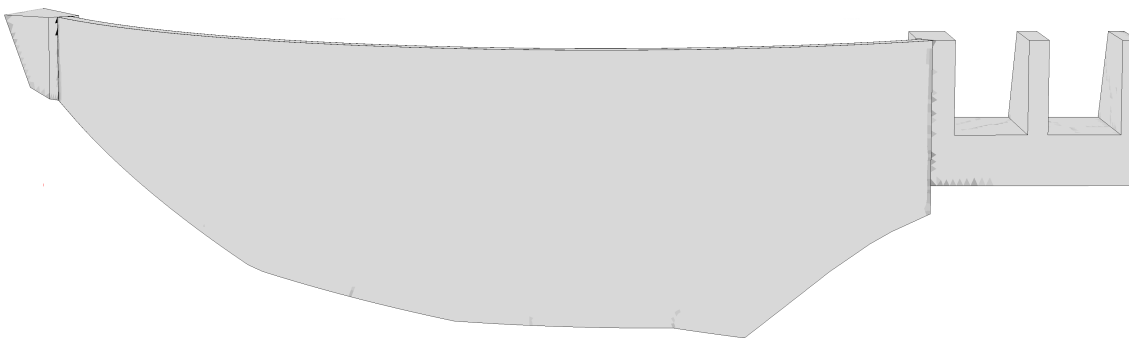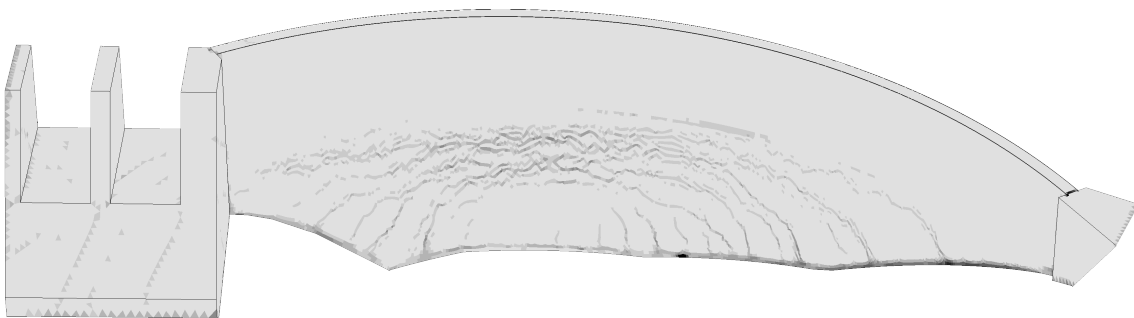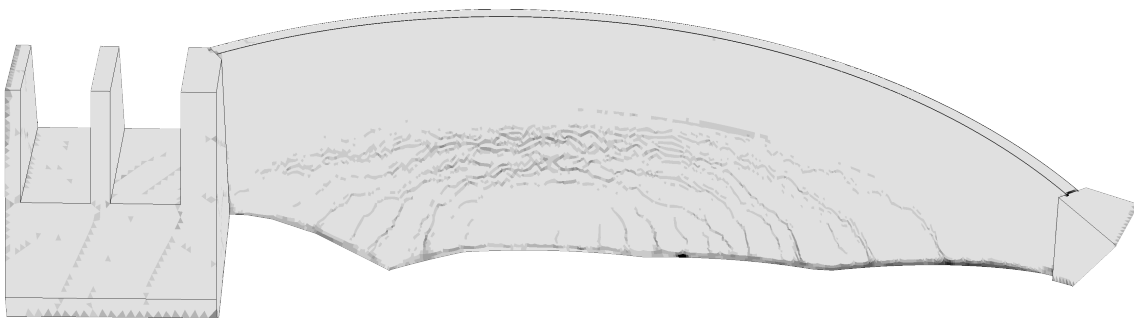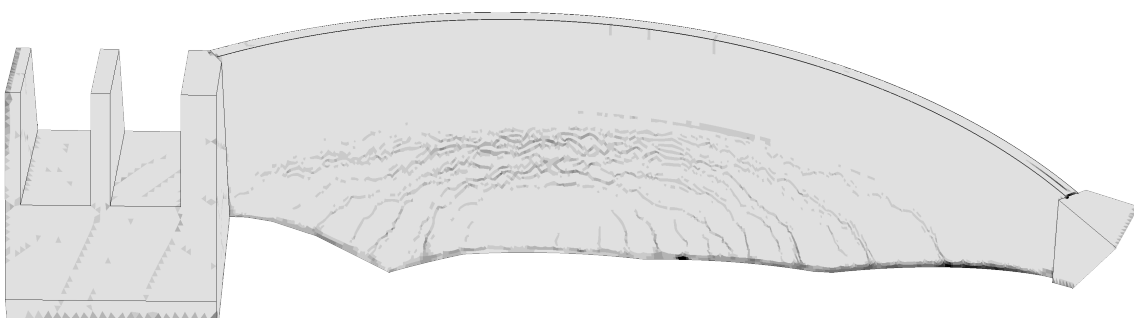Figure 7.47: Crack propagation in July the second year on the downstream surface.
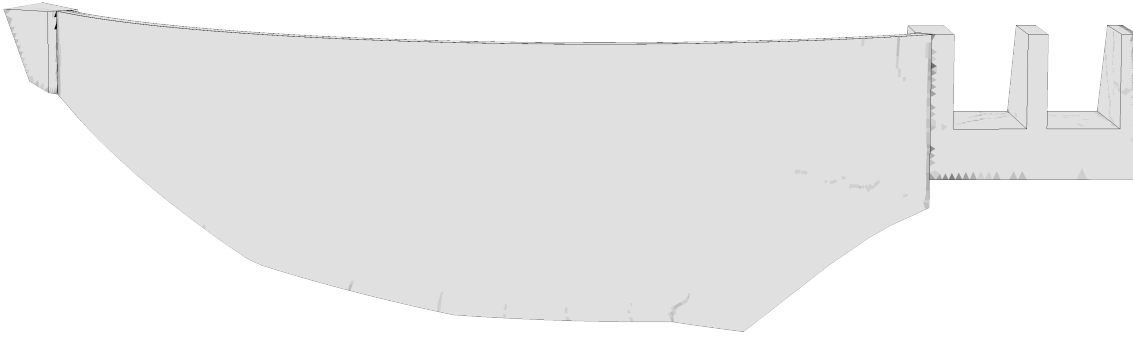
Figure 7.48: Crack propagation in July the second year on the upstream surface.

7.3.4   Implementing the tensile damage parameter, d_t, in the CDP model

With a mesh identical to the previous analyses the spillway and support experienced very large and unrealistic crack formations. A finer mesh in these parts was therefore used with distortion control activated and a lower density in order to get a stable solution. Distortion control is a technique available in Abaqus/Explicit which prevents solid elements from inverting or distorting excessively in analyses which otherwise would fail prematurely due to relative high strain in a coarse mesh. Note that the distortion control was only activated for the spillway and support, the dam body was modelled in the same way as in the previous non-linear analyses.

Quasi-static control

The strain energy and kinematic energy for the whole model, during the total time of the non-linear analysis, was extracted from Abaqus. The values were compared in order to ensure that a quasi-static analysis was performed according to Section 4.5.4.

Figure 7.49 presents the resulting strain and kinematic energy on a global scale throughout the whole analysis for the WC temperature combination. The maximum ratio between the strain and kinematic energy is approximately 2.3 % indicating small kinematic effects and a quasi-static behaviour. At some points between 0 and 2 seconds the ratio between the kinematic energy and the strain energy exceeds the recommended value, however, since this occurred during the gravity and hydrostatic step and the strain energy develops at a slower rate, this is neglected.
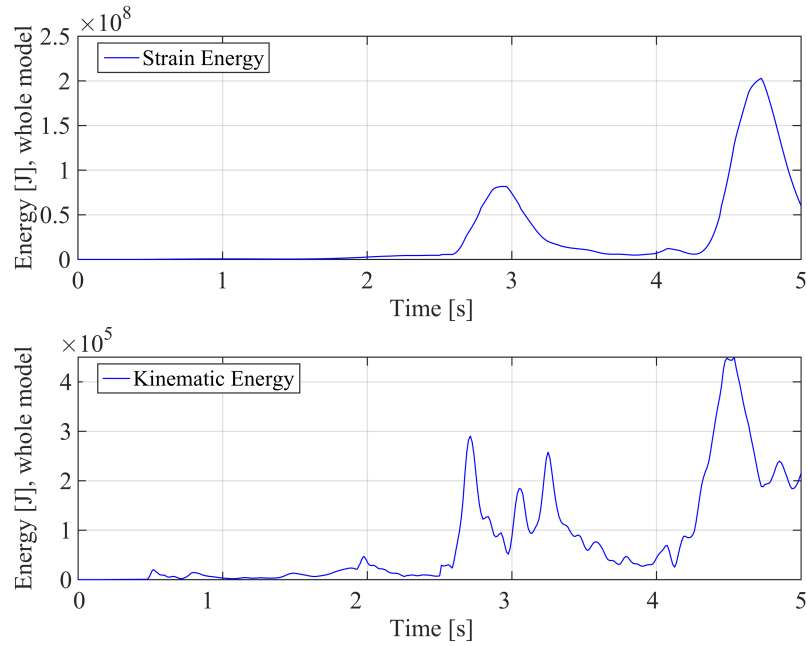
Figure 7.49: Strain energy and kinematic energy for the whole model for a warm year followed by a cold year with the damage parameter, d_t, $= 0.95$

Deformation

The largest calculated displacement of the crest in the upstream, positive, direction occurred in July of the warm year. The largest calculated displacement of the crest in the downstream, negative, direction occurred in January of the cold year. The calculated radial displacement of the crest is illustrated in Figure 7.50 and the calculated displacement 14 meter below the crest is illustrated in Figure 7.51. The deformation caused by gravity and hydrostatic forces, refereed to in the displacement figures as *Initial conditions*, are plotted as a dotted line. The squiggly arrow in the figures indicates the the water flow direction.
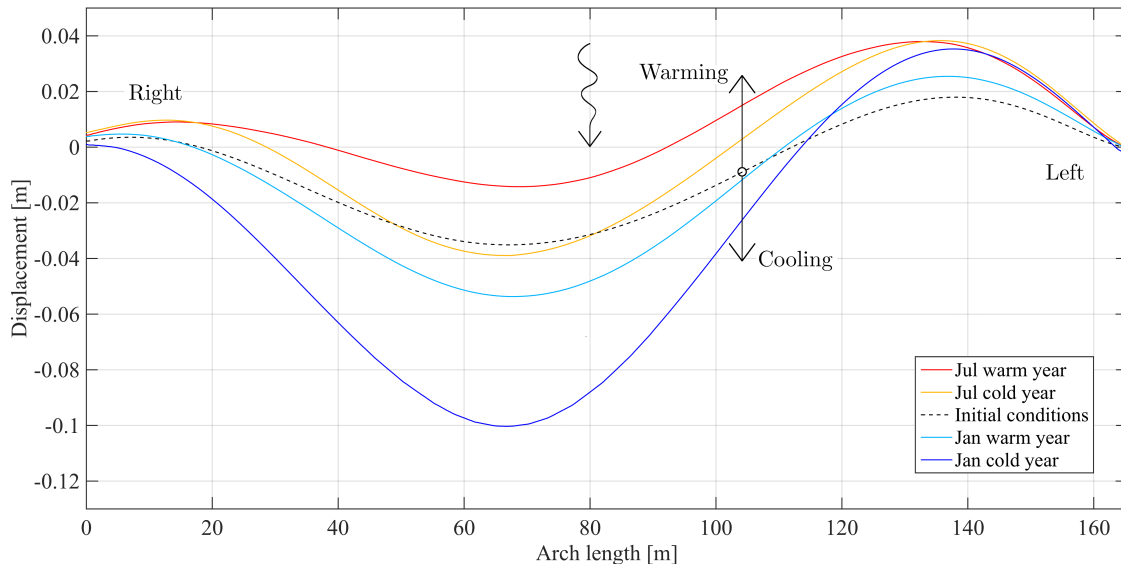
Figure 7.50: Maximum calculated radial displacement of the crest line for a warm year followed by a cold year with $d_t = 0.95$.
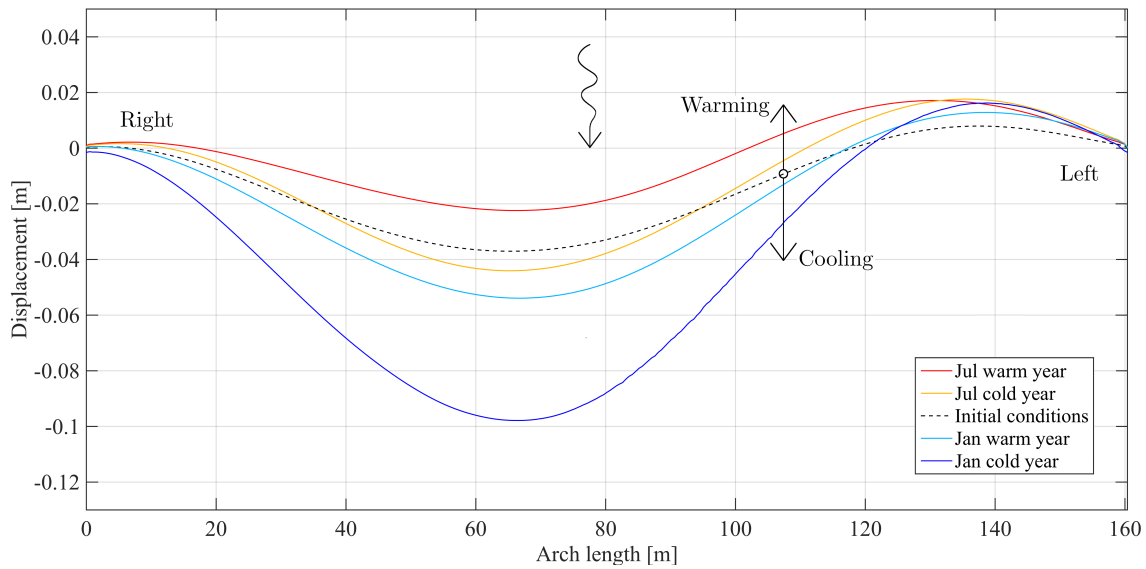
Figure 7.51: Maximum calculated radial displacement along a line 14 m below the crest on the downstream surface for a warm year followed by a cold year with $d_t = 0.95$.

The radial displacement of the centre section was measured as a function of height and is presented in Figure 7.52. The largest calculated displacement in the upstream direction, referred to as *Minimum* in Figure 7.52, occurred in July of a warm year. The largest displacement in the downstream direction, referred to as *Maximum* in Figure 7.52, occurred in January of a cold year.
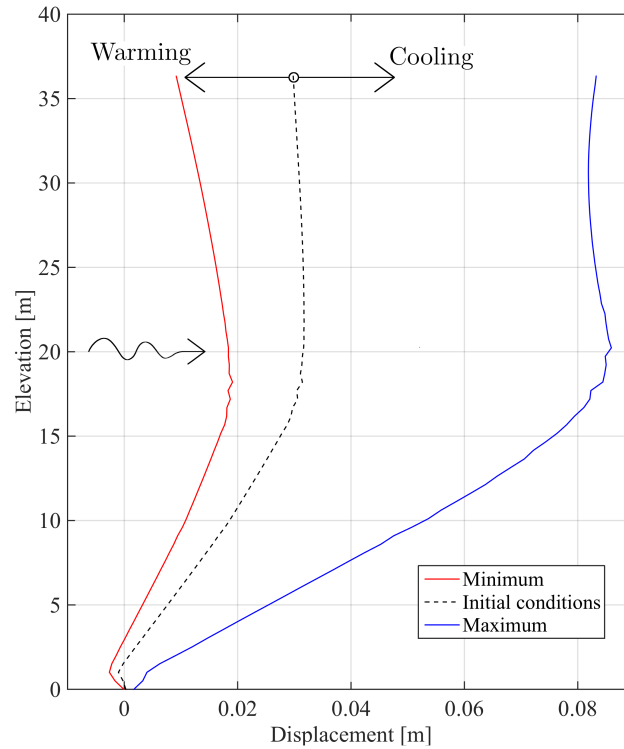
Figure 7.52: Maximum calculated radial displacement with $d_t = 0.95$.

Crack propagation

The total number of elements in the dam body that reached a plastic strain of over 0.001 is plotted in Figure 7.53 together with the temperature in the middle of the dam and in 7.54 together with the absolute value of the temperature gradient.

Figure 7.53: The temperature in the middle of the dam body, node (b) in Figure 7.1, as well as the number of elements in the dam body which was assumed to have cracked over time.

Figure 7.54: The absolute value of the temperature difference between the upstream and downstream surfaces of the dam as well as the number of elements in the dam body which was assumed to have cracked over time.

The number of cracked elements are presented in Table 7.3 for the initial condition, January and July of both years, as well as at the end of the analysis.

Table 7.3: The number of elements that have reached a plastic strain greater than 0.001 in the dam body.

	Time	Number of elements	% of total elements
	Gravity and hydrostatic pressure	5152	2.3
a	July the first year	5414	2.4
b	January the first year	8733	3.9
c	July the second year	9344	4.2
d	January the second year	24513	11.0
e	Complete analysis	24935	11.2

As evident by Figure 7.54 the crack propagation over time follows a similar development as the analysis without d_t implemented, as presented in Figure 7.34. Therefore only the crack patterns in January the second, cold year, is presented in Figure 7.55.

Figure 7.55: Crack propagation in January the second year on the downstream surface.

7.3.5   Analysing the cause of crack propagation

In the results from the analyses, both the mean temperature of the dam and the absolute value of the gradient are presented. Due to the negative correlation of the lowest mean temperature and the largest absolute gradient during winter months it is hard to draw conclusions as to which was the most important factor in regards crack propagation.

An analysis was therefore set up to determine which of the factors were the main cause of crack propagation. The temperature combination used in the analysis was based on the CW temperature combination and is illustrated in Figure 7.56.
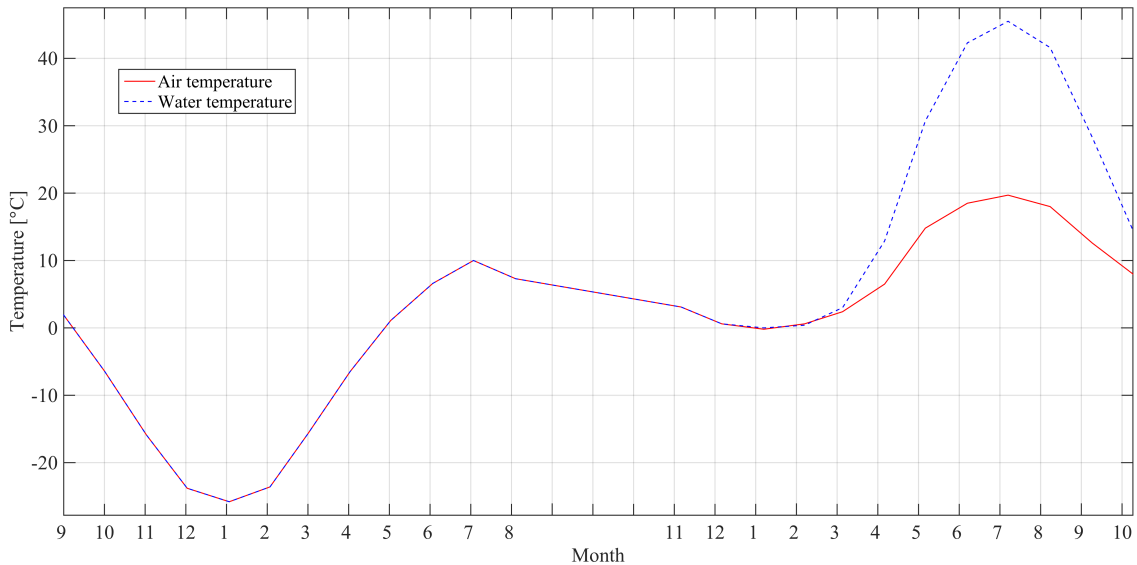
Figure 7.56: Ambient air and water temperatures for the temperature combination used to determine the cause of crack propagation.

The temperatures for the water and ambient air during the first year coincide and during summer months of the warm year the water temperature rises so that the gradient in the dam becomes equal to the gradient of the cold winter in the non-linear analyses. Note that this is not a realistic temperature variation and was only done in order to investigate the cause of crack propagation.

The total number of elements in the dam body that reached a plastic strain of over 0.001 is plotted in Figure 7.57 together with the temperature in the middle of the dam and in 7.58 together with the absolute value of the temperature gradient.
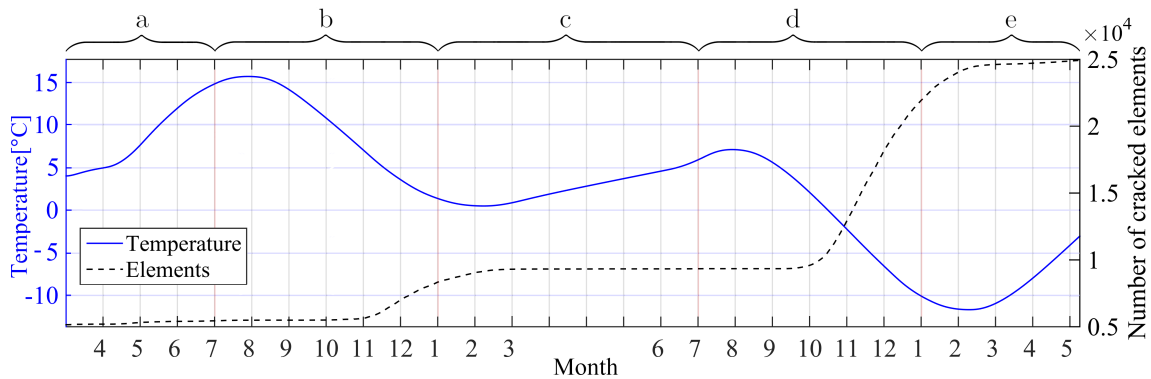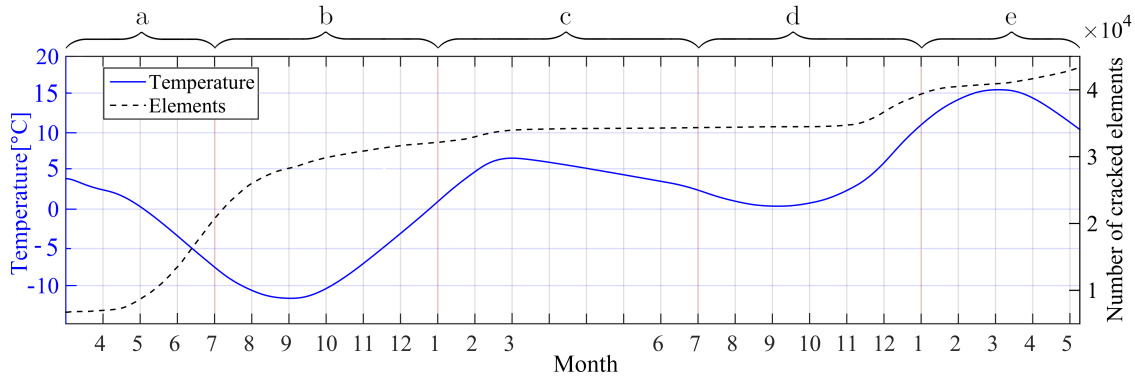
Figure 7.57: The temperature in the middle of the dam body, node (b) in Figure 7.1, as well as the number of elements in the dam body which was assumed to have cracked over time.
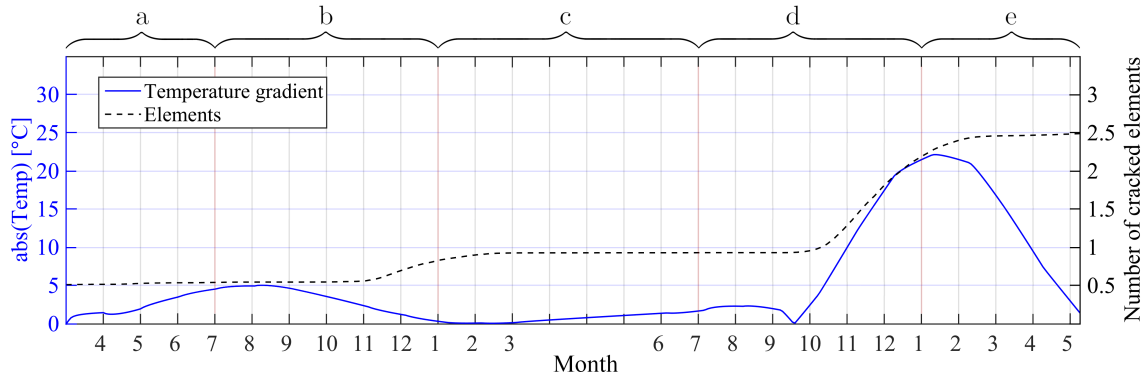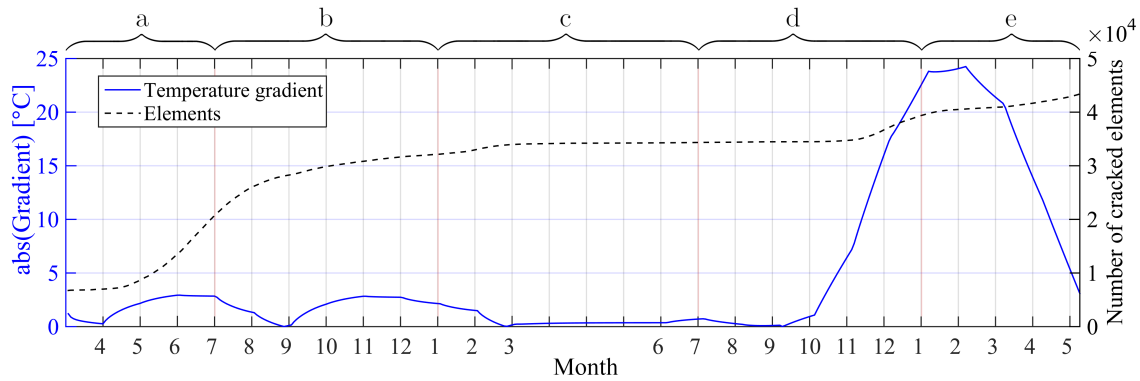

Figure 7.58: The absolute value of the temperature difference between the upstream and downstream surfaces of the dam as well as the number of elements in the dam body which was assumed to have cracked over time.

7.4 Compilation of results

A compilation of the results from the analyses is presented below for easier overview and comparison.

Table 7.4: Maximum radial displacement of the dam body along the crest.

Case	Upstream		Downstream	
	Disp. [mm]	Pos. [m]	Disp. [mm]	Pos.[m]
Linear	25.9	135.1	-62.6	58.4
Warm - Cold	47.5	132.5	-103.9	67.2
Cold - Warm	99.2	135.1	-104.3	67.7
Warm - Cold, d_t	38.3	135.5	-100.3	66.7

Table 7.5: Maximum radial displacement of the dam body along a line 14 m below the crest on the downstream surface.

	Upstream		Downstream	
Case	**Disp. [mm]**	**Pos. [m]**	**Disp. [mm]**	**Pos.[m]**
Linear	9.8	128.3	47.4	56.1
Warm - Cold	22.7	130.5	-96.5	66.3
Cold - Warm	43.4	133.5	-97.2	68.3
Warm - Cold, d_t	17.1	130.5	-97.9	66.8

Table 7.6: Number of elements that have reached a plastic strain greater than 0.001 in the dam body for the CW year temperature combination.

Time	**Number of elements**	**% of total elements**
Gravity and hydrostatic pressure	6725	3.0
January the first year	21885	9.8
July the first year	23876	10.7
January the second year	24062	10.8
July the second year	25475	11.4
Complete analysis	26372	11.9

Table 7.7: Number of elements that have reached a plastic strain greater than 0.001 in the dam body for the WC temperature combination.

	$d_t = 0$		$d_t = 0.95$	
Time	**Number of el.**	**% of total**	**Number of el.**	**% of total**
Gravity and hydrostatic pressure	6725	3.0	5152	2.3
July the first year	7243	3.2	5414	2.4
January the first year	9852	4.4	8733	3.9
July the second year	10421	4.7	9344	4.2
January the second year	22868	10.3	24513	11.0
Complete analysis	23724	10.7	24935	11.2

Chapter 8

Discussion and further research

The results from the thermal, linear mechanical and non-linear mechanical analyses coincide with each other as to how, when and where the dam deforms and cracks propagate. It can be concluded from the analyses that the seasonal temperature variations have a significant influence on the structural behaviour of arch dams in colder climates.

Some simplifications, presented below, were made in the modelling which were not presented in Section 1.3 or in Chapter 5 and 6. Presumably these would not change the result in any major way but should nevertheless be recognised when performing similar analyses or when comparing calculated results with measurements. Together with the limitations presented in Section 1.3, these simplifications could be studied further for even more accurate analyses.

Due to the steel bars being embedded in the concrete as a membrane there is a perfect bond between the materials. In reality the interaction between the steel bars and the surrounding concrete is not perfect, allowing for some relative motion in areas with high tensile stresses. Due to the reinforcement being modelled as an embedded membrane, as opposed to each bar being modelled individually, bond slip was considered to be outside the scope of this report.

No consideration of the fatigue strength of the reinforcement was implemented in the model. As the stresses changes in direction during the seasons the steel will experience cyclic compression and tension causing the steel to fatigue in areas that has experienced cracking.

The rock surfaces exposed to air will during the winter months most likely have a layer of insulating snow which would have a similar thermal effect as the insulating wall has on the downstream side. The same is true for the surfaces on top of the dam which are exposed to air. The water temperature in the reservoir could also be modelled with varying temperature over the depth, especially during the warmer months.

8.1 Thermal analysis

The thermal analysis was able to provide an idea of when large displacements and cracks would most likely occur and propagate in the dam. The temperature difference between the upstream and downstream surfaces, plotted in Figure 7.2 and 7.3, indicated that the temperature in the middle of the dam was the lowest and the gradient was the highest during the winter months. Large displacements and cracking would presumably occur in this time period.

The calculated temperature variation in Figure 7.2, indicated that the insulated wall have some effect on reducing the temperature gradient and delaying the heating and cooling of the dam body. By comparing the temperature variations of node (a) and node (d) the effect is noticeable as the

gradient in the dam body was reduced by a few degrees. However, since no further research was done on the impact of the insulating wall, it was not possible to draw any conclusion as to how significant the effect of the wall was on the thermal response of the structure.

8.2   Linear mechanical analysis

The results from the linear mechanical analysis display large areas on the lower half of the downstream surface where the maximum principal stress exceeds the tensile strength of the concrete, *i.e.* cracking is likely to occur. An explanation for the relatively large areas is the linear behaviour of the material, allowing the concrete to exceed its tensile strength without the development of cracks which would otherwise have redistributed the stresses in the structure.

During the colder months, the concrete contracts and the dam deflects towards the downstream side. During the warmer months the concrete expands and the dam deflects towards the upstream side.

The calculated stresses indicated, just as the thermal analysis, that most of the cracking will occur during the winter months, as illustrated in Figure 7.15. The crack direction, which was later visualised in the non-linear mechanical analyses, could be accurately predicted by the maximum and minimum principal stress direction plots in Section 7.2.3. As most of the elements exceed the tensile strength of the concrete during the winter of the cold year, Figure 7.20 is of particular interest as to how the crack patterns in the subsequent non-linear analyses developed.

8.3   Non-linear mechanical analyses

8.3.1   Deformation

The shape of the deformation was similar in the linear mechanical analysis and the non-linear mechanical analyses, however the magnitude of the displacements differed quite a bit, from about 62 mm to 104 mm due to the non-linear material properties. In the linear elastic material model the stress-strain relation is linear requiring an increase of stress in order to increase the strain. In the non-linear modelling tension softening occurs once the stress exceeds the yield stress and strain can develop further without an increase in stress.

The unsymmetrical deformation along the arch might be due to the varying height of the dam. The largest radial displacement in the non-linear mechanical analyses occurred between 60 - 80 m from the spillway where the dam is the tallest.

During the colder months the dam deforms in the downstream direction which is further amplified by the hydrostatic pressure. Since more hydrostatic pressure is acting on the taller sections of the dam, these areas experience larger deformation. The large deformation in the upstream direction, near the left support, might be due to the angle of the connection to the hydrostatic force. Furthermore, as the dam body is not as tall in this section, the hydrostatic pressure is relatively low which leads to less of a counteracting force and allows for more upstream deformation. The smaller deformation in the taller sections of the dam is, by the same reasoning, reduced by the larger hydrostatic force pushing the dam downstream during the warmer months.

The difference in shape of the radial displacement in the linear and non-linear mechanical analyses are most likely due to the redistribution of stresses in the body which is allowed due to the non-linear material properties. The difference in displacement between the WC and the CW temperature combinations is most likely due to the large crack propagation which occurs during the winter of the cold year.

8.3.2 Crack patterns and propagation

With the exception of a few vertical cracks at the crest in the CW temperature combination, the majority of the cracks were limited to the lower area of the dam as indicated by the linear analysis. In the middle of the dam the cracks propagated horizontally and as they got closer to the spillway and support they propagated diagonally towards the base. This crack pattern was indicated by the stress direction plots in the linear mechanical analysis presented in Section 7.2.3.

The horizontal cracks propagation is most likely due to the way the dam deforms. As illustrated in the vertical displacement plots, as well as the contour displacement plots, the lower half of the dam deforms downstream whereas the upper half does not. This deformation shape results in horizontal crack propagation as opposed to vertical.

Very few cracks propagated on the upstream surface in the non-linear analyses. Only a couple of vertical cracks at the base of the dam, and some horizontal cracks near the spillway, are visible in Figure 7.40 and 7.48. The real arch dam consists of several independently casted monoliths which was joined together to form the arch. As described in Section 1.3 the arch was in the analyses modelled as one continuous part, preventing any relative motion between the monoliths. In reality vertical cracks would most likely occur at the interactions between the monoliths as a result of the contraction joints not being able to fully transfer stresses and motion.

As presented in the thermal analysis the largest temperature gradient, and the lowest temperature in the middle of the dam, occurred in January of the cold year. The linear mechanical analysis also indicated that January of the cold year was the most critical in regard to displacement and cracking. The results of the non-linear analyses confirms that the propagation of cracks on the downstream surface was predominantly occurring during this period, as illustrated in Figure 7.34 and 7.42.

An interesting observation in Figure 7.42 and 7.54 is that the cracks seem to propagate only when the dam body is deforming downstream. During the summer months when the dam deforms upstream, cracks do not propagate, but as the temperature rises and the dam deforms downstream, towards its initial state, cracks starts to propagate. An explanation for this could be that as the dam deforms in the upstream direction the hydrostatic force counteracts and compressive forces are created in the dam body. When the temperature sinks and the dam deform downstream tensile forces arise and crack propagates.

8.3.3 Implementing the tensile damage parameter, d_t, in the CDP model

The non-linear analysis with implementation of the tensile damage parameter, d_t, and distortion control activated in the spillway and support took approximately four times as long to complete.

By comparing Figure 7.55 and 7.39 it is noticeable that the crack cluster, in the centre of the downstream surface, is more distinct in the analysis with d_t implemented. With only gravity and hydrostatic force acting on the dam, the number of cracked elements was fewer than for the analysis without d_t implemented, however during the thermal step more elements cracked.

8.3.4 Analysing the cause of crack propagation

As illustrated in Figure 7.57 and in 7.58 the crack propagation seems to correlate more with the mean temperature of the dam body than with the absolute value of the gradient. As illustrated in the figures, the gradient does have an effect on the crack propagation but the impact is not as distinct as when the mean temperature of the whole dam decreases.

The temperature combination modelled in the analysis used the temperature values of the ambient air of a cold year for both the upstream and downstream surfaces. This caused a very low average temperature in the dam and large areas cracked as a result. The main cause of crack propagation could be further investigated by using a higher average temperature, while keeping the gradient low. The insulating wall should also be removed in order to avoid bumps in the gradient as seen in the first year in Figure 7.58.

8.4 Conclusions

8.4.1 Modelling and FE-methodology

The modelling and method of analysis used in this work produced reasonable results and would most likely give satisfactory results if used to analyse other arch dams as well. Some observations which could assist in the modelling and method of analysis in further research are presented below.

First of all, the tie constraints between the dam body and spillway, and the dam body and support, resulted in large stresses in these areas. A more realistic model in these areas could be to fully merge the parts. This was not done in this work as merging of the parts would remove the tie constraint between the dam body and foundation, illustrated in Figure 6.3, and thus preventing the upstream side to lift. Tie constraints overall caused a lot of problems during the calculations and should based on our experience gained during this work be avoided if not deemed necessary.

Implementing the tensile damage parameter, d_t, in the CDP model may result in convergence problems and unstable analyses if some aspects are not properly addressed. A way to solve these convergence problems can be to activate the distortion control in Abaqus for the unstable parts and increased the step time for critical steps. This will increase the CPU-time significantly but should give more realistic results than without d_t implemented.

48 hour time increment in the thermal analysis was found to be adequate and a good compromise between keeping the CPU-time low and producing results which are accurate enough for the analyses done in this work. By performing the thermal analyses separately and importing the results in to the mechanical analyses a lot of modelling time can be saved, especially when troubleshooting.

The use of smooth amplitude curves is a requirement in order to achieve quasi-static behaviour and is highly recommended to use in non-linear analyses.

8.4.2 Risk for and extent of cracking

By comparing and evaluating the results, conclusions can be drawn from the analyses, some of which are presented below.

The temperature variation has a significant impact on the movement of the dam body, with the largest displacement occurring in January of a cold winter. According to our work, cold winters have a major effect on arch dams in regards to deformation and cracking as the temperature of the dam goes below 0 °C.

The propagation of cracks mainly occurred during the winter months of the cold year which could be predicted in the linear mechanical analysis. The linear mechanical analysis was, however, not able to predict the cracking which took place after the summer of the warm year when the dam body returned from from upstream displacement.

The majority of the cracks propagated in the area where the largest radial displacement occurred during the winter months, *i.e*, between the centre section and the spillway.

Linear mechanical analyses are a quick and easy way in order to identify when, where and how cracks are likely to propagate. Non-linear analyses requires significantly more effort and drastically increase the CPU-time but are necessary in order to accurately describe the structural behaviour.

8.5 Further development

In order to fully understand the effects that temperature variation have on dam structures, extensive research is needed. The section will give a few examples of areas where further research could be conducted.

The main cause of crack propagation could be investigated in order to study whether crack initiation is caused by the temperature gradient or by the mean temperature in the dam. In this report, one simulation was done to study this, indicating that the mean temperature might be the dominant factor but no definite conclusion can be drawn from this simulation alone hence further research is needed.

The crack width and the safety of the dam as a result of the cracking was not included in this work and further studies is needed to adequately answer which effect the cracks have on the safety of the structure.

The thermal effects of the insulating wall and its effect on the crack propagation could be of interest in order to determine how effective insulating walls are in order to reduce crack propagation.

References

[1] Anderson, T. L. (2005). *Fracture mechanics: fundamentals and applications.* CRC Press, Miami, third edition.

[2] Björnström, J., Ekström, T., and Hassanzadeh, M. (2006). *Dammsäkerhet: spruckna betongdammar: översikt och beräkningsmetoder.* (Elforsk rapport; Vol. 06:29). Elforsk.

[3] Bobiński, J. and Tejchman, J. (2006). Modeling of strain localization in quasi-brittle materials with a coupled elasto-plastic-damage model. *Journal of Theoretical and Applied Mechanics*, 44(4).

[4] Chen, W.-F. (1982). *Plasticity in reinforced concrete.* McGraw-Hill, New York.

[5] Cornelissen, H. A. W., Hordijk, D. A., and Reinhardt, H. W. (1986). Experimental determination of crack softening characteristics of normalweight and lightweight concrete. *Heron*, 31(2):45–56.

[6] Dassault Systèmes (2014a). *Abaqus 6.14 Getting started with Abaqus: Interactive edition.* Dassault Systèmes Simulia Corp.

[7] Dassault Systèmes (2014b). *Abaqus 6.14 Theory Manual.* Dassault Systèmes Simulia Corp.

[8] Dassault Systèmes (2014). *Abaqus 6.14 Analysis User's Guide Volume III: Materials.* Dassault Systèmes Simulia Corp.

[9] de Borst, R. (2002). Fracture in quasi-brittle materials: a review of continuum damage-based approaches. *Engineering fracture mechanics*, 69(2):95–112.

[10] Eriksson, D. and Gasch, T. (2011). Load capacity of anchorage to concrete at nuclear facilities: Numerical studies of headed studs and expansion anchors. Master Thesis, Royal Institute of Technology (KTH), Stockholm, Sweden.

[11] Hillerborg, A. (1985). The theoretical basis of a method to determine the fracture energy GF of concrete. *Materials and structures*, 18(4):291–296.

[12] Jirásek, M. and Bazant, Z. P. (2002). *Inelastic analysis of structures.* John Wiley & Sons.

[13] Ju, J. W. (1989). On energy-based coupled elastoplastic damage theories: constitutive modeling and computational aspects. *International Journal of Solids and structures*, 25(7):803–833.

[14] Lee, J. and Fenves, G. L. (1998). Plastic-damage model for cyclic loading of concrete structures. *Journal of engineering mechanics*, 124(8):892–900.

[15] Léger, P. and Seydou, S. (2009). Seasonal thermal displacements of gravity dams located in northern regions. *Journal of performance of constructed facilities*, 23(3):166–174.

[16] Lindholm, K. (2017a). Elproduktion. *https://www.energiforetagen.se/sa-fungerar-det/el/produktion.* [2017-06-09].

[17] Lindholm, K. (2017b). Vattenkraft. *https://www.energiforetagen.se/sa-fungerar-det/el/produktion/vattenkraft*. [2017-06-09].

[18] Lubliner, J., Oliver, J., Oller, S., and Onate, E. (1989). A plastic-damage model for concrete. *International Journal of solids and structures*, 25(3):299–326.

[19] Malm, R. (2006). *Shear cracks in concrete structures subjected to in-plane stresses*. Licentiate Thesis, Royal Institute of Technology (KTH), Stockholm, Sweden.

[20] Malm, R. (2016). *Guideline for FE analyses of concrete dams*. (Energiforsk Report 2016:270). Energiforsk.

[21] Malm, R. and Ansell, A. (2011). Cracking of concrete buttress dam due to seasonal temperature variation. *ACI Structural Journal*, 108(1):13–22.

[22] Malm, R., Hellgren, R., Ekström, T., and Chaoran, F. (2016). *Theme A, Thermal cracking of a concrete arch dam*. Royal Institute of Technology (KTH), Division of Concrete Structures and ÅF International Division, MA Hydro Power Sweden.

[23] Model Code (2010). *fib Model Code for Concrete Structures 2010*. Number 55. International Federation for Structural Concrete (FIB), Lausanne, Switzerland.

[24] Ngo, D. and Scordelis, A. C. (1967). Finite element analysis of reinforced concrete beams. *Journal Proceedings*, 64(3):152–163.

[25] Omidi, O., Valliappan, S., and Lotfi, V. (2013). Seismic cracking of concrete gravity dams by plastic-damage model using different damping mechanisms. *Finite Elements in Analysis and Design*, 63:80–97.

[26] Ottosen, N. S. and Petersson, H. (1992). *Introduction to the finite element method*. Prentice-Hall.

[27] Ottosen, N. S. and Ristinmaa, M. (2005). *The mechanics of constitutive modeling*. Elsevier.

[28] Pacoste, C., Plos, M., and Johansson, M. (2012). Recommendations for finite element analysis for the design of reinforced concrete slabs. Technical report, Royal Institute of Technology (KTH), Stockholm, Sweden.

[29] Parmee, I. C. (1993). The Concrete Arch Dam. In *Artificial Neural Nets and Genetic Algorithms*, pages 544–551. Springer, Vienna.

[30] Petersson, P.-E. (1981). *Crack growth and development of fracture zones in plain concrete and similar materials*. Division of Building Materials, Lund Institute of Technology, Lund, Sweden.

[31] Rashid, Y. (1968). Ultimate strength analysis of prestressed concrete pressure vessels. *Nuclear engineering and design*, 7(4):334–344.

[32] Rombach, G. A. (2004). *Finite element design of concrete structures: practical problems and their solution*. Thomas Telford.

[33] SS-EN 1992-1-1:2005 (2008). *Eurocode 2: Dimensionering av betongkonstruktioner: Del 1-1: Allmänna regler och regler för byggnader*. Swedish Standards Institution, Stockholm.

[34] USACE (1994). EM1110-2-2201 Arch Dam Design. US Army Corps of Engineers, Washington DC.

Appendix

Linear elastic convergence study

The following figures illustrates the different solutions obtained by using varying element length, l, in the linear mechanical analysis. The enlarged part is the section used to measure the difference in displacement or stress. The results for the radial displacement are presented in Table 8.1 and for the maximum principal stress in Table 8.2.
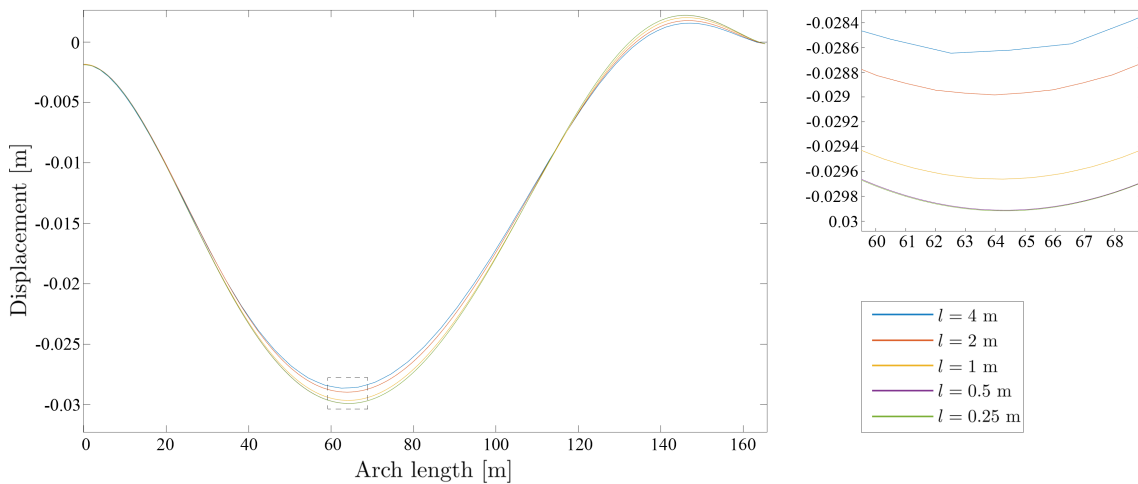

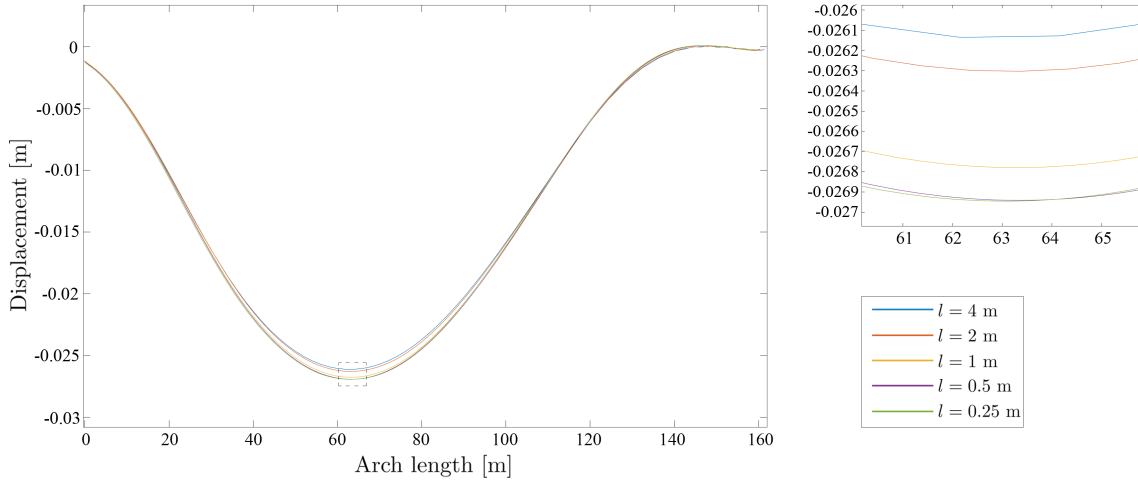Figure 8.1: Radial displacement of line 1.
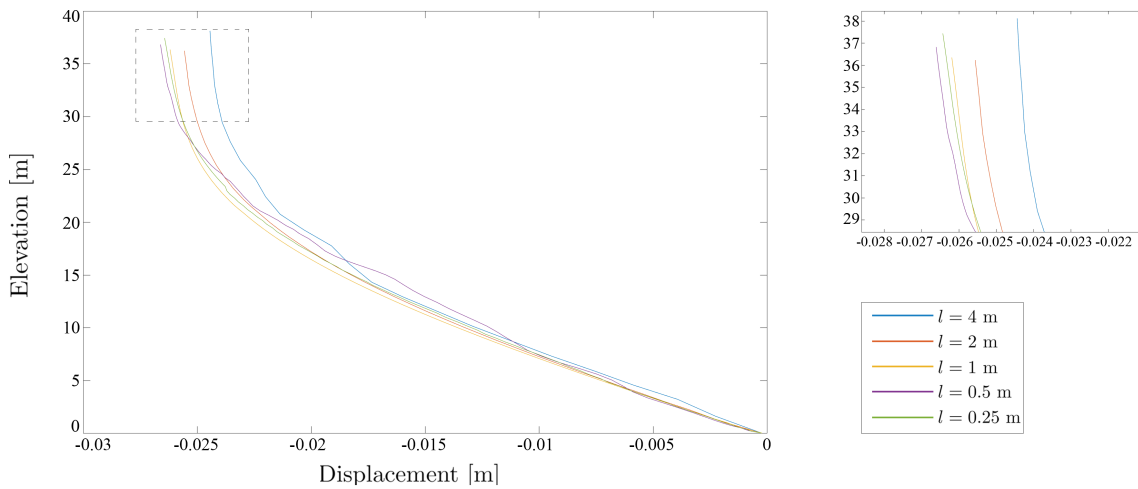
Figure 8.2: Radial displacement of line 2.

Figure 8.3: Radial displacement of line 3.

Table 8.1: Results from the convergence study for the dam mesh for radial displacement.

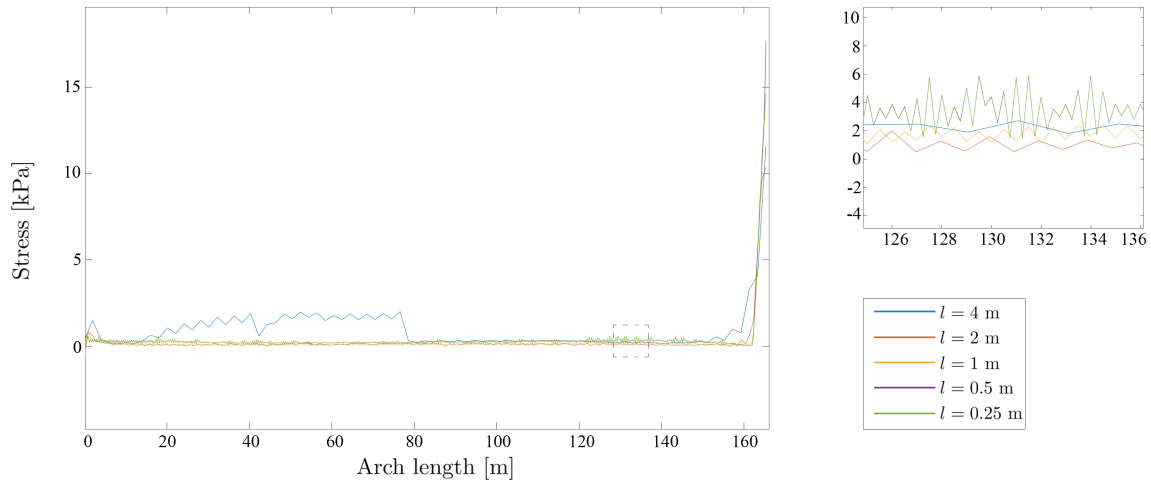| Element lengths [m]	Greatest difference in displacement along line 1	Greatest difference in displacement along line 2	Greatest difference in displacement along line 3
4.0 - 2.0	1.19 %	0.63 %	4.44 %
2.0 - 1.0	2.35 %	1.80 %	2.39 %
1.0 - 0.5	0.85 %	0.61 %	1.38 %
0.5 - 0.25	0.02 %	0.01 %	0.88 %

Figure 8.4: Maximum principal stress on line 1, the difference in stress between l=4 m and l=2 m was measured at 70-74 m.
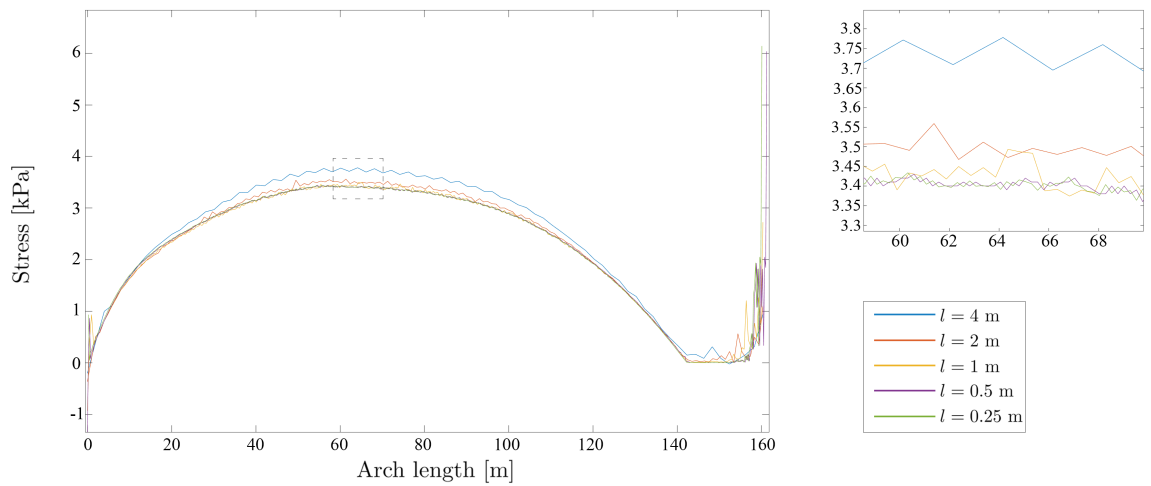

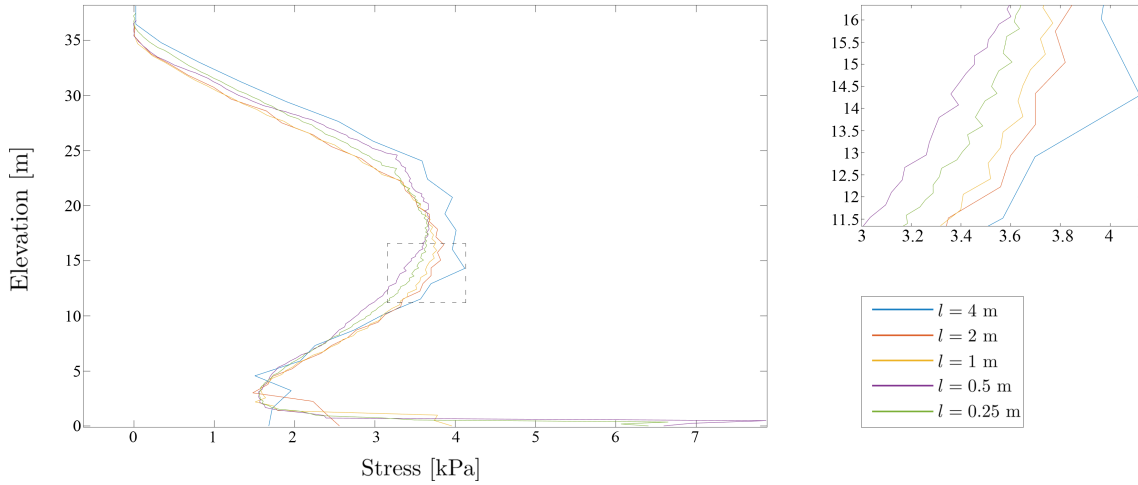Figure 8.5: Maximum principal stress on line 2.

Figure 8.6: Max principal stress on line 3.

Table 8.2: Results from the convergence study for the dam mesh for maximum principal stress.

Element lengths [m]	Greatest difference in max. principal stress along line 1	Greatest difference in max. principal stress along line 2	Greatest difference in max. principal stress along line 3
4.0 - 2.0	133.76 %	7.18 %	5.18 %
2.0 - 1.0	54.15 %	2.52 %	1.20 %
1.0 - 0.5	88.89 %	0.71 %	7.36 %
0.5 - 0.25	0.26 %	0.01 %	3.02 %

Conclusion

The result of the convergence study demonstrates that convergence according to our definition have been achieved for the displacements along all three lines when the element length is decreased from 4 m to 2 m.

The stress converges along all three lines when the element length is reduced from 0.5 m to 0.25 m. However, it seems unlikely that an element length of 0.25 m should be needed in order to achieve an accurate result in the linear analysis when the non-linear analysis required an element length around 0.5 m, see Section 6.3.7. It can also be said that the difference in displacement and stress follow each other well along most of the arch length and vertical line and that the difference in result is studied in the area where the largest difference occur. It is not reasonable to set the element length to 0.25 m in order to take these small areas into consideration when most of the structure have converged at an coarser mesh. An element length of 2 m was deemed sufficient for the linear analysis.